Theses and Dissertations

2016

Thermodynamic Analysis of Carbon Capture and Pumped Heat Electricity Storage

Fan Ni
Lehigh University

Thermodynamic Analysis of Carbon Capture and Pumped Heat Electricity Storage

by

Fan Ni

A Dissertation

Presented to the Graduate and Research Committee

of Lehigh University

in Candidacy for the Degree of

Doctor of Philosophy

in

Chemical Engineering

Lehigh University

Jan, 2016

Certificate of Approval

Approved and recommended for acceptance as a dissertation in partial fulfillment of the requirements for the degree of Doctor of Philosophy.

_____

Date

_____

Accepted Date

_____

Prof. Hugo S. Caram
Dissertation Director

Committee Members:

_____

Prof. Hugo S. Caram, Lehigh University

_____

Prof. Mayuresh Kothare, Lehigh University

_____

Prof. Cesar A. Silebi, Lehigh University

_____

Prof. Alberto LaCava, Felician College

_____

Dr. Ramesh Gupta, ExxonMobil Research and Engineering Co.

_____

Dr. Simon C. Weston, ExxonMobil Research and Engineering Co.

Acknowledgements

This work will not be possible without the guidance and help from my advisor and committee members, our industry partners, my friends at Lehigh and my parents in China.

As my Ph.D. advisor Prof. Caram is always supportive and helpful with my research projects and willing to share his wisdom when my work comes to a difficult time. I would not come so far without his patience and encouragement. Prof. LaCava provided crucial support for my study in adsorption and guided me through the detailed operation and simulation of pressure swing adsorption processes. I would like to thank Prof. Kothare and Prof. Silebi for being my committee members and shared with me the knowledge of chemical processes design. I would also like to thank Dr. Gupta, Dr. Weston and Dr. Thomann for supporting me and working with me on the carbon capture projects. This work would have stayed on paper without support and insight from our industry partners.

My friends at Lehigh both from within and out of the department of chemical engineering make my life here easier and cheerful. I would specially thank our department engineering technician John Caffrey for be a miracle of my research life by making the impossible possible. I would also like to express warm gratitude to previous lab members and undergraduate students who helped on my research projects including Prof. Kwangkook Jeong, Dr. Michael Beaver, Dr. Ranjan Sahoo, Palis Tarasansombat, Daniel Camarda, Joseph Bhaskar and Lucas Cruz. Supports from my lab friends and also gym friends Roy B. Xu, Chih-Hsiu Lin and Chris Keturakis are greatly appreciated.

For my parents although they might not be able to understand the research I did at Lehigh, they were always there when I needed their support.

Table of Contents

List of Tables

List of Figures

Abstract

This work can be divided into two different parts: Chapter 1, 2 and 3 are focused on carbon capture ranging from the thermodynamic analysis to the hybrid reactor design; Chapter 4 is devoted to the study of pumped heat electricity storage processes.

In Chapter 1 we aim to illustrate the basic separation energy calculation and minimum work requirement for sorption processes and calcium looping processes. Based on the study it is possible to compare the potential energy savings of different technologies, namely temperature swing adsorption (TSA) and calcium looping processes (CLP), which are currently under development for carbon capture. Without considering the material deterioration for CLP it was found out that CLP is more competitive for flue gas with CO_2 molar fraction less than 10% while TSA using zeolite 13X requires less work when CO_2 molar fraction becomes higher than 10%.

In Chapter 2 a specific hybrid reactor process called sorption enhanced reaction process (SERP) is discussed, which can be integrated into the pre-combustion carbon capture process for power plants with the potential to reduce the efficiency penalty compared with traditional post-combustion carbon capture processes. A detailed study is done to investigate the interaction of reaction and sorption on the performance of such processes. Four different zones were identified inside a well-developed sorption enhanced reactor: 1. the reaction controlled zone near the entrance, 2. the equilibrium zone after it, 3. the reaction mass transfer zone where both reaction and sorption interact with each other, 4. the equilibrium zone near the exit. Without considering the mass transfer resistance for adsorption and reaction, the only dominating factors are reaction kinetics and equilibrium constants and the shape of adsorption isotherm. It was found out that there are two different mechanisms that can affect the effluent profiles of the sorption enhanced reactor: 1. the reaction rate

determines the shape of the reaction mass transfer zone; 2. the shape of the isotherm determines the effluent profile of the adsorbate. Changing the reaction equilibrium constant will affect the effluent profile in both ways. Also the reaction stoichiometric parameters are discussed by comparing two different reactions: the water gas shift reaction and the hydrogen sulfide decomposition reaction. It was found out that it requires the reactor to be sulfur free in order to achieve high purity hydrogen product due to the stoichiometric coefficient of sulfur. The importance of mass transfer resistance and gas diffusion is also explored by the propene metathesis reaction.

The experimental work on the high temperature carbon dioxide adsorbent is included in Chapter 3. Dry PSA tests using argon as the purge gas were done on a bench scale single bed setup. Among different PSA cycle schemes it was found out that the best purity was achieved with a 5-step (1. pressurization 2. adsorption 3. blowdown 4. rinse 5. purge) PSA scheme where CO_2 purity of 86% (argon free) and recovery 18% was obtained. Thermogravimetric tests on fresh and PSA tested samples show that the used sample has a slower kinetics and lower equilibrium capacity. The limited success of the experimental results shows that the difficulties of the development of the appropriate CO_2 sorbents as well as the optimization of the PSA cycles in a small laboratory unit. To study the effects of steam a pilot scale PSA test setup was built. Based on the thermal front moving during the steam purge and the amount of CO_2 desorbed it is concluded that steam competes with CO_2 on the surface of Na-promoted alumina.

In Chapter 4 an emerging technology called pumped heat electricity storage (PHES) is discussed. It is a recently proposed competitive energy storage solution for large scale electrical energy storage (EES). It is especially valuable for regions where specific geological structures are not available. The performance of PHES depends on two factors: the operations of turbomachines and the thermal storage system. The former is characterized by pressure ratio, polytropic efficiency and gas heat capacity ratio. The latter contains the parameters of

heat regenerators that can be summarized into two dimensionless numbers: length Λ and step time π. The overall process operation can be described by temperature difference representing the energy stored per unit heat capacity, the storage bed utilization ratio and the turn-around efficiency. Exponential matrix solutions are obtained for a discretized heat transfer model of a typical pumped heat electricity storage process. Using the cyclic steady state and transient state solutions, we are able to analyze how dimensionless length and step time affect the storage bed utilization ratio as well as the turn-around efficiency. Our model provides basic guidance for further development of such processes.

████████ Thermodynamic Analysis of Adsorption and Calcium Looping Processes for Carbon Capture

1.1 Introduction

There is much work regarding the development of adsorption processes for CO_2 capture. The expectations are that adsorption processes will reduce the work needed for CO_2 separation. Unlike the work on improving the equilibrium capacity of adsorbents, the fundamental energy requirements for adsorption processes are rarely discussed. In this work the Gibbs energy of desorbed gas was used to calculate the minimum work requirement to regenerate the adsorbent and collect the desorbed gas at a desired pressure.

As pointed out by Berger and Bhown [1, 2], one cannot simply evaluate an adsorbent based on its properties alone, i.e. equilibrium capacity at a certain condition, heat of adsorption, thermal stability, heat capacity etc. Those properties need to be combined with a proper process. Until the optimum operating conditions are found for this specific adsorbent, we cannot reach a fair conclusion on the value of this adsorbent.

For temperature swing adsorption processes and chemical looping processes another important factor often overlooked [3] when evaluating energy requirement for a process is that heat requirement does not necessarily reflect the power loss imposed on a power plant. Hence it is more appropriate to evaluate those processes based on the equivalent work instead of the heat requirement.

We will: first provide the expression for the minimum thermodynamic work required to regenerate an adsorbent, which determines the best possible performance of an

adsorption process, second discuss how the shape of isotherm affect the minimum required energy and finally evaluate an example of calculating the equivalent work instead of required heat for a temperature swing adsorption process and a chemical looping process.

1.2 Thermodynamic minimum work of separation

It is well known [4] that according to the Gibbs free energy balance of the ideal gas at constant pressure before and after CO_2 capture, the minimum work of separation per mole of CO_2 captured for flue gas containing y moles CO_2 and (1-y) moles N_2 (Figure 1-1) is given by:

$$W_{min} = RT_0 \left[\frac{1}{r} \ln(1-r) - \ln y' - \frac{1}{ry} \ln(1-yr) \right] \tag{1.1}$$

where y' is the CO_2 partial pressure in the lean flue gas and r is the fraction of captured CO_2:

$$y' = \frac{y(1-r)}{1-yr} \tag{1.2}$$

Separation work

yr mol CO_2
1 bar 25 ^{o}C

Captured CO_2

y mol CO_2
(1-y) mol N_2
1 bar 25 ^{o}C

Flue gas

y(1-r) mol CO_2
(1-y) mol N_2
1 bar 25 ^{o}C

Lean flue gas
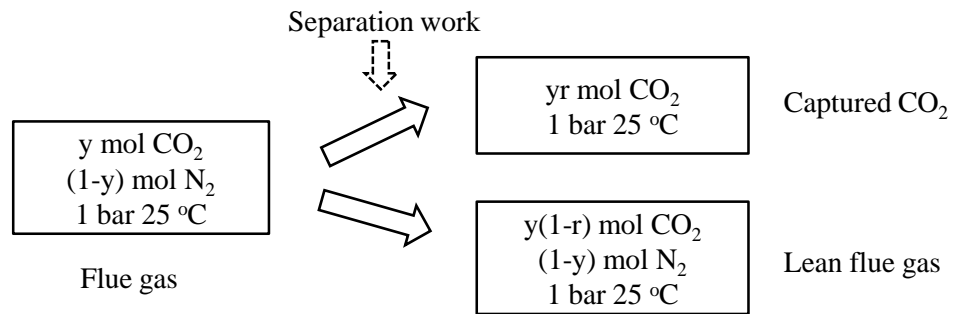
Figure 1-1 Thermodynamic minimum work of separation for CO_2 capture with recovery of r

In this work T_0 is the cold sink temperature, namely 25 ^{o}C for ambient temperature. In order to simplify our analysis pure CO_2 is assumed to be obtained as a result of the separation. Usually for carbon capture the purity of captured CO_2 ranges from 95% to

99% depending on the source and separation process. A modification on the CO_2 purity will be discussed in future work.
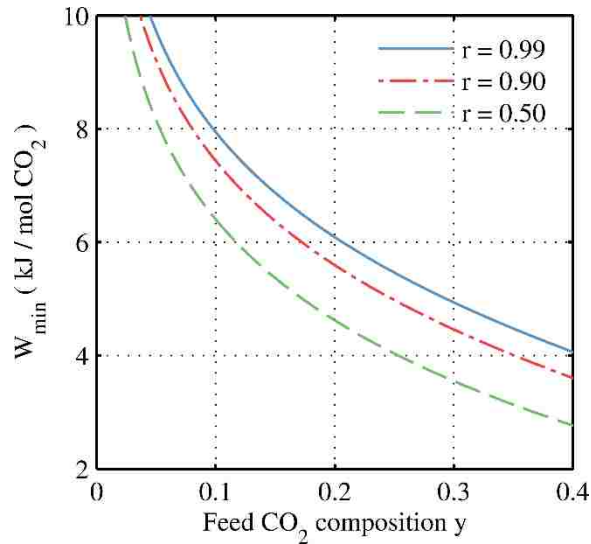
Figure 1-2 The dependence of thermodynamic minimum energy of separation on the rich flue gas composition y and the process recovery rate r

As shown in Figure 1-2 the minimum work is a function of the feed flue gas CO_2 composition y and the fraction of CO_2 being recovered (recovery) r. When y is increased less amount of energy is needed to separate unit amount of CO_2. The extra work needed to increase the recovery from 0.9 to 0.99 is larger compared with that needed to increase the recovery from 0.8 to 0.9 for the same feed rich flue gas. This pattern is true for all separation processes.

1.3 Minimum work of separation for adsorption processes

Adsorption processes use a selective adsorbent to capture CO_2 from the flue gas. After the adsorbent is saturated, a regeneration step is needed to recover pure CO_2 and produce clean adsorbent, for which external energy is required. Assume before regeneration the adsorbent is saturated with flue gas of CO_2 composition y_1 and after regeneration it is saturated with lean flue gas of CO_2 composition y_2. The CO_2 loadings at those two conditions are n_1 and n_2, respectively. The desorption process, shown in Figure 1-5,

6

consists an ideal CO_2-selective membrane unit that is put on top of the adsorbent while the gas in the interstitial space of the adsorbent is neglected. Assuming it is a reversible process, the CO_2 partial pressure on one side of the membrane is the equilibrium CO_2 partial pressure of the adsorbent. A vacuum pump is used for pull out the gas from the adsorbent and discharge it at the desired final pressure. As CO_2 is compressed and collected in downstream, the CO_2 loading gradually decreased to n_2. Because the heat of desorption doesn't need to be taken into account at room temperature to calculate the equivalent work, the only work needed here is the isothermal reversible compression work for pure CO_2 and lean flue gas. For an ideal gas, the minimum equivalent work per mole of captured CO_2 by the process shown in Figure 1-5 is written as:

$$W_{ad} = \frac{RT_0}{n_1 - n_2} \int_{n_1}^{n_2} \ln(P / P_{atm}) dn \qquad (1.3)$$

Eq. (1.3) can also be obtained by combining the grand potential of the clean adsorbent described in Myer and Monson's work [5] and Gibbs free energy of ideal gases as shown in Appendix A. Utilizing the isotherm of the adsorbent at room temperature, $n=f(P)$, the minimum work of separation for adsorption processes can be estimated. This minimum work is independent of the overall separation process and cannot be reduced. Note that it is also independent of the heat of adsorption. Here the analytical expressions for a linear adsorption isotherm ($n=kP$) and a Langmuir adsorption isotherm ($n=mKP/(1+KP)$) are listed in Table 1 in terms of pressure and adsorbent loading respectively.

Table 1-1 Minimum equivalent work of separation for adsorption processes

Linear isotherm~p	$W_{lin} = RT_0 \left[1 - \dfrac{p_1 \ln p_1 - p_2 \ln p_2}{p_1 - p_2} \right]$	(1.4)
Linear isotherm~n	$W_{lin} = RT_0 \left[1 - \dfrac{n_1 \ln(n_1 / k) - n_2 \ln(n_2 / k)}{n_1 - n_2} \right]$	(1.5)
Langmuir isotherm~p	$W_{lang} = \dfrac{RT_0 \left[m \ln \dfrac{m}{1 + Kp} + \dfrac{mKp}{1 + Kp} \ln p \right]\Big\|_{p_1}^{p_2}}{n_1 - n_2}$	(1.6)
Langmuir isotherm~n	$W_{lang} = \dfrac{RT_0 \left[m \ln(m - n) + n \ln \dfrac{n}{(m - n)\,K} \right]\Big\|_{n_1}^{n_2}}{n_1 - n_2}$	(1.7)

It is shown in Eq. (1.4) that W_{lin} is independent of the slope of the isotherm, while based on Eq. (1.6) we know that W_{lang} is related to the Langmuir adsorption isotherm parameters K and m. For simplicity zeolite 13X is chosen in this work as the reference adsorbent for CO_2 capture. The adsorption model is described by Chue et al. [6] with m = 5.1 mol/kg, K = 14.2 bar^{-1} and ΔH = -34.5 kJ/mol (at 25 $^{\circ}$C). The results of the minimum separation work for the linear and the Langmuir adsorption isotherm are shown in Figure 1-3 and Figure 1-4.
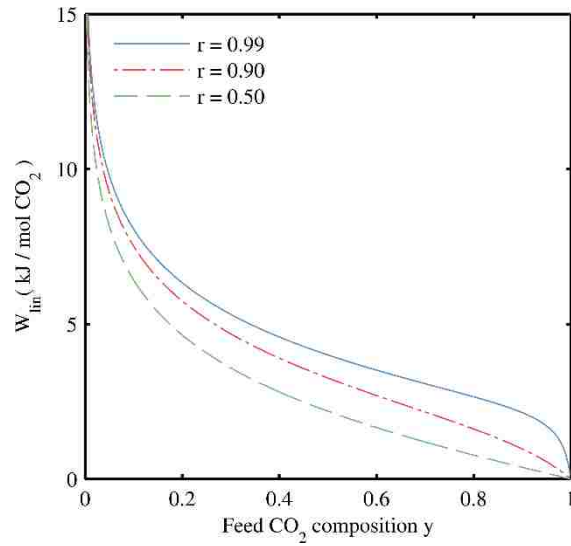
Figure 1-3 The minimum equivalent work of separation for the linear adsorption isotherm adsorbent varies with the feed composition and the process recovery rate
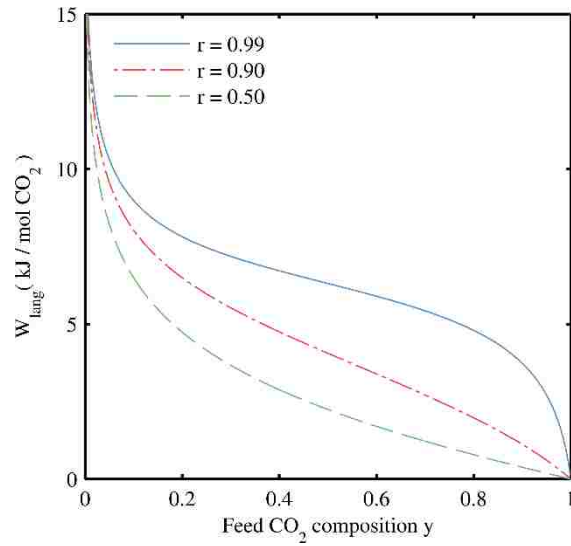
Figure 1-4 The minimum equivalent work of separation for the Langmuir adsorption isotherm adsorbent varies with the feed composition y and the process recovery rate r where m = 5.1 mol/kg and K = 14.2 bar^{-1}

9
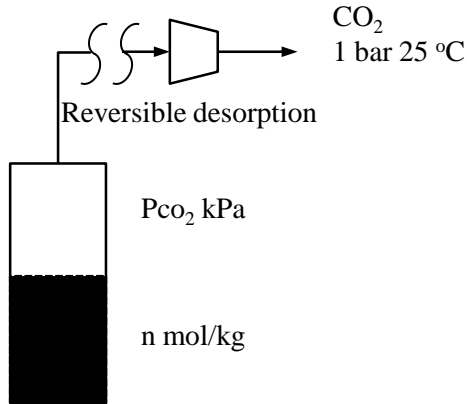
Figure 1-5 Reversible regeneration process with a CO_2-selective membrane unit
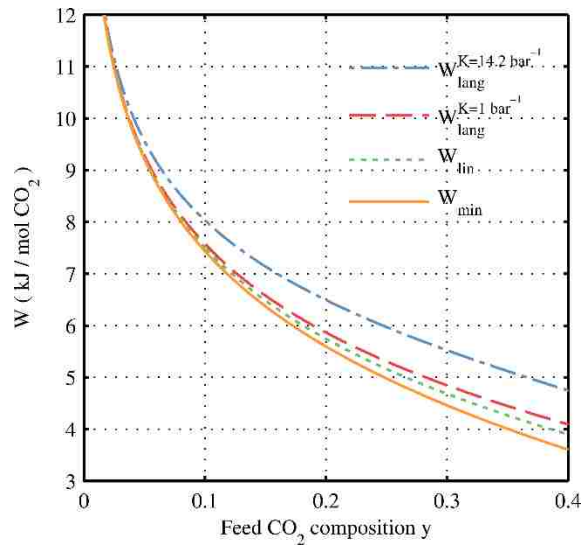
Figure 1-6 The minimum work of separation for adsorption processes depends on the shape of the isotherm where m = 5.1 mol/kg and r = 0.9

In Figure 1-6 the minimum work of separation for adsorption processes with the linear isotherm and the Langmuir isotherm and the thermodynamics minimum work of separation is compared. According to the equation derived by us before, the minimum work of separation for adsorbents of linear isotherm is only related to the feed flue gas conditions and recovery rate. The minimum separation work must be lower than that of the linear and the Langmuir isotherm. As the value of K decreases the minimum separation work approaches that of the linear isotherm, due to the fact that the isotherm is closer to a linear isotherm.

1.4 Energy analysis for temperature swing adsorption processes

Previously the minimum work of separation for adsorption processes has been analyzed by assuming reversible desorption with a CO_2-selective membrane unit while the bed temperature is kept at room temperature (T_{ad}). In reality the regeneration step can be carried out at an elevated temperature (T_{de}) as temperature swing adsorption (TSA), or at a lower pressure as pressure swing adsorption (PSA), or a combination of both, or using a purge gas, usually steam. In all cases the minimum work of separation calculated here remains the same. For a TSA process the regeneration energy includes two parts, sensible heat to increase the adsorbent temperature from T_{ad} to T_{de} and heat of adsorption ($-\Delta H$). In an ideal case the energy needed to provide the sensible heat can be minimized by using a perfect heat exchanger between the regenerated adsorbents and the saturated adsorbents and adsorbed gas as is done in the amine processes. However the process with lower regeneration energy requirement doesn't necessarily equal to the one with less parasitic energy penalty to the power plant. In order to evaluate the parasitic energy the following equation [1] is normally used to calculate the equivalent work for a TSA process:

$$W_{TSA} = \eta_{turbine}\eta_{Carnot}\left[c_p(T_{de}-T_{ad})/(n_1-n_2)-\Delta H\right] \quad (1.8)$$

This equation allows us to calculate the energy penalty of carbon capture processes on power plants without worrying about details of extracting steam from power plants. The Carnot efficiency is calculated based on the desorption temperature as:

$$\eta_{Carnot} = 1-T_{ad}/T_{de} \quad (1.9)$$

The turbine efficiency $\eta_{turbine}$ is usually around 0.75 in Eq. (8) to calculate the equivalent electricity that can be produced by expanding the equivalent steam in a steam

turbine. Since we are only interested in equivalent work in this study $\eta_{turbine}$ is assumed to be 1 and neglected in all the following studies.

For a given adsorbent to achieve the given recovery as is described in Figure 1-1, the minimum desorption temperature can be determined by the Clausius-Clapeyron equation. At the end of the desorption step the CO_2 partial pressure at least need to reach 1 atm. After the adsorbent is cooled down the CO_2 partial pressure drops to the lean flue gas CO_2 partial pressure (p'), which is a function of the process CO_2 recovery r and feed composition y. Assuming the isosteric heat of adsorption (ΔH) is constant over the pressure and temperature range, the desorption temperature is calculated as:

$$T_{de} = \left[\frac{R}{\Delta H} \ln \frac{p_{atm}}{p'} + \frac{1}{T_{ad}} \right]^{-1}$$

(1.10)

where p' is a function of the feed composition and recovery rate. By substituting Eq. (1.10) into Eq. (1.8) we have:

$$W_{TSA} = \frac{c_p (T_{de} - T_{ad})^2}{T_{de}(n_1 - n_2)} + T_{ad} R \ln \frac{p_{atm}}{p'}$$

(1.11)

From Eq. (1.11) the energy to provide the heat of desorption $-\Delta H$, as shown in the second term, is only a function of adsorption temperature and lean flue gas CO_2 pressure. Note that the heat of adsorption ($-\Delta H$) does not appear in the second term, which describes the work of separation due to heat of desorption. This is counter intuitive in the beginning. For an adsorbent with high heat of desorption the desorption temperature is lower. The Carnot efficiency is also lower thus results in the same work of separation. Hence if we use a perfect heat exchanger the minimum separation work for a TSA process can be expressed as:

$$W_{TSA}^{min} = T_{ad} R \ln \frac{p_{atm}}{p'} = T_{ad} R \ln \frac{1 - yr}{y(1 - r)}$$

(1.12)

which is only a function of the CO_2 capture process parameters. As shown in Figure 1-7 the minimum work only depends on the feed composition y and the recovery rate r.
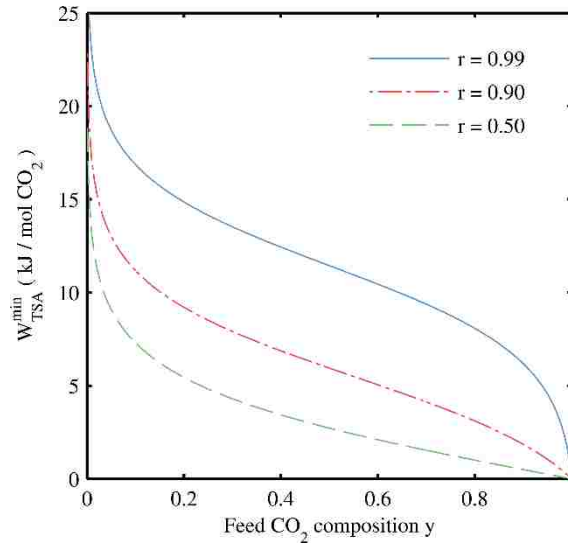
Figure 1-7 The minimum work of separation required by TSA processes varies with the feed compostion y and the recovery rate r when there is perfect heat recovery
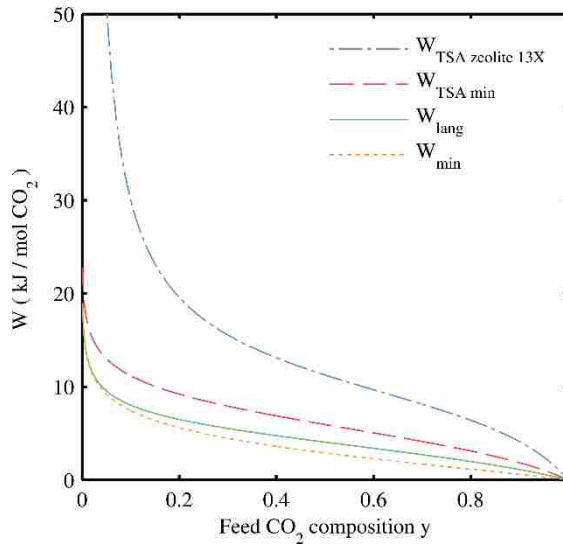
Figure 1-8 Comparison of different types of separation work for TSA processes

Up until now we have proposed 4 different levels of separation work for TSA processes: the thermodynamic minimum, the minimum for adsorption processes, the minimum for TSA processes and the separation work including sensible heat to heat up

the adsorbent. As shown in Figure 1-8 the first 3 levels provide the lower boundary for work requirement of adsorption processes while the fourth level provides an upper boundary.

1.5 Application to adsorbents screening for TSA processes

As an example we will compare activated carbon and zeolite 13X to illustrate how our model will help choosing an adsorbent requiring less separation work. To compare their minimum separation work requirement their adsorption isotherms at room temperature are required. According to Chue et al. [6] both materials can be described by the Langmuir adsorption isotherm model $n = mKP/(1+KP)$. To take the sensible heat into account for a TSA process their heat of adsorption are assumed to be constant as shown in Table 1-2.

Table 1-2 Properties of activated carbon and zeolite 13X

	Activated carbon	Zeolite 13X
K bar^{-1}	1.9	11
m mol/kg	2.5	4.9
c_p kJ/kg/K	1050	920
ΔH kJ/mol	-30	-36

The results are shown in Figure 1-9. Without considering the sensible heat $W_{carbon\ min}$ is closer to W_{min} than $W_{zeolite\ min}$. The reason is because that the Langmuir equilibrium constant K for activated carbon is much smaller, which makes the shape of the isotherm closer to a linear isotherm. However after the sensible heat is taken in to account the separation work for zeolite 13X is smaller than that of activated carbon. The reason is mostly due to the higher working capacity of zeolite 13X at the same working condition

as activated carbon. Less amount of adsorbent needs to be heated up thus it requires less energy for regeneration. Note that the work required to provide the sensible heat is significantly larger than the work of separation providing the heat of desorption.
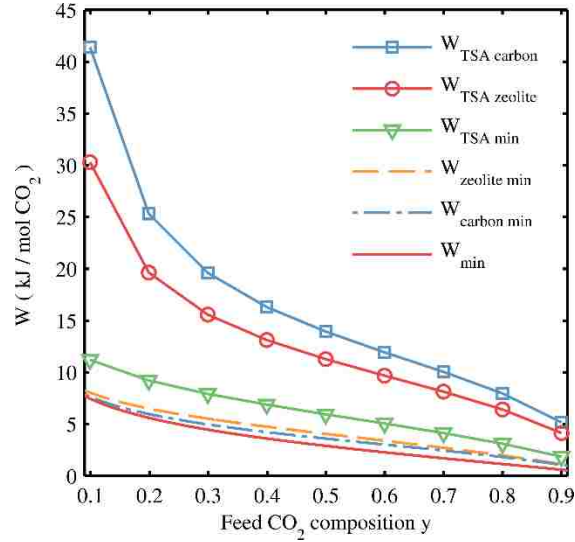
Figure 1-9 Comparison of different separation work for activated carbon and zeolite 13X when recovery r=0.9

1.6 Work of separation for chemical looping processes

According to Fan et al. [7] there are two types of chemical looping processes (Type A-I and A-II) used for CO_2 capture. Type A-I uses an oxygen carrier to provide a N_2 free oxidant to the fuel, thus avoids the need for CO_2 separation from the inert of the flue gas. Depending on the final product it can be used for co-production of hydrogen and power as the syngas chemical looping (SCL) or for power production only as the chemical-looping combustion (CLC) or chemical looping with oxygen uncoupling (CLOU). None of those processes involves gas separation and no additional separation work is needed for carbon capture. According to Peltola et al. [8] the 100 MW_{th} chemical looping combustion plant can achieve similar efficiency around 40% based on their simulation compared with modern steam power plants without CO_2 capture [9].

However major difficulties may come from the development of robust oxygen carriers and high temperature solid transfer equipment.

Type A-II uses a CO_2 carrier to react with CO_2 in the flue gas and CO_2 is collected after the carrier is heated up. Among those CO_2 carriers calcium oxide is mostly studied due to its high equilibrium capacity and low cost.

1.6.1 Calcium looping process with air separation unit

The calcium looping process (CLP) (Figure 1-10) uses fluidized beds that may be assumed to be well-mixed. Calcium oxide is used as a reactant to carry CO_2 between the carbonator and the calciner. Coal and pure oxygen are mixed and burned in the calciner to provide the heat to drive the $CaCO_3$ decomposition reaction in this idealized model. The chemical reactions are listed as:

$$CaO(\text{s}) + CO_2(\text{g}) \leftrightarrow CaCO_3(\text{s}) \quad \Delta H_r = -178 \ kJ/mol$$
$$C(\text{s}) + O_2(\text{g}) \longrightarrow CO_2(\text{g}) \quad \Delta H_c = -394 \ kJ/mol$$
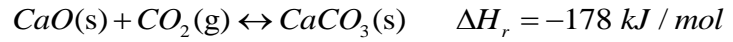
Since there is only one gas species involved in the first reaction, the equilibrium-state CO_2 partial pressure in the calciner and carbonator are functions of temperature according to the Van't Hoff equation:

$$\ln\left(\frac{K_{carb}}{K_{cal}}\right) = \frac{-\Delta H_r}{R}\left(\frac{1}{T_{carb}} - \frac{1}{T_{cal}}\right) = \ln\left(\frac{P_{CO_2}^{cal}}{P_{CO_2}^{carb}}\right) \tag{1.13}$$

while for the equilibrium coefficient we have:

$$P_{CO_2} = 1/K_{eq} = K_0 \exp\left(\frac{\Delta H_r}{RT}\right) \tag{1.14}$$
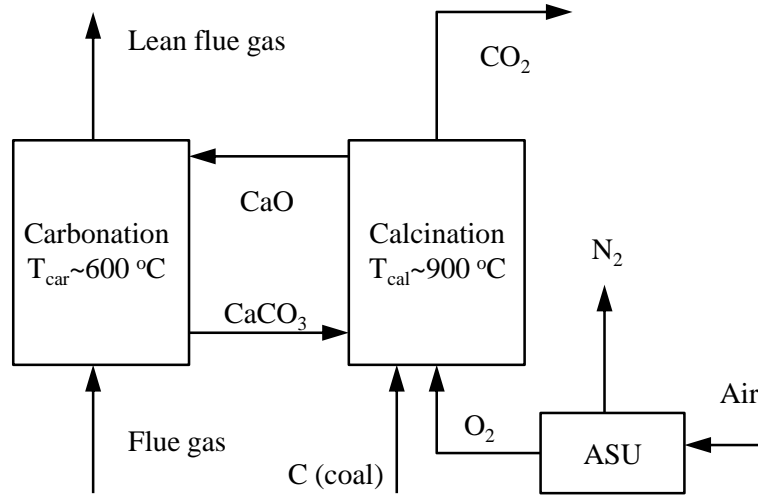
Figure 1-10 Calcium looping process for CO₂ capture (ASU: air separation unit)

Unlike the adsorption process, in which the lean flue gas composition is determined by the regeneration temperature, the lean flue gas composition of CLP is a function of the carbonator temperature. Substitution Eq. (1.2) into Eq. (1.14) yields the carbonator temperature as:

$$T_{carb} = \frac{\Delta H}{R} / \ln\left[\frac{y(1-r)}{1-yr}K_0\right] \tag{1.15}$$

For example the carbonator temperature of 653 °C is required if the feed flue gas is composed of 10% CO_2 and 90% recovery is targeted. Note that the temperature is very close to that of ultra-supercritical steam generation, a state-of-art steam cycle power generation process. Thus the heat provided in the calciner can be efficiently harvested in the carbonator using a supercritical steam cycle [10] as shown in Figure 1-11.

The minimum calciner temperature is fixed since the pure CO_2 is obtained at ambient pressure, which is estimated to be 1171 K when CO_2 partial pressure is at 1 atm according to Eq.(1.16).

$$T_{cal} = \frac{\Delta H}{R} / \ln\left(K_0 P_{atm}\right) \tag{1.16}$$

17

Lean flue gas

Steam
Coal
Air

Steam
Flue gas

CaCO₃ CaO

CO₂
O₂
Coal

N₂
Air

A. Boiler   B. Calcium looping process   C. Air separation unit (ASU)
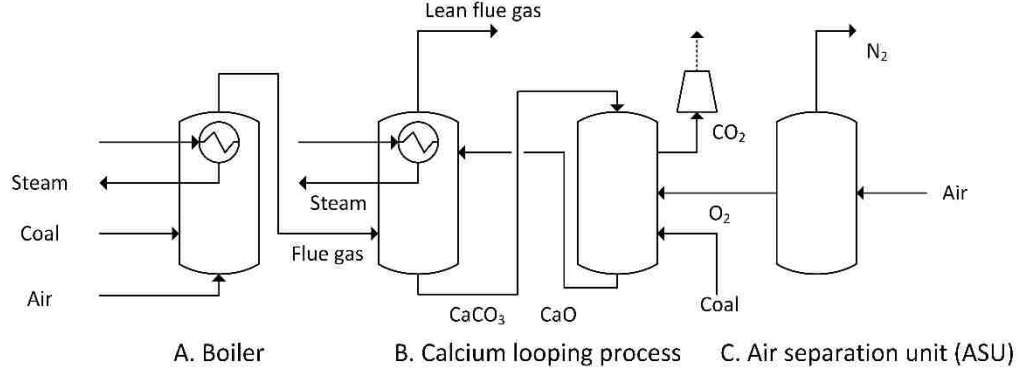
Figure 1-11 A coal-burning power plant retrofitted with a calcium looping process

The oxy-combustion heat equals the sum of the reaction heat to decompose calcium carbonate and the sensible heat to heat up calcium carbonate. Assume that the oxygen going into the calciner is completely consumed, the amount of O_2 and coal needed for combustion to capture 1 mol of CO_2 from flue gas is given by:

$$n_C = n_{O_2} = Q_{cal} / \Delta H_c = (c_{p,\text{CaCO}_3} \Delta T / n_{CO_2} + \Delta H_r) / \Delta H_c \qquad (1.17)$$

The thermodynamic minimum separation work for 1 mol O_2 is given by:

$$W_{O_2} = -RT_0 \left[\ln y_{O_2} + (1 - y_{O_2}) / y_{O_2} \ln(1 - y_{O_2}) \right] \qquad (1.18)$$

Assume that no energy is lost during the solid transport between the carbonator and the calciner, the total minimum equivalent work input for CLP to achieve the separation process in Fig. 1 is calculated using the definition of Carnot efficiency given in Eq. (1.9) :

$$W_{CLP}^{\min} = Q_{cal}(\eta_{cal} - \eta_{carb}) + n_{O_2} W_{O_2} = Q_{cal}(\frac{T_0}{T_{carb}} - \frac{T_0}{T_{cal}}) + n_{O_2} W_{O_2} \qquad (1.19)$$

1.6.2   Variances of calcium looping processes for CO_2 capture

In order to increase the process efficiency for CO_2 capture the following two process schemes are proposed and the results are analyzed here as an example to demonstrate our minimum work analysis.

18

1.1.1.1 Multi-stage fluidized bed process
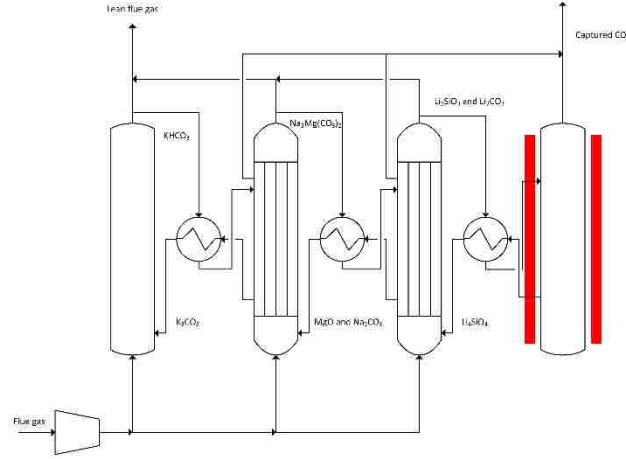
Figure 1-12 Conceptual diagram of the 3-stage fluidized bed carbon capture process

Kim et al. [11] recently reported a multi-stage fluidized bed process (Figure 1-12) with inter-stage heat integration to capture CO_2. The concept is based on utilizing sorbents working at different adsorption and regeneration temperatures so that one adsorbent can be regenerated by the heat released during the adsorption of another adsorbent. Assuming that no energy is lost during heat exchange, the minimum work required to capture 1 mol of CO_2 is calculated as:

$$W_{1-stage} = -\Delta H(\eta_{de} - \eta_{ad}) \tag{1.20}$$

For the 3-stage process:

$$W_{3-stage} = \frac{-n_1 \Delta H_1 \eta_{de1} - n_2 \Delta H_2(\eta_{de2} - \eta_{ad2}) - n_3 \Delta H_3(\eta_{de3} - \eta_{ad3})}{n_1 + n_2 + n_3} \tag{1.21}$$

where ΔH, η, n are the corresponding enthalpy change of adsorption, Carnot efficiency and amount of CO_2 being processed. As discussed in Kim et al.'s work [11] K_2CO_3, Na_2CO_3 promoted MgO and Li_4SiO_4 solid sorbents were selected for a 3-stage fluidized bed carbon capture process. Their properties are listed in Table 1-3.

Table 1-3 Physical properties of the sorbents used in the 3-stage carbon capture process and parameters for each stage

	K_2CO_3	Na_2CO_3 promoted MgO	Li_4SiO_4
Adsorption/desorption temperature (K)	323/443	543/723	823/1023
Heat of adsorption (kJ/mol)	137.4	122.4	140.0
Carnot efficiency η_{ad}	1-298/323	1-298/543	1-298/823
Carnot efficiency η_{de}	1-298/443	1-298/723	1-298/1023
Work required for a single stage $W_{1\text{-stage}}$ kJ/ mol captured CO_2	45.0	16.7	9.9
Feed flue gas split percentage (%)	32.2	36.2	31.6

The minimum work required for this 3-stage carbon capture process can be then calculated as W = 23.7 kJ/mol of captured CO_2, which is only lower than the required work for a single stage capture process using K_2CO_3. From the view of thermodynamics the multi-stage carbon capture process doesn't provide a more efficient process than a single stage process. However, a potential advantage is that it is a stand-alone process and does not require a steam turbine process to recycle the carbonation reaction heat.

1.1.1.2 *Three fluidized beds combustion system*
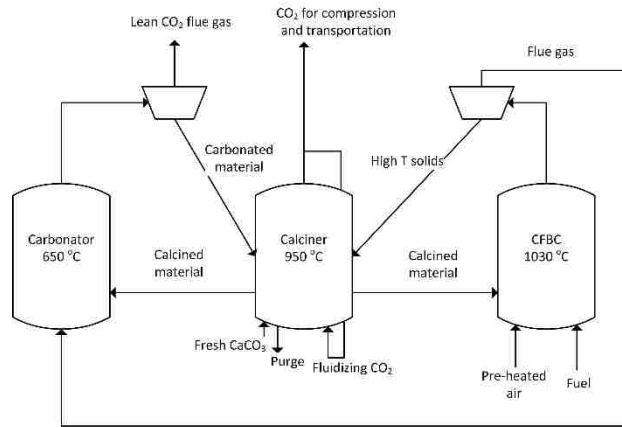
Figure 1-13 Process scheme of the three fluidized combustion system

Martínez et al. [12] proposed a three fluidized beds combustion system (Figure 1-13) using CaO as the CO_2 carrier and heat transfer solid between the carbonator, calciner and circulating fluidized bed combustor (CFBC). Compared with the calcium looping process (CLP) discussed before, this process doesn't require air separation unit (ASU) for oxy-combustion in the calciner. Instead the heat required in the calciner (950 $^{\circ}$C) is provided by high temperature solids (CaO) from the CFBC, where compressed air and fuel are mixed with calcined CaO from the calciner and combusted at 1030 $^{\circ}$C. Therefore, the main benefit of such a process is the reduction of air separation work. The minimum work required is obtained as:

$$W_{3-bed} = Q_{cal}(\eta_{cal} - \eta_{carb}) \qquad (1.22)$$

Compared with Eq. (1.19) the only difference is the reduction of the separation work for O_2, which is 3% of the separation work based on our previous calculation.

1.7 Comparison between temperature swing adsorption processes and chemical looping processes

Utilizing Eq. (1.11) and Eq. (1.19) we are able to compare the separation work between the TSA process using zeolite 13X as the adsorbent with the CLP using CaO as the CO_2 carrier. As shown in Figure 1-14 the equivalent work of separation varies with the feed flue gas composition y. The effects of capacity degradation for CLP are explored here. It is mentioned by Blamey et al. [10] that after 45 cycles of carbonation and calcination the sorption capacity of CaO drops to 0.316 g CO_2/g sorbent (40% conversion). As shown in Figure 1-14, the degradation results in higher work requirement due to more heat required to heat up the solids and more O_2 for oxy-combustion. Compared with TSA processes using zeolite 13x, CLP processes require less work for flue gas with low CO_2 concentration and there is a cross point where they require the same amount of work. For the ideal case where CaO is 100% reacted with CO_2 the cross point is when y = 8.4% and for degraded CaO the cross point is when y = 5.6%. Generally TSA processes require less work when y is higher than the cross point.
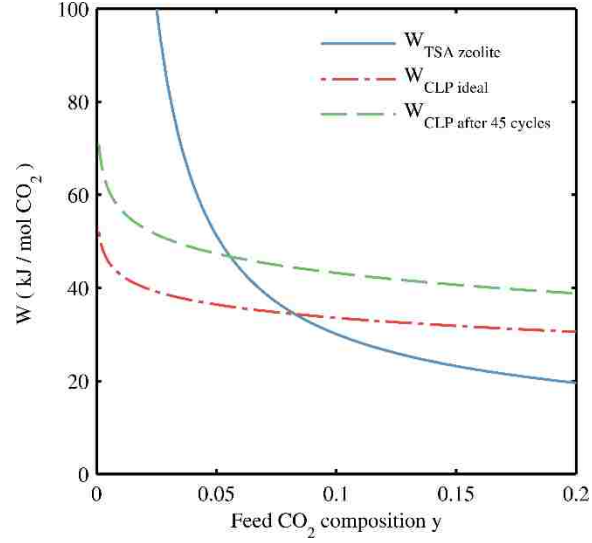
Figure 1-14 The equivalent work of separation for TSA using zeolite 13x and CLP using CaO when the recovery rate r = 0.9

The evaluation above is based on equivalent work required per unit of CO_2 captured from power plants, which does not consider the actual higher efficiency of oxy-combustion in the calciner and the benefits of producing extra CO_2 without the need for separation. An evaluation method based on the overall power plant efficiency after adding the carbon capture including the compression work is proposed here. Assume the overall efficiency η_p for a stand-alone supercritical power plant is around 38.5% and the same number is assumed for the steam generator in the carbonator. After adding the CLP, the overall efficiency can be calculated by:

$$\eta_{CLP} = \frac{(\Delta H_c + Q_{cal})\eta_p - (1 + n_c)W_{comp} - n_{O_2}W_{sep,O_2}}{(1 + n_c)\Delta H_c} \tag{1.23}$$

While for TSA the overall efficiency can be given by:

$$\eta_{TSA} = \frac{\Delta H_c \eta_p - \eta_{turbine}\eta_{Carnot}\left[c_p(T_{de} - T_{ad})/(n_1 - n_2) - \Delta H\right] - W_{comp}}{\Delta H_c}$$

$$\tag{1.24}$$

where the compression work is calculated by using a train of five (N_c) ideal gas adiabatic compressors with intermediate cooling and an isentropic efficiency of 75%. The final pressure equals 100 bar.

This yields:

$$W_{comp} = \frac{RT_0 N_c k}{(k-1)} \left[\left(\frac{P_{final}}{P_{atm}} \right)^{(k-1)/(\eta k N_c)} - 1 \right] \qquad (1.25)$$

with k=1.3 for carbon dioxide and the compression work turns out to be 18.5 kJ/mol CO_2.

As an example shown in Figure 1-15, η_{CLP} of stoichiometric capacity overlaps with that of degraded sorbents and remains nearly constant to be around 33%, while η_{TSA} is greatly increased from zero to 34% as the flue gas CO_2 concentration rises up to 10%. The conclusion is similar to that obtained with the equivalent work analysis: CLP remains more competitive with y less than 10% and TSA has an advantage when y becomes higher than 10%.
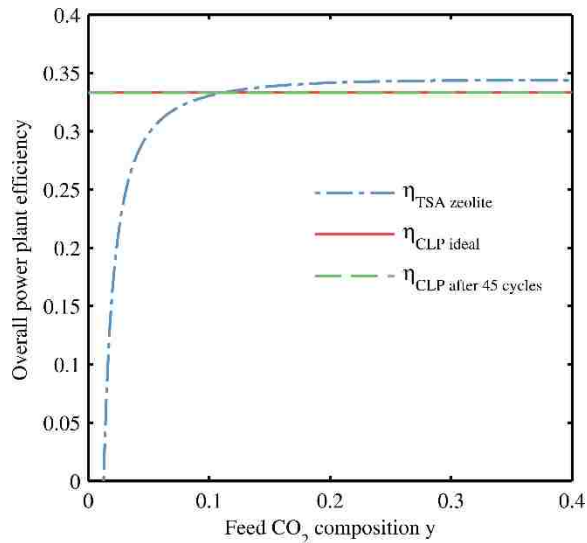
Figure 1-15 Comparison of overall power plant efficiency after adding CLP and TSA for carbon capture with varying flue gas composition and 90% CO_2 recovery (CO_2 is compressed to 100bar)

1.8 Conclusions

In this work we provided the expression to calculate the minimum work of separation for adsorption processes and applied the equation to the linear isotherm and the Langmuir isotherm. It was found that the adsorbent with the linear isotherm requires less minimum work of separation than that with the Langmuir isotherm. Moreover we analyzed the equivalent work needed for temperature swing adsorption processes and chemical looping processes. By using zeolite 13X and CaO the equivalent work required by those two processes are compared and calcium looping process is favored for low CO_2 concentration flue gas while temperature swing adsorption requires less energy for high CO_2 concentration flue gas. The point where the required work from both processes are equal depends on the extent of degradation of CaO. However due to the utilization of high temperature sensible heat and carbonation heat, the effects of degradation are hardly noticeable when it comes to the overall efficiency of power plants with carbon capture.

Simulation Study of Sorption Enhanced Reaction Processes

2.1 Introduction

A sorption enhanced reaction processes (SERP) is based on Le Chatelier's principle. By removing one or several species of the products, the reaction equilibrium is shifted towards the desired direction. Besides the improved conversion rate, another advantage is the reduction of equipment investment by combining reactors with separation processes. It is possible to drive a reversible reaction to near completion in a flow reactor by using a fixed bed packed with a selective adsorbent for one of the products and an appropriate catalyst, which provides an even higher conversion rate than that in a similar process using a well-mixed batch reactor.

This concept was reported as early as 1931 by Gluud et al. [13] for the production of hydrogen in the water gas shift reaction. More recently it was thoroughly reviewed by Carvill et al [14] in 1996 and Harrison in 2008 [15]. So far the most studied example is the hydrogen production by integration of reform or shift reaction catalyst with high temperature CO_2 adsorbents. It has been demonstrated experimentally in our laboratory and other groups [16-25] that high purity hydrogen can be produced by combining high temperature CO_2 adsorbents with corresponding water-gas-shift or steam-methane-reforming catalysts together in a fixed bed reactor.

A typical gas component profile for a long sorption enhanced WGS reactor is shown in Figure 2-1. For a fixed bed there are 4 zones: A. a reaction controlled zone, where fresh feed starts to react under the influence of both adsorption and reaction; B. an

equilibrium zone, where both reaction and adsorption reach equilibrium; C. a reaction mass transfer zone, where due to the contact of fresh adsorbent the reaction equilibrium is shifted again; D. an equilibrium zone, where unadsorbed product and excess reactant reach reaction equilibrium. In the case of WGS and SMR the excess reactant is steam and can be easily separated by condensation, thus high purity hydrogen is produced.
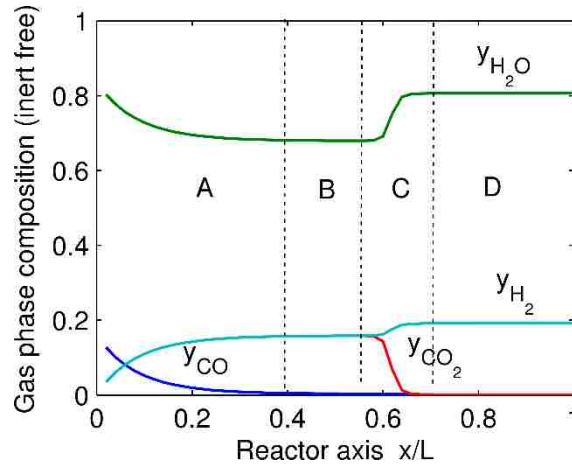
Figure 2-1 Typical gas species profile in a sorption enhanced reactor for water gas shift reaction (with 1000 times slower kinetics in order to demonstrate the reaction controlled zone) A: Reaction-controlled zone, B: Equilibrium-controlled zone, C: Reaction mass transfer zone, D: Equilibrium-controlled zone

Although many studies have been done on the modeling of the process performance [19, 26-29], little is known on how different factors affect the transient concentration front in the reactor. In this work we aim to investigate how the reaction and operating parameters affect those four zones. By investigating a more general reaction A + B -> C + D, we would like to answer under what circumstance sorption enhanced reaction principle can be applied to produce high purity product. Moreover by studying cases of hydrogen sulfide decomposition and propene metathesis and comparing it with the well-studied WGS reaction, we try to answer that whether other reactions have the similar profile in a sorption enhanced reactor. In order to focus on the reaction itself, local sorption equilibrium is assumed in all cases so that there is no mass transfer limitation.

The species concentration profile is determined by the reaction kinetics, stoichiometry, equilibrium constants and shape of sorption isotherm.

For WGS reaction various reaction rate expressions exist for different catalysts and so is for the sorption isotherms of various high temperature CO_2 adsorbents. Here a commercial $Cu/ZnO/Al_2O_3$ catalyst from Sud-Chemie, Inc. and K-promoted hydrotalcite from Air Products and Chemicals, Inc. are used for our sorption enhanced WGS reactor study [30]. While for sorption enhanced H_2S decomposition reaction molybdenum disulfide powder from VENTRON GmbH is used as the catalyst [31]. There is no literature data available for elemental sulfur adsorption, however, there are patents [32, 33] mentioning the use of an admixture of catalyst and sulfur adsorbent for removing sulfur moieties from Claus tail-gas. The process operates at 120-135 ℃ after the tail-gas is cooled down. Nevertheless in this work it is assumed that such an adsorbent could be designed and manufactured in the future and for modeling purposes a simple Langmuir isotherm model can be used to mathematically describe it. A series of studies has been done on sorption enhanced propene metathesis by Gomes et al. [34-36]. In their study rhenium oxide (Re_2O_7) supported on gamma-alumina (γ-Al_2O_3) was used as both the catalyst and adsorbent while zeolite 13X was used to preferentially adsorb butene and propene. It is studied here to show that the importance of the mass transfer during adsorption and the diffusion term in simulating sorption enhanced reactor.

2.2 Model description

Besides the instantaneous local sorption equilibrium assumption mentioned before, other assumptions made in the model are, isothermal operation, uniform pressure distribution, no radial concentration gradient, negligible axial dispersion, no mass

transfer resistance around catalyst and adsorbent and ideal gas behavior. As a result the total concentration in the reactor is the same everywhere, C=P/RT. The corresponding equations are:

Mass balance equation for individual species in the gas phase is given by:

$$\varepsilon C \frac{\partial(y_i)}{\partial t} = -\varepsilon C \frac{\partial(vy_i)}{\partial z} + \rho_c \alpha_i R - \rho_a \frac{\partial n_i}{\partial t} \qquad (2.1)$$

Adding all species up yields:

$$0 = -\varepsilon C \frac{\partial v}{\partial z} + \rho_c \Delta \alpha R - \rho_a \sum \frac{\partial n_i}{\partial t} \qquad (2.2)$$

The sorption isotherm can be expressed as:

$$n_i = F(y_i) \qquad (2.3)$$

and

$$\frac{\partial n_i}{\partial y_i} = f(y_i) \qquad (2.4)$$

Mass balance of the adsorbed phase:

$$\frac{\partial n_i}{\partial t} = \frac{\partial n_i}{\partial y_i} \frac{\partial y_i}{\partial t} = f(y_i) \frac{\partial y_i}{\partial t} \qquad (2.5)$$

2.3 Study on the water gas shift (WGS) reaction

According to Choi and Stenger [37] the reaction kinetics of WGS reaction on the Cu/ZnO/Al$_2$O$_3$ catalyst described before is given by:

$$R_{WGS} = K_r \left(P_{CO} P_{H_2O} - P_{CO_2} P_{H_2} / K_{eq} \right) \qquad (2.6)$$

where $K_r = K_{r0} \exp [H_r/(RT)]$ and the reaction equilibrium rate K_{eq} [38] can be expressed as shown in Table 2-1.

The adsorption isotherm is obtained from Lee et al.'s work [39]:

$$n_{CO_2} = \frac{mk_c P_{CO_2} \left[1 + (a+1)k_a P_{CO_2}^a \right]}{1 + k_c P_{CO_2} + k_c k_a P_{CO_2}^{a+1}} \qquad (2.7)$$

where $K_c = K_{c0} \exp[q_c/(RT)]$ and $k_a = k_{a0} \exp[q_a/(RT)]$. Jang et al. [40] made a modification on the expression of a so that it becomes a function of temperature. The parameters are listed as in Table 2-1.

Table 2-1 Parameters for WGS reaction kinetics and equilibrium information and CO₂ adsorption isotherm on K-promoted hydrotalcite

K_{r0}, mol/(s·kg·atm)	$3.302*10^7$
H_r, kJ/mol	-67.13
m, mol/kg	0.25
K_{c0}, atm^{-1}	0.8778
q_c, kJ/mol	21.00
a	$0.285*\exp(12200/RT)$
k_{a0}, atm^{-a}	$1.34*10^{-3}$
q_a, kJ/mol	42.13
K_{eq}	$\exp(5693.5/T+1.077\ln T+5.44E\text{-}4T-1.125E\text{-}7T^2-49170/T^2-13.148)$

Jang et al. [40] studied the same sorption enhanced reaction system experimentally and with a numerical model based on reactor energy balance for temperature effects, linear driving force (LDF) model for mass transfer during adsorption and reaction kinetics. Since the reactor diameter they used is small (1.73 cm) and the reaction is only moderately exothermic (ΔH = -41.1 kJ/mol), we can assume an isothermal condition during the operation. Moreover the mass transfer coefficient is sufficiently large (k_{ldf} = 3 min^{-1}) so that the local equilibrium model can be applied in this case.

The reactor was packed with 50:50 catalyst and adsorbent by weight and detailed information is listed in Table 2-2. The reactor was initially filled with steam and argon. Due to the void volume of the test setup and the response time of detectors, a 3.9 min delay is used to account for the time it takes before hydrogen appears at the exit of the reactor.

A first order upwind finite difference method is used to discretize the reactor. The resulting stiff ordinary differential equations are solved by a build-in function ode15s in

Matlab. The effects of the number of grids (N) used for the simulation are explored in Figure 2-2, where the bed properties and operating conditions are the same as those used for the experiments except the feed gas is set as equal molar ratio of CO and H_2O. When N is above 200 little effect is observed on the shape of the effluent curve. Therefore in the following discussion all the simulation were performed with N = 200 unless otherwise specified

By changing the feed composition to the experimental value, the simulation results of our model match the reported experimental results well as shown in Figure 2-3. As is discussed later in our study the shape of the effluent gas composition profile is determined by the WGS reaction kinetics and equilibrium parameters and CO_2 adsorption isotherm shape. In the experimental study all parameters are in favor of the formation of high purity H_2 product and a sharp breakthrough curve.

Table 2-2 Reactor information and operation parameters for the base case of WGS reaction

ρ_{cat}, kg/m3	410
ρ_{ads}, kg/m3	410
ε	0.6
ID, cm	1.73
L, cm	50.2
P, atm	1
T, K	673.15
F_{CO}, ml/min (STD)	50
F_{H2O}, ml/min (STD)	258.6
F_{Ar}, ml/min (STD)	150
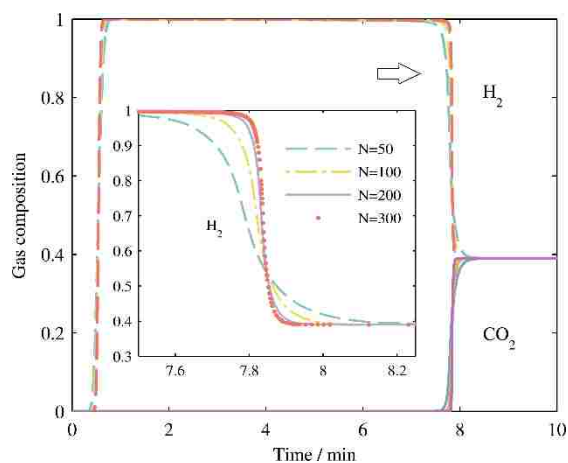
Figure 2-2 The influence on the shape of effluent curves by increasing the number of grids used for the simulation
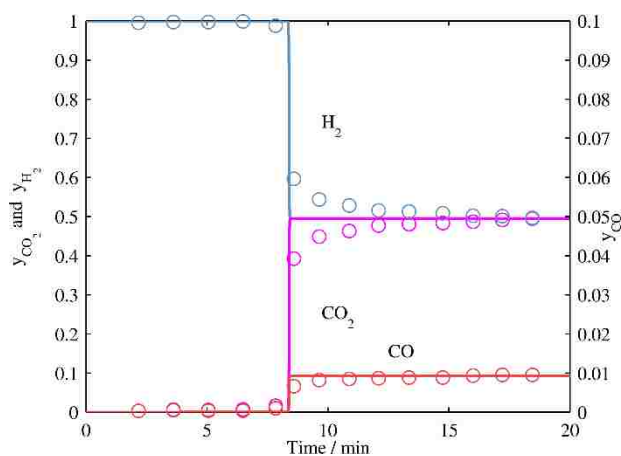
Figure 2-3 Comparison of effluent gas composition (dry and argon free) from a SEWGS reactor using K-promoted hydrotalcite at 400 ºC; symbols: experimental data, lines: simulation results.

2.3.1   Results and discussion

The reason of obtaining pure H_2 in the SEWGS reactor as shown in Figure 2-3 is because there is a large excess of steam. For a more general reaction A + B -> C + D, if C is adsorbed we are interested in whether high purity D can be produced. The SEWGS reactor can be studied as an example and the question now evolves into whether it is

32

possible to produce H_2 without the use of excessive H_2O. The only way to do that is using the stoichiometric ratio of H_2O and CO in the feed. Jang et al. [40] studied the effect of H_2O/CO ratio and noticed that the H_2 productivity increased dramatically around the minimum stoichiometric ratio of 1.0, which was explained by the thermodynamics of the WGS reaction. Here we also studied the case where $F_{CO} = F_{H2O}$ = 50 sccm (standard cm^3 per minute), $F_{Ar}=0$ and the bed is prefilled with argon. As shown in Figure 2-4, high purity H_2 is available without the need of water condensation in this case. Therefore using a stoichiometric feed components ratio can reduce the need of product separation for a sorption enhanced reactor. We will limit to the stoichiometric feed components ratio for the following discussion on the effects of other parameters.
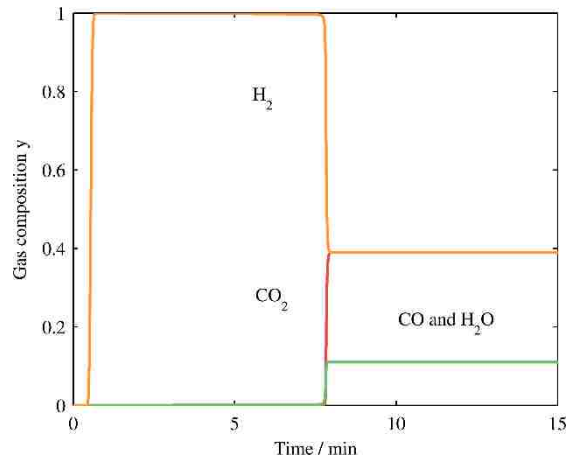
Figure 2-4 Effluent gas composition profile at the end of the SEWGS reactor when $F_{CO}=F_{H2O}$ (base case: $K_{eq} = 12.5$, $K_r = 203.9$ mol/(s•kg•atm) and $K_c = 37.4$ atm^{-1})

2.3.1.1 Effects of the reaction equilibrium constant

As mentioned previously high purity H_2 is available because of the formation of the equilibrium zone near the exit of the reactor shown in Figure 2-1. According to the equilibrium constant expression in Table 2-1 the reaction equilibrium constant K_{eq} at 400 °C is estimated to be 12.5. In order to study the effects of K_{eq} on the H_2 product

purity, two cases were studied here in which K_{eq} became 1/10 and 1/100 of its original value. The H_2 profiles at different equilibrium values are shown in Figure 2-5. As we reduce the value of the equilibrium constants the concentration of H_2 is reduced in general, which reflects that the concentration front inside the reactor becomes more stretched as shown in Figure 2-6. Inside the reactor due to the large value of the reaction kinetics constant K_r the reaction controlled zone is too small to be observed and as we reduce the value of K_{eq} the reaction mass transfer zone extends to the equilibrium zone at the reactor exit. According to Figure 2-8 the impurities are mostly unreacted CO and H_2O while the CO_2 profile also seems to be affected but not as much as that of the other components.
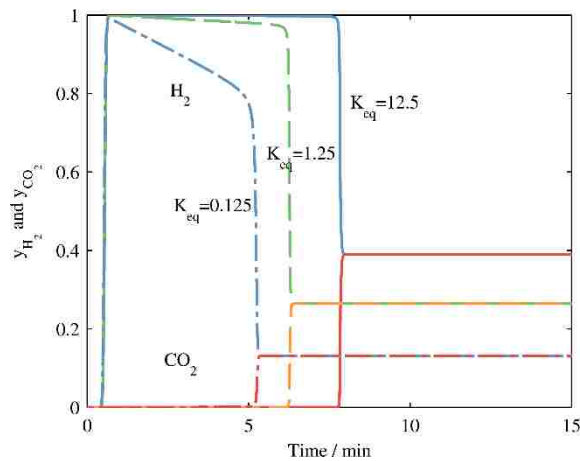
Figure 2-5 Effects of different reaction equilibrium constants on the hydrogen profile where K_r = 203.9 mol/(s•kg•atm) and K_c = 37.4 atm^{-1}
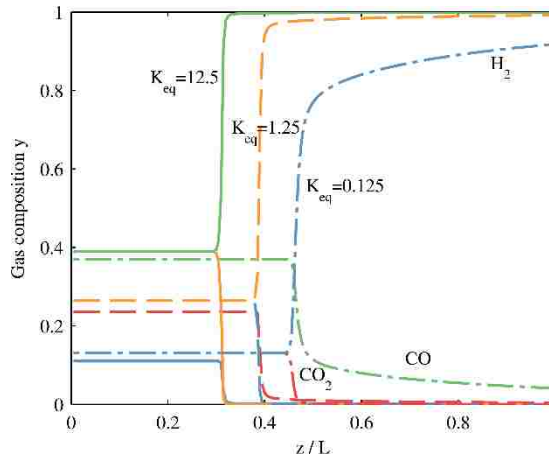
Figure 2-6 Effects of different K_{eq} on the CO concentration profile inside the reactor when t = 146 sec, K_r = 203.9 mol/(s•kg•atm) and K_c = 37.4 atm^{-1}

To explore the reason for stretched hydrogen profile after reducing the value of K_{eq}, the following explanation is proposed. It is well known [41] that the velocity of the concentration front for adsorbates with the Langmuir isotherm model will form a shock wave inside the bed if the bed is long enough, which is the base for the constant pattern model. However when the adsorbate concentration is low, the Langmuir model will approach a linear isotherm model, which results in a less compressed concentration front. In sorption enhanced WGS reaction if K_{eq} is high enough so that the concentration of the adsorbate, also as one of reaction products, inside the bed becomes reasonably high, the same principle can be applied here to form a sharp reaction mass transfer zone, which results in high purity hydrogen product. If, however, the value of K_{eq} is low so that the adsorbate concentration inside the bed lies in the region making the adsorption isotherm close to the linear isotherm, a stretched reaction mass transfer zone will form, resulting in the lack of high purity hydrogen product.
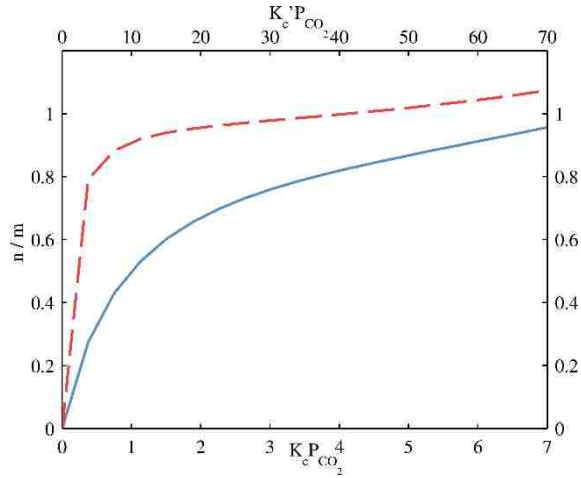
Figure 2-7 Dimensionless plot of the CO₂ adsorption isotherm of K-promoted hydrotalcite at 400 °C when Kc = 37.4 atm⁻¹ (solid line and bottom x-axis) and 374 atm⁻¹ (dash line and top x-axis)

When K_{eq} is reduced to 0.125, the equilibrium molar fraction of CO_2 in the saturated region (Section B) was reduced from 0.39 (base case) to 0.13. The CO_2 concentration in the reactor moves into the linear section of the adsorption isotherm according to the isotherm shown in Figure 2-7. To verify this hypothesis the value of K_c was increased from 37.4 atm⁻¹ to 374 atm⁻¹ and the modified isotherm is also shown in Figure 2-7. After increasing the value of K_c the equilibrium concentration of CO_2 in the reactor no longer lies in the linear region. Therefore the adsorption front is more likely to form a sharp reaction zone. The simulation results for the case where $K_{eq} = 0.125$ and $K_c = 374$ atm⁻¹ are compared with that where $K_{eq} = 0.125$ and $K_c = 37.4$ atm⁻¹. As shown in Figure 2-8 the concentration of hydrogen in the product gas is greatly improved by increasing the value of K_c.
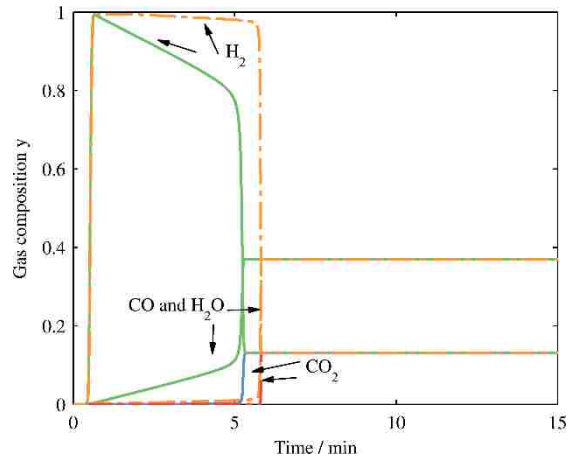
Figure 2-8 Reactor exit gas composition profiles with different values of K_c: solid lines – Kc = 37.4 atm^{-1} dashed lines – K_c = 374 atm^{-1} (K_{eq} = 0.125 and K_r = 203.9 mol/(s•kg•atm))

Although the shape of the adsorption isotherm is found to be the main factor that affects the effluent profile, as we reduce the value of K_{eq} the adsorbate concentration is reduced and approaches the linear section of the isotherm. Another effect of reducing the value of K_{eq} is that the reaction rate (Eq (2.6)) is also reduced, which changes the shape the reaction mass transfer zone. We will discuss the effects of reaction kinetics on the shape of the reaction mass transfer zone in the following section.

2.3.1.2 Effects of the reaction rate constant

The reaction rate constant K_r used in Eq (2.6) at 400 ^{o}C is around 203.9 mol/(s·kg·atm). Again we compared the effluent concentration profile after smaller K_r values are applied while keeping the other parameters unchanged. It is observed in Figure 2-9 that reducing the value of K_r has limited effects on the effluent profile when K_r is between 2 and 200 mol/(s·kg·atm). When K_r becomes smaller than 2 mol/(s·kg·atm) the H_2 concentration starts to decrease over the whole time period. The reason for that can be explained by the formation of the reaction controlled zone at the reactor entrance. When K_r is so small that it takes more than the whole length of the reactor to fully develop the reaction controlled zone, the equilibrium zone between the

reaction controlled zone and the reaction mass transfer zone will be eliminated and the equilibrium zone near the exit of the reactor becomes part of the reaction mass transfer zone as shown in Figure 2-10.

Also shown in Figure 2-10 is that the molar fraction of CO forms a small peak in the reaction mass transfer zone after the value of K_r is reduced below 0.2 mol/(s·kg·atm), which is a combined result of adsorption and reaction. When there is only adsorption, after CO_2 is taken away from the gas phase the molar fractions of the other 3 species increase simultaneously. When reaction comes into play if the reaction rate is fast, the equilibrium will instantaneously be shifted to the forward WGS reaction, thus reducing the molar fraction of CO and H_2O while increasing that of H_2. Competition between adsorption and reaction happens at the reaction mass transfer zone, where when CO_2 concentration is high adsorption dominates and when CO_2 concentration is low reaction dominates. The peak corresponds to the transition between those two regions.
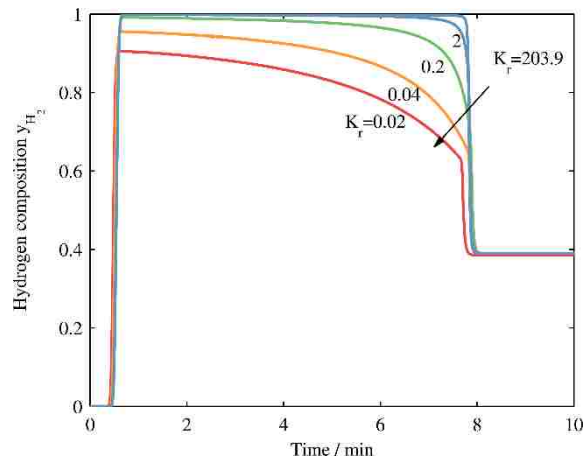
Figure 2-9 Effluent H_2 concentration profile when K_r is reduced from 203.9 to 0.02 mol/(s·kg·atm), K_{eq} = 12.6, and K_c = 37.4 atm^{-1}
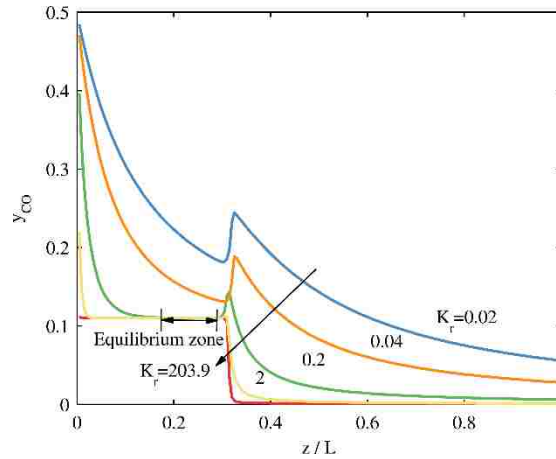
Figure 2-10 CO percentage inside the reactor when t=146.3 sec, K_{eq} = 12.6, and K_c = 37.4 atm^{-1} after reducing K_r from 203.9 to 0.02 mol/(s kg atm)

It is demonstrated in Figure 2-11 that when K_r equals 0.04 the reaction controlled zone slowly develops with time in the reactor and after 400 sec the components reach reaction equilibrium near the reactor exit. Therefore there is not enough bed space for the concentration front to develop the sharp reaction zone and a longer reactor is needed to obtain high purity hydrogen. By increasing the reactor length from 0.5 m to 1 m (the number of computational nodes was increased from 200 to 400) high purity hydrogen is again available from the reactor as shown in Figure 2-12. Although the reaction rate is still slow the increased reactor length enables the formation of a stable reaction mass transfer zone and thus the high purity hydrogen. Interestingly the shape of the product profiles are not changed by increasing the length of the reactor as shown in Figure 2-13.
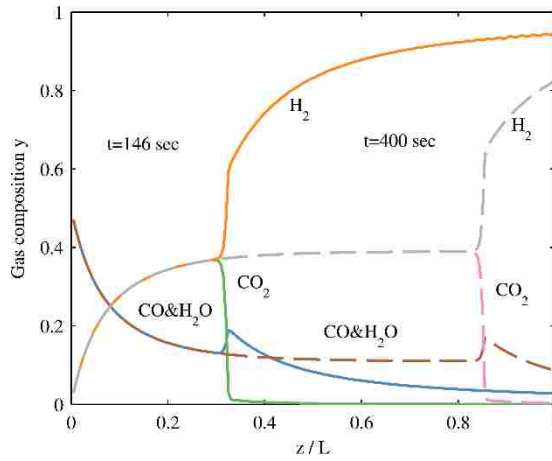
Figure 2-11 Components profile inside the reactor at t=146 sec (solid lines) and t = 400 sec (dashed lines) when $K_r = 0.04$ mol/(s·kg·atm) $K_{eq} = 12.6$, and $K_c = 37.4$ atm^{-1}
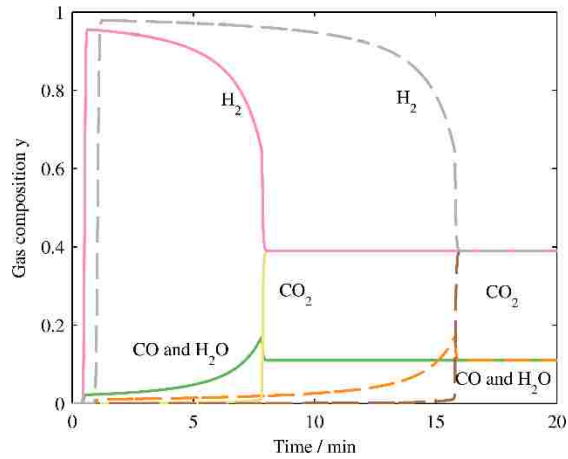
Figure 2-12 Effects of reactor length to the product profiles when $K_r = 0.04$ mol/(s·kg·atm) $K_{eq} = 12.6$, and $K_c = 37.4$ atm^{-1} (solid lines: L = 0.5 m, dashed lines: L = 1 m)
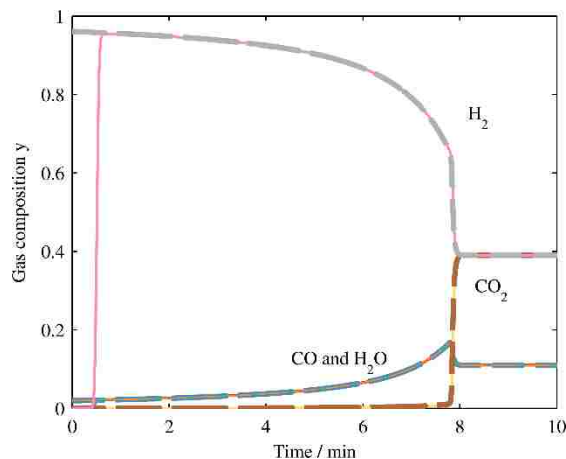
Figure 2-13 Comparison of the product profile shapes of different reactor lengths after shifting the time frames when K_r = 0.04 mol/(s kg atm) K_{eq} = 12.6, and K_c = 37.4 atm^{-1} (solid lines: L = 0.5 m, dashed lines: L = 5 m)

2.3.1.3 Effects of the isotherm model constant

The only way that adsorption affects the reactor performance in this model is through the adsorption isotherm model. The rather complex isotherm model (Eq. (2.7)) used before can be approximated by the Langmuir isotherm model as $n = mK_cP/(1+K_cP)$ when the partial pressure of CO_2 is relatively small. By changing the value of K_c we can explore the effects of interaction strength between the adsorbate and adsorbent on the SEWGS reactor performance. Initially K_c equals 37.4 atm^{-1} at 400 ^{o}C, which implies relatively strong interaction between CO_2 and K-promoted hydrotalcite. By reducing K_c the isotherm model tends to be closer to a linear isotherm and a weaker interaction force. If there is only adsorption happening the breakthrough curve for CO_2 will be stretched resulting in a longer reaction mass transfer zone. Another direct effect is the equilibrium CO_2 capacity in the reactor will be reduced causing shorter breakthrough time. The results are shown in Figure 2-14.
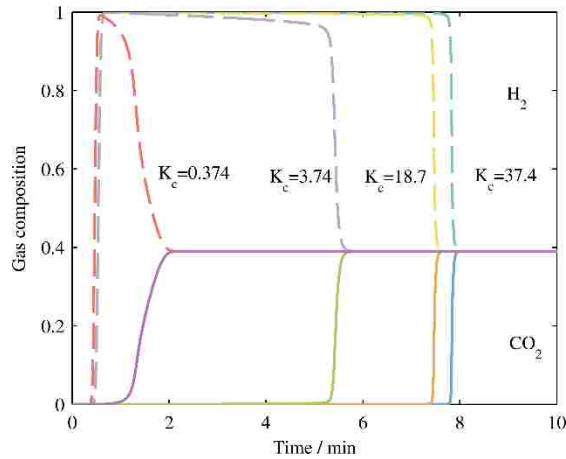
Figure 2-14 Effluent composition with different values of the adsorption constant K_c when K_{eq} = 12.6 and K_r = 203.9 mol/(s•kg•atm)

2.4 Study on the sorption enhanced H_2S decomposition reaction

Up until now the most important factors like reaction equilibrium, reaction kinetics and adsorption isotherm when designing a sorption enhanced reactor have been covered. Another factor we would like cover is the reaction stoichiometry. From the studied SEWGS reactor it is clear that high purity product is available for a generalized reaction A + B -> C + D as long as all the factors mentioned before are in an appropriate range. It is of interest to find if the conclusions reached for WGS reaction can be extended to a reaction stoichiometry like A -> B + ½C, as in the H_2S decomposition reaction H_2S -> H_2 + ½ S_2.

It is proposed by Raymont [42] that instead of using the Claus process to eliminate the emission of H_2S it is more economical to be use H_2S as a source to produce hydrogen. Among the many different ways to decompose H_2S, the most promising one is suggested to be the catalytic decomposition [43]. There are many studies [31, 44-47] focused on using transitional metal sulfides as catalyst to facilitate H_2S decomposition.

In this study we will focus on using molybdenum disulfide due to its relatively high activity and stability [31].

The same assumptions are made here as that for the previously discussed SEWGS reactor. Besides Eq (2.1)-(2.5) the reaction kinetics equation and adsorption isotherm equation are still needed. The thermodynamics information on H_2S decomposition reaction is summarized by Kaloidas and Papayannakos [48]. The reaction equilibrium constant is calculated based on the Van't Hoff equation and can be expressed as:

$$K_{eq} = a \exp\left(\frac{b}{RT}\right)$$ (2.8)

where a and b equal 323.3 and -9.006E4 respectively.

The kinetics data for catalytic H_2S decomposition are obtained from another work by Kaloidas and Papayannakos [31] and a Hougen-Watson adsorption model, shown in the following equation, is used to calculate the reaction rate.

$$R = K_r \cdot \frac{(Py_{H_2S} - (1/K_{eq})P^{1.5}y_{H_2}y_{S_2}^{0.5})}{(1 + K_{H_2S}Py_{H_2S} + K_{S_2}P^{0.5}y_{S_2}^{0.5})}$$ (2.9)

where K_r = 4.33E4 exp (-9.01E4/RT), K_{H2S} = 9.75E-7 exp (2.16E5/RT) and K_{S2} = 17.03 exp (1.02E5/RT). Since no literature data are available for a S_2 adsorbent, a Langmuir isotherm model is used here:

$$n_{S_2} = \frac{mK_cP}{1 + K_cP}$$ (2.10)

where m = 1.6 and K_c = 6E-8 exp (1.3E5/RT).

The reactor and operating information is summarized in Table 2-3:

Table 2-3 Reactor information and operating parameters for the base case of H₂S decomposition

ρ_{cat}, kg/m3	500
ρ_{ads}, kg/m3	500
ε	0.6
ID, cm	1.73
L, cm	50
P, atm	1
T, K	1200
F_{H2S}, ml/min (STD)	70

2.4.1　Results and discussion

The effluent profile of the base case is shown in Figure 2-15. The composition profile shows that after around 120 sec the profile reaches equilibrium, which implies around 20% conversion rate for H₂S. Although enhancement on the reaction conversion is observed for the first minute, the results are not promising to produce high purity H₂. From the conclusions we have reached for SEWGS reactor study we can improve the reactor performance by improve the properties of the catalyst and adsorbent.
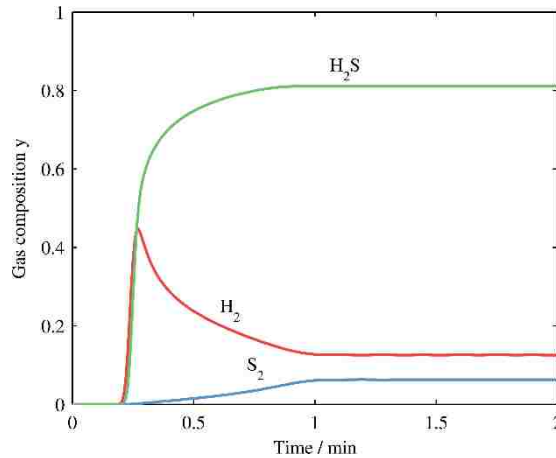
Figure 2-15 Effluent composition of the base case for the sorption enhanced H₂S decomposition reaction where K_r = 3.64E4 mol/(s kg atm) K_{eq} = 0.039, and K_c = 0.0328 atm⁻¹

Under the conditions of the base case the equilibrium molar fraction of S₂ after the bed is saturated is around 0.063 and the adsorption capacity is at 3.3E-3 mol/kg, which is quite small compared with that of CO₂ on K-promoted hydrotalcite. Therefore three

44

cases of increasing K_c by 100, 10,000 and 100,000 times are studied and the corresponding isotherms are shown in Figure 2-16. By increasing the value of K_c the equilibrium capacity for S_2 is increased by 3 orders of magnitude and the shape of the isotherm becomes more favorable. It is shown in Figure 2-17 that only after we increased the value of K_c to 32,800 atm^{-1} the hydrogen profile becomes sharp when S_2 starts to breakthrough.
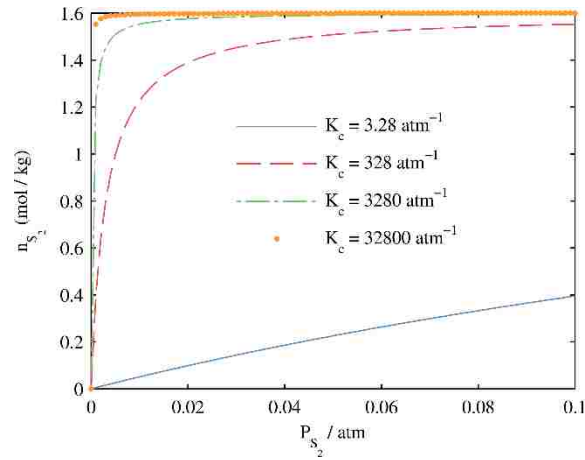
Figure 2-16 Adsorption isotherm for S_2 with different values of K_c (when K_c = 0.0328 the isotherm almost overlaps with the x-axis)
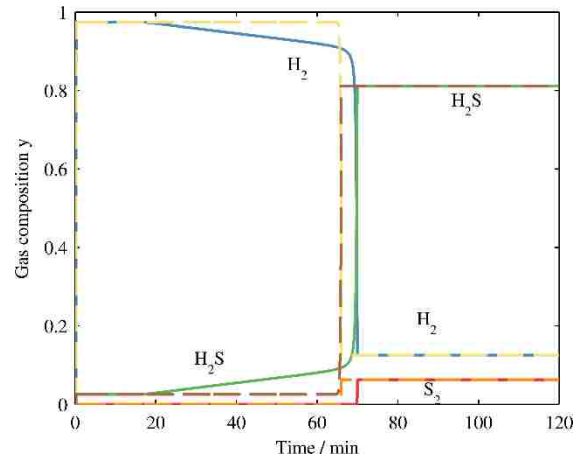
Figure 2-17 Effluent profiles of the sorption enhanced H_2S decomposition reactor after K_c is increased, (solid lines: K_c = 3280 atm^{-1}, dashed lines: K_c = 32800 atm^{-1})

Also noticed is that the highest hydrogen concentration is limited to a certain value around 97.5%, which is due to the H_2S formation by the reaction of initial S_2 with the rich H_2 product. The initial species molar fraction was set as 1E-6, which works fine for the sorption enhanced water gas shift reaction (WGS) simulation. However, for sorption enhanced hydrogen sulfide decomposition simulation that tiny amount of S_2 would react with 97.5% hydrogen and form 2.5% H_2S in the collected hydrogen product. The stoichiometric parameters for the elementary reaction of H_2S decomposition is the main cause of this. In order to achieve high purity another case with initial S_2 molar fraction of 1E-12 was studied and the reactor effluent profile is shown in Figure 2-18.
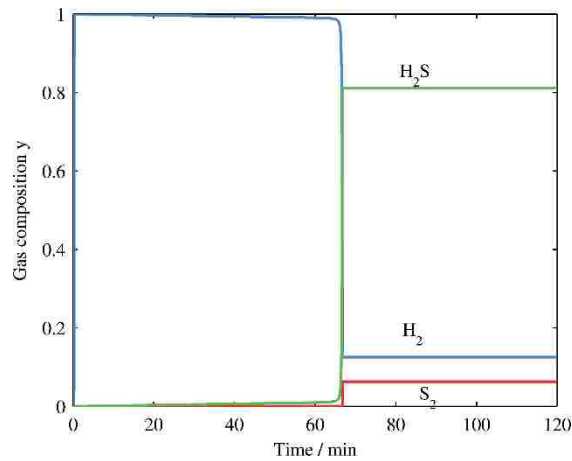
Figure 2-18 Effluent profiles of the sorption enhanced H₂S decomposition reactor after y_{S2}^0 is reduced from 1e-6 to 1e-12 where K_r = 3.64E4 mol/(s kg atm) K_{eq} = 0.039 and K_c = 32800 atm^{-1}

On the other hand we explored the effects of reaction kinetics by increasing the reaction rate K_r by 100 times. As shown in Figure 2-19 there is no noticeable difference between the concentration profiles before and after we increase the value of K_r. Therefore the reaction kinetics is not the limiting factor in this case. We then explored the effects of the reaction equilibrium constant. As mentioned previously in the discussion of the sorption enhanced WGS reactor the reaction equilibrium constant can affect the effluent profile from both adsorption and reaction perspectives. The results in

Figure 2-20 shows that the reaction equilibrium constant is a limiting factor to produce high purity H_2 by sorption enhanced H_2S decomposition reaction. Also noticed is that after increasing the value of K_{eq} high purity hydrogen becomes available even with y_{S2} = 1e-6. It confirms our previous conclusion based on SEWGS reaction that in order to produce high purity product all the factors including reaction kinetics, thermodynamic equilibrium and adsorption isotherm need to be considered and each factor determines the reactor performance in a different way.
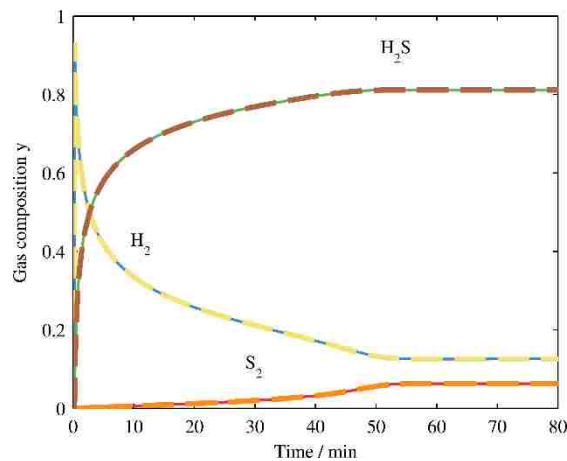
Figure 2-19 Comparison of effluent profiles of the sorption enhanced H_2S decomposition reactor after increasing the reaction rate constant where K_c = 3.28 atm^{-1} and K_{eq} = 0.039, solid lines: K_r = 3.64E4 mol/(s kg atm), dashed lines: K_r = 3.64E6 mol/(s kg atm)
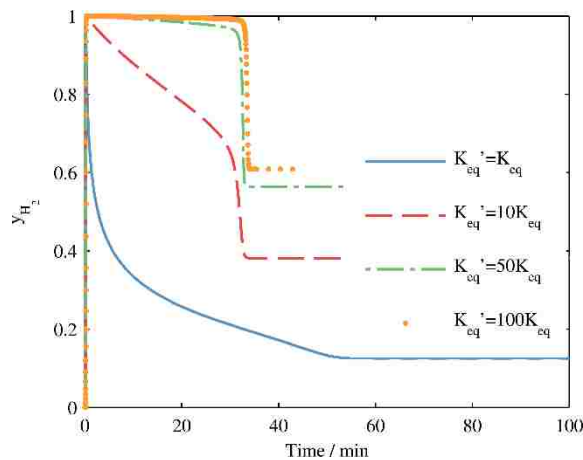
Figure 2-20 Effluent profile of the sorption enhanced H_2S decomposition reaction with various values of Keq where K_c = 3.28 atm^{-1} and K_r = 3.64E4 mol/(s kg atm)

2.5 Study on the sorption enhanced propene metathesis reaction

Olefin metathesis reaction allows the mutual exchange of alkylidene groups between two substituted alkenes. It is widely applied in olefins production process to obtain olefins with desired number of carbon atoms and the polymerization of olefins [49]. Propene metathesis (the Phillips Triolefin Process) is a key industrial scale olefin metathesis reaction, which can either produce propene or ethene depending on the market demand.

$$2CH_2 = CH - CH_3 \leftrightarrow CH_2 = CH_2 + CH_3 - CH = CH - CH_3$$
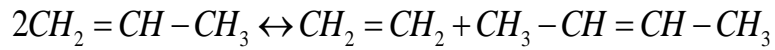
The sorption enhanced propene metathesis reaction is proposed to improve the propene conversion for this equilibrium controlled reaction by using an adsorbent (zeolite 13X) to selectively remove butene. It was found out [35] that by operating the sorptive reactor in a cyclic fashion similar to a two-bed pressure swing adsorption cycle, the product yield and catalyst/adsorbent productivity was improved. A one-pass experiment with only the rhenium oxide (Re_2O_7) impregnated gamma-alumina (γ-Al_2O_3) packed was conducted to verify the reactor model developed by Rawadieh et al. [34]. Here we try to compare their experimental results with our own model which neglects all mass transfer resistance and diffusion terms.

There is one change that needs to be made for this process, the adsorption isotherm model. Since all three species are adsorbed on γ-Al_2O_3, a multicomponent Langmuir isotherm model is used and is written as:

$$n_i = n_{is} \frac{b_i c_i}{1 + \sum b_i c_i} \tag{2.11}$$

where n_{is} and b_i are listed in Table 2-4. Therefore, Eq. (2.5) is rewritten as:

$$\frac{\partial n_i}{\partial t} = \frac{\partial n_i}{\partial c_i} \frac{\partial c_i}{\partial t} + \frac{\partial n_i}{\partial c_j} \frac{\partial c_j}{\partial t} + \frac{\partial n_i}{\partial c_k} \frac{\partial c_k}{\partial t} \tag{2.12}$$

The reaction kinetics was studied by Gomes and Fuller [36] and is expressed as:

$$Rct = \frac{K_r\left(c_p^2 - c_b c_e / 0.0397\right)}{c_p + 0.172 c_p^2 + 2.309 c_e + 2.727 c_b + 0.398 c_p c_e + 0.469 c_p c_b} \quad (2.13)$$

where K_r equals 6.34E-2 mol/kg/sec. The bed properties and operating conditions can

be found in Table 2-5.

Table 2-4 The adsorption isotherm parameters of ethane, propene and butene on γ-Al₂O₃

	Ethene	Propene	Butene
n_{is}, mol/kg	0.1836	0.4106	0.8144
b_i, m³/mol	239.7	332.6	514

Table 2-5 Packed bed properties and operating conditions

Reactor radius, m	5E-3
Reactor length, m	0.0805
Bed density, kg/m³	711
Bed voidage	0.608
Pressure, atm	1
Temperature, K	291
Feed flow rate, sccm	1520
Feed composition, %	Propene/Nitrogen 5/95

2.5.1 Results and discussion

The simulation results are shown in Figure 2-21, where the dimensionless time is

calculated as $t v_0 / L$. The effluent composition after the bed is saturated with the feed

shows the simulation data is close to experimental data. However, the breakthrough

curves are far from satisfactory. Especially our model predicts a rather significant

enhancement of ethene concentration, while the experimental results show the ethene

concentration remains constant after the breakthrough. Moreover the butene

breakthrough curve appears ealier than the experimental data, which is also observed

when comparing simulation results with experimental data by Rawadieh et al. [34]. It

was suggested that using pure gas isotherm parameters instead of measuring the mixture isotherm parameter contribute to this breakthrough time error.

In an attempt to modify different parameters in order to match the experimental results, the best match was found by reducing the kinetic parameter K_r by 20 times shown in Figure 2-22. It is shown that the enhancement on ethene concentration was less obvious and the breakthrough curve for propene is now closer to the experimental results.
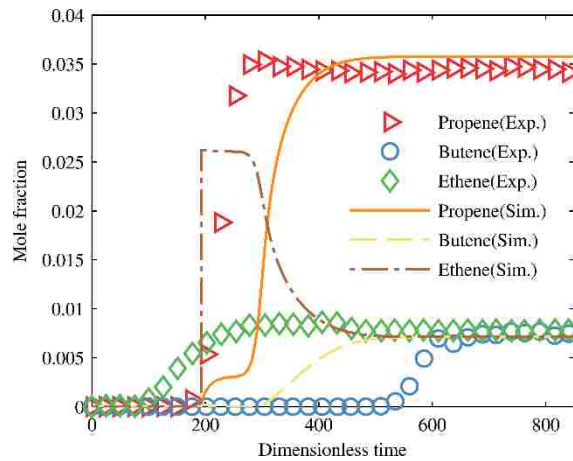
Figure 2-21 Comparison of the experimental results and our simplified model
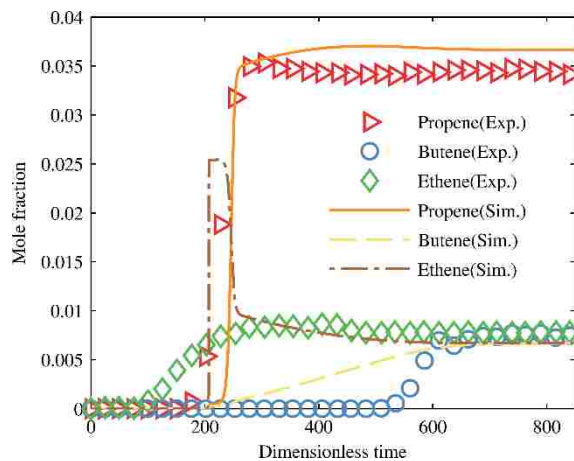
Figure 2-22 Comparison of the experimental results and the simplified model when K_r is reduced by 20 times

Comparing our model results with the model by Rawadieh et al. [34] it is found out that mass transfer resistance does play an important role on the enhancement of the product concentration. Further study is needed to confirm the effects of mass transfer resistance.

2.6 Conclusions

In this work we ignored the mass transfer resistance for both reaction and adsorption and focused on the effects of reaction kinetics, thermodynamic equilibrium and adsorption isotherm on the performance of the sorption enhanced reaction process. Three model reactions with different stoichiometric parameters, the water gas shift reaction, the H_2S decomposition reaction and the propene metathesis reaction, are studied. It was found from the first two reactions that in order to produce high purity product the following parameters: K_r, K_{eq} and K_c need to be large enough. The equilibrium constant affects the effluent profile in two ways: 1. by changing the equilibrium concentration of the adsorbate it changes the shape of the adsorbate concentration front thus the effluent profile; 2. by changing the reaction rate it changes the shape of the reaction mass transfer zone. In the meantime the reaction rate constant and the adsorption constant affect the reaction and adsorption separately. Also the reaction stoichiometric parameters are equally important as we found out in the study of the H_2S decomposition, in which the product purity is determined by the initial concentration of S_2 in the reactor. In practice it is difficult to periodically regenerate the reactor to the required level to produce high purity hydrogen. Secondary purification process may be needed to obtain high purity hydrogen from the sorption enhanced H_2S decomposition reactor. These conclusions can be applied to the future design of a sorption enhanced reactor with various reaction schemes. The third reaction sheds light

on the importance of mass transfer resistance on the product concentration for a sorption enhance reaction reactor. Further study is needed to quantify the impacts of the mass transfer process during adsorption and the diffusion terms in the mass balance equation.

Experimental Study of High Temperature Pressure Swing Adsorption with Steam Purge for Carbon Capture using Na-Promoted Alumina

3.1 Introduction

In order to mitigate global warming and climate change caused by greenhouse gases, carbon capture and storage (CCS) was proposed. Three different carbon capture pathways including pre-combustion, post-combustion and oxy-combustion are under development to reduce the CO_2 emission from power plants, which accounts for 40% of total CO_2 emission in the United States [4]. For pre-combustion carbon capture high temperature (>400 °C) CO_2 adsorbents can provide high temperature carbon-free fuel for gas turbines thus increasing the efficiency [50]. It can also be used in hybrid reactors like sorption enhanced water gas shift reactors to produce high purity hydrogen [14].

Among different adsorbents Na-promoted alumina and K-promoted hydrotalcite are the mostly studied materials due to their mild regeneration temperature, relatively high working capacity, long-time stability and low cost [51]. While K-promoted hydrotalcite has been studied by many groups [27, 39, 52-54] not much information is known for Na-promoted alumina, especially for its long-term stability and the role of steam on it.

Na-promoted alumina was first mentioned in a patent by Sircar and Golden [55] as one of the candidate sorbents developed by Air Products and Chemicals Inc for pressure swing adsorption (PSA) processes to separate bulk CO_2 from a wet high-temperature gas. Later our group published a series of work on Na-promoted alumina and K-promoted hydrotalcite [16, 17, 30, 39, 56-62]. It was concluded that it shares the same

chemisorption mechanism thus the same isotherm model as that of K-promoted hydrotalcite. A key feature during those studies is that they were performed as a temperature swing adsorption process where adsorbents were regenerated by increasing the column temperature during each test no matter with steam or not. It was concluded that steam acted as inert purge gas during regeneration.

A novel temperature swing sorption enhanced reaction (TSSER) was proposed [30] based on the experimental results obtained, where high pressure and low pressure steam were needed to regenerate the adsorbent. Based on simulation results Na-promoted alumina was found to require less steam during regeneration compared with K-promoted hydrotalcite [61]. A high pressure condenser was studied to recover the high pressure steam used in TSSER, the heat recovery of which was estimated to be 11-32% [62].

Compared with temperature swing adsorption (TSA), pressure swing adsorption (PSA) can be run in faster cycles and requires less heat for regeneration. So far there is no experimental study related to PSA using Na-promoted alumina. Also recent results on other similar alkali metal promoted metal oxides show that steam plays a rather complicated role at various conditions. Walspurger et al. [63] reported K-Dawsonite crystalline phase was found on the potassium promoted alumina using in situ XRD under an equimolar mixture of CO_2 and steam at 10 bar between 200-300 ℃, and the breakthrough capacity was found to be enhanced to 1.5-1.7 mol/kg by adding steam. Boon et al. [53] measured the steam and CO_2 mixture adsorption isotherm experimentally and proposed a combined model with low pressure surface adsorption and high pressure nanopore adsorption parts, where steam and CO_2 only interact through

the high pressure nanopore part. Here we aim to explore the process performance of different PSA cycles and the role of steam as the purge gas on Na-promoted alumina. The testing temperature and CO_2 partial pressure was determined by the exhaust gas out of a gas turbine to be around 400~440 °C and 2 atm.

3.2 Experimental section

Materials: Na-promoted alumina is purchased from BASF (CL-750) originally designed for hydrogen chloride removal.

3.2.1   Thermogravimetric analysis (TGA) tests

TA Instruments SDT Q600 was used for the TGA tests. Nitrogen (Praxair, >99.998%) was used as the purge gas and pre-mixed 44% CO_2 balanced with N_2 and pure CO_2 (Praxair, >99.998%) were used for the adsorption test gas. A typical TGA run was carried out with around 30 mg sample using platinum pans at 1 atm. The gas flow rate was set at 100 mL/min. The sample was first heated at 10 °C/min to the activation temperature (500 °C for Na-promoted alumina) and kept at that temperature for 4 hr in order to dehydrate and desorb CO_2. The adsorption step was started after the sample weight stabilized at the testing temperature. The flowing gas was then switched from the purge gas to the adsorption test gas. During the desorption step the flowing gas was switched back to the purge gas. The influence of switching between different gases is negligible and was confirmed by checking the weight signal change using empty platinum pans. The adsorption capacity was calculated by the amount of CO_2 adsorbed divided by the weight of the dehydrated sample (Eq. (3.1)).

$$n = \frac{W_{ad} - W_{dry}}{M_{CO_2} W_{dry}}$$
(3.1)

where M_{CO2} is the molecular weight of CO_2, W_{dry} is the sample weight when the adsorption step starts and W_{ad} is the sample weight when the adsorption equilibrium is reached. However it is hard to accurately measure the total dry sample weight in a relatively large packed column for the pressure swing adsorption and breakthrough test. In this work the total sample weight during column packing was measured and part of the fresh sample was tested by the TGA test mentioned above. The weight loss based on the TGA test was then used to estimate the dry weight of the sample packed in the column. The sample weight and density in the following analysis are based on the dry weight.

3.2.2 Pressure swing adsorption and column breakthrough tests

A bench scale (Figure 3-1) and a pilot scale (Figure 3-3) experimental setup were built to test different quantities of adsorbents (~15g and ~200g) by pressure swing adsorption and column breakthrough tests. Here for the bench scale setup the following items were used for the experimental test rig: standard 44% CO_2 balanced with N_2 gas mixture (Praxair), argon (>99.999%, Praxair), nitrogen (>99.998%, Praxair), helium (>99.999%, Praxair), mass flow controllers (Alicat Scientific, Tucson, AZ and Aalborg instruments & controls, Orangeburg, NY), mass flow meters (Alicat Scientific, Tucson, AZ), back pressure controllers (Alicat Scientific, Tucson, AZ), and mass spectrometer (Pfeiffer QMA 200, Nashua, NH). The DAQ system (CB-7017, 7018 and 7520) comes from Measurement Computing Corp. and the control and automation system was enabled by a programmable logic controller (PLC), ELC series from Eaton Corp. For the pilot scale experimental setup mass flow controllers for CO_2 and N_2 were from Brooks Instrument due to a higher working pressure requirement. The high pressure

liquid metering pump from Eldex Laboratories Inc. provides accurate liquid flow rate to generate steam. Water separator with a coalescing filter and automatic drain from Parker Hannifin Corp. was used to separate condensed water from gas after the condenser. Desiccant (indicating Drierite from W.A. Hammond Drierite Co. Ltd.) was used before the gas product entered the Mass-Spec. High temperature heating tapes were used for the heating system for the bench scale setup (2-section) and the pilot scale setup (3-section). While the temperature controllers were controlled by K-type thermocouples attached to the wall, three K-type thermocouples were inserted into the column to monitor the temperature change inside the column. The setup pictures are shown in Figure 3-2 and Figure 3-4. The packed bed properties of the bench scale setup and pilot scale setup can be found in Table 3-1. Unlike the bench scale bed, glass beads were mixed and packed together with Na-promoted alumina in the pilot scale bed to reduce the temperature peak caused by heat of adsorption.

A helium expansion experiment (Figure 3-5) was performed at room temperature to obtain the void volume (V_{void}) in the experimental setup using Eq. (3.2), where P_H and P_L are the pressure before and after the test setup is connected with the standard vessel and V_s is the volume of the standard vessel. After the setup was heated up to the test temperature the helium expansion experiment was performed again to calculate the average temperature T_H in the system. By doing the mass balance calculation before and after connecting to the standard vessel at room temperature T_0, the average temperature in the system T_H can be derived by Eq. (3.3).

$$V_{void} = \frac{P_L - P_{atm}}{P_H - P_L} V_s \tag{3.2}$$

$$T_H = T_0 \frac{V_{void}\left(P_H - P_L\right)}{V_s\left(P_L - P_{atom}\right)} \tag{3.3}$$
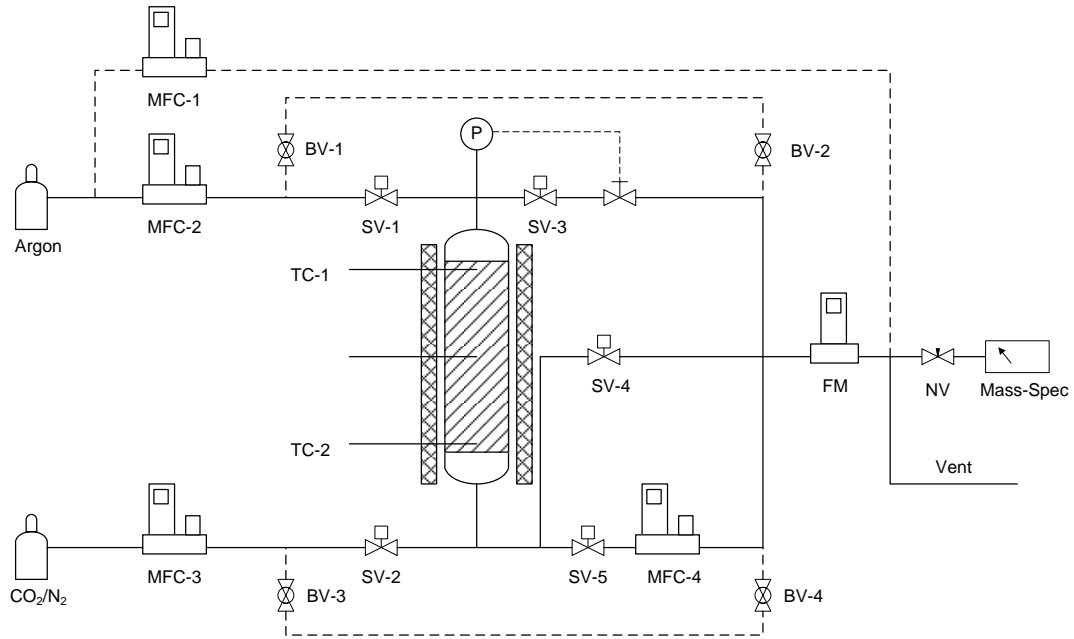
Figure 3-1 Schematic diagram of the bench scale experimental setup version 1.0 for the breakthrough and pressure swing adsorption tests on high temperature CO_2 adsorbents (MFC: mass flow controller, BV: ball valve, TC: thermocouple, P: pressure sensor, SV: solenoid valve, FM: flow meter, NV: needle valve, Mass-Spec: mass spectrometer)
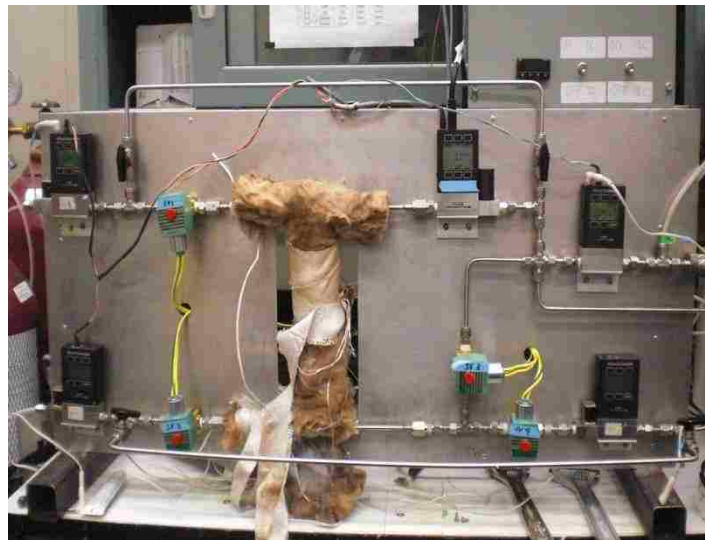
Figure 3-2 Picture of the bench scale experimental setup for high temperature PSA test of CO_2 capture
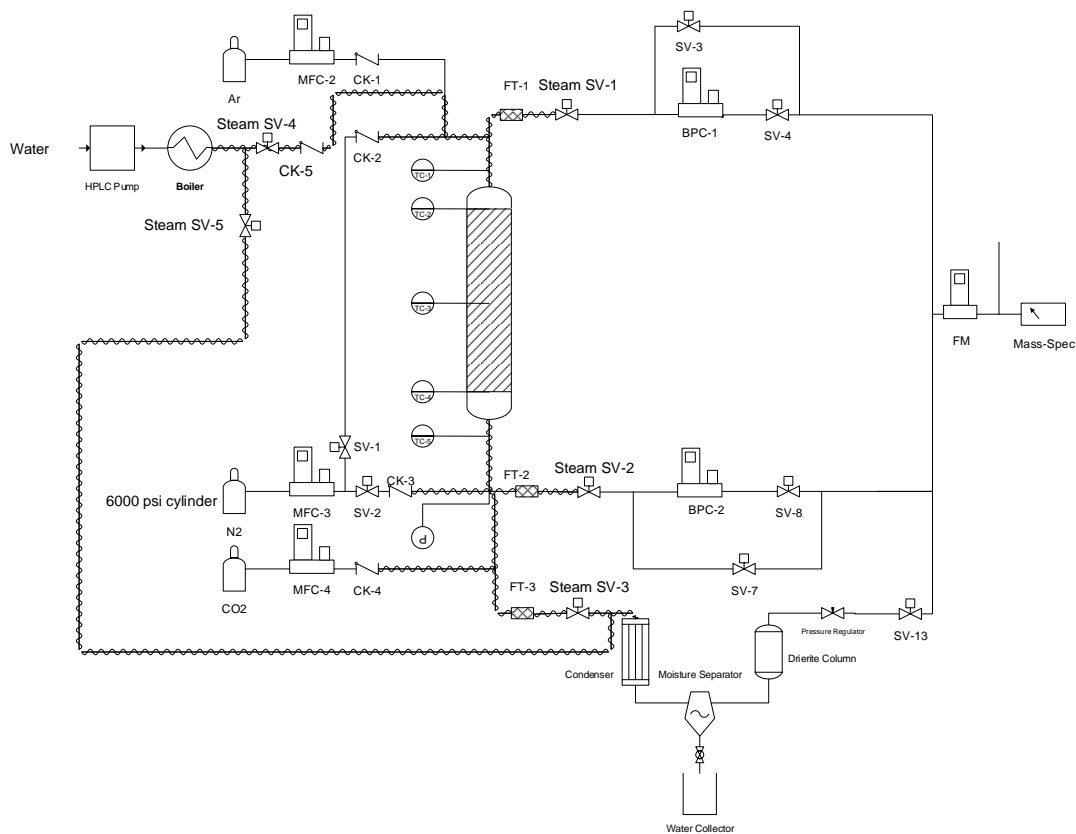
Figure 3-3 Schematic diagram of the pilot scale experimental setup with automated steam procedures for adsorbent regeneration (MFC: mass flow controller, BV: ball valve, CK: check valve, FT: filter, TC: thermocouple, P: pressure transducer, BPC: back pressure controller, SV: solenoid valve, FM: flow meter, Mass-Spec: mass spectrometer)

Figure 3-4 Picture of the pilot scale experimental setup for high temperature PSA test of CO$_2$ capture
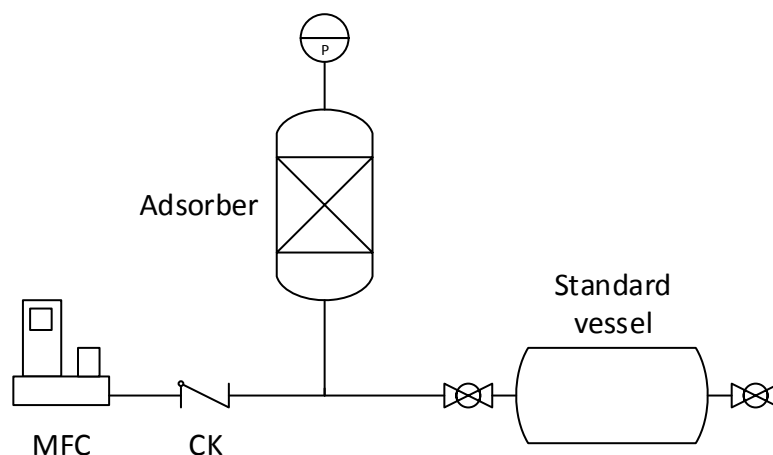
Figure 3-5 Diagram illustration of the helium expansion experiment (MFC: mass flow controller for helium, CK: check valve, P: pressure transducer)

3.2.3   Bench scale tests

Four cases of pressure swing adsorption (PSA) cyclic tests were performed on the bench scale experiment setup. For each case the cyclic steady state was reached judging by the outlet composition and column temperature profile of the last two cycles. The column was fully regenerated at 500 °C before each cyclic test. The PSA cycle schemes are shown in Figure 3-6. The 5-step cycle analysis was based on the experimental results of the 4-step cycle, with the 4th purge step divided into a rinse step and a purge step. The reason to do that is to increase the product purity by purging the residual gas out during the rinse step.

The amount of gas going out of the column was calculated based on the calibrated flow meter reading. The response time for the detector (Mass-Spec) was estimated to be around 8 seconds by comparing the response of the flow meter and the detector during the breakthrough experiment. Since the flow meter reading has a linear relationship with gas viscosity, the flow meter was calibrated by the gas mixture viscosity correlation by Kestin and Ro [64] using the effluent gas composition measured by the Mass-Spec.
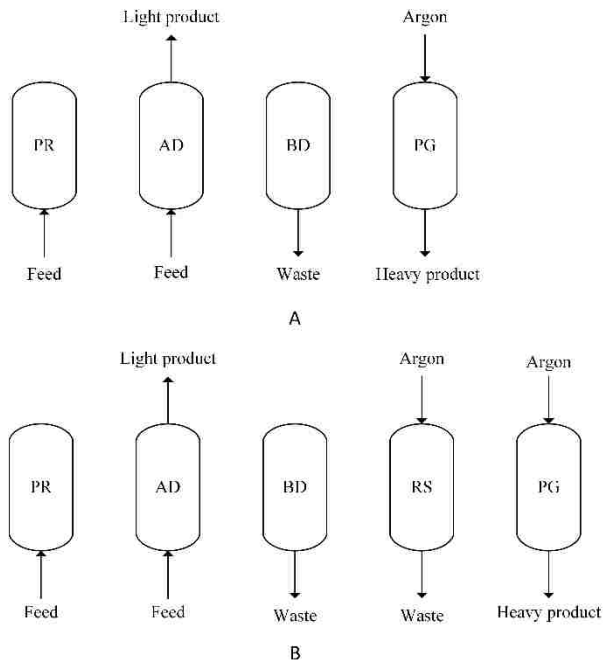
Figure 3-6 4-step-1-bed (A) and 5-step-1-bed (B) pressure swing adsorption cycle for CO_2 capture (PR: pressurization, AD: adsorption, BD: blowdown, RS: rinse and PG: purge)

Table 3-1 Bed properties of the bench scale test and pilot scale test

Bench scale setup bed properties	
ID, cm	1.09
Height, cm	16.5
Bulk density, g/cm^3	0.906
V_{void}, cm^3	61.53
T_H, ^oC	125.2
Pilot scale setup bed properties	
ID, cm	2.21
Height, cm	56.5
Bulk density for Na-promoted alumina, g/cm^3	0.489
Bulk density for glass beads, g/cm^3	0.411
V_{void}, cm^3	314.1
T_H, ^oC	254.1

After the pressure swing adsorption cycle tests were finished, the breakthrough experiment was performed at various CO_2 partial pressures, with adsorption at 400 ^oC and desorption at 500 ^oC. The breakthrough capacity is calculated based on the mass

balance of CO_2 from when the adsorption step starts to when the bed is saturated with the feed, which is typically less than 20 min while the desorption step is usually more than 1 hr. Typical mass balance error over the complete adsorption and desorption cycle is less than 3%, however when comparing the amount of CO_2 adsorbed and desorbed during each cycle the error could be as high as 20% due to the reason of hard-to-measure low level CO_2 composition during desorption. Therefore the breakthrough capacity here is based on the mass balance during the adsorption step shown in Eq (3.4):

$$n = \frac{\int_0^{t_{ad}} \left(F_{CO_2}^{in} - F_{out} y_{CO_2} \right) dt - V_{void} P_{total} y_{CO_2}^{eq} / RT_H}{m_{dry}} \qquad (3.4)$$

where F is the molar flow rate and t_{ad} is the time when adsorption finishes. After the breakthrough tests the used sample were then taken out and tested by TGA tests and compared with the results of the fresh sample.

3.2.4 Pilot scale tests

The pilot scale tests were performed to verify the role of steam during regeneration. Glass beads with diameter (~3mm) similar to that of Na-promoted alumina was mixed with as diluent in the column. The bed density and mixing ratio can be found in Table 3-1. The breakthrough tests done for the pilot scale setup were similar to that done for the bench scale tests. The experimental steps can be found in Figure 3-7. The same equation (Eq. (3.4)) was used to calculate the breakthrough capacity. The only difference lies in the regeneration step. The regeneration temperature was kept the same as the adsorption temperature at 440 °C. The steam test was performed at ambient pressure with 80% steam and 20% nitrogen. Here nitrogen was used to carry all the desorbed CO_2 out of the condenser. A control test called Dry I was done by using the

same amount of gas without steam to regenerate the bed. Because there is no water removal device during the adsorption step, the bed needs to be completely dry before the adsorption step begins. Dry II was performed for both dry and steam tests to remove the moisture in the column. Breakthrough tests at P_{CO2} = 1 atm and 2 atm were performed. Since the tests at P_{CO2} = 1 atm were done at ambient pressure there was no pressurization and depressurization step. A series of breakthrough tests were performed and the results will be discussed later.
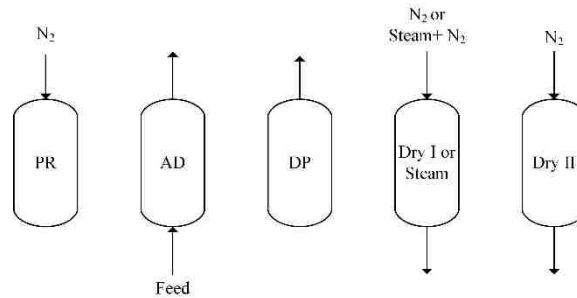
Figure 3-7 Steam test steps for the pilot scale setup when P_{CO2} = 2 atm (PR: pressurization, AD: adsorption, DP: depressurization, Dry I: dry purge, Steam: steam purge, Dry II: dry purge)

The adsorber column temperature is controlled by three separate temperature controllers at 440 °C. The temperature variance during the tests is within 12 °C. For a typical breakthrough test at P_{CO2} = 1 atm, during adsorption 0.5 slpm (standard liter per minute) CO_2 is sent to the bottom of the colum until the flow meter reading plus the temperature inside the column stabilizes, which typically takes 20 min. Then desorption for dry tests is started by sending 2.5 slpm pure N_2 or Ar to the top of the column for 30 min. Then the N_2 or Ar flow rate is decreased to 0.5 slpm, which lasts for another 30 min. For steam tests the first section of the desorption step is replaced by 0.5 slpm pure N_2 or Ar together with around 2 slpm gas phase steam. The second section of the desorption step is the same as before, which will take away residue moisture inside the

column. For a typical breakthrough test at P_{CO2} = 2 atm, there are 2 more additional steps: pressurization and depressurization. The bed is first pressurized with 1 slpm nitrogen and stabilized at 4 bar for 5 min before adsorption starts. During adsorption 0.5 slpm CO_2 and 0.5 slpm N_2 gas mixture is sent from the bottom to the top of the bed. After 20 min when the bed is saturated with gas mixture, co-current blow down starts. The desorption steps are the same as those done at ambient pressure tests.

3.3 Results and discussion

3.3.1 PSA results of the bench scale setup

The adsorption pressure was chosen as 4.54 bar (52 psig) to separate a 44% CO_2 and N_2 mixture. The combination of adsorption pressure and mixture concentration enables us to test the adsorbent performance at 2 bar CO_2 partial pressure. 4-step-1-bed PR+AD+BD+PG and 5-step-1-bed PR+AD+BD+RS+PG PSA cycles are explored here to study the effects of additional rinse step. The first cycle scheme is the simplest cycle scheme similar to the typical Skarstrom cycle. For either cycle scheme three tests were done using the feed to pressurize the bed and one test was, for comparison, done using argon.

3.3.1.1 4-step-1-bed PSA cycles

The test conditions for the four tests are listed in Table 3-2. The flow rate and time are values set in the programmable logic controller (PLC). The detailed mass balance results for each case can be found in the supplemental information. Assuming the gas received during PG is the product, the performance data are summarized in Table 3-3.

Table 3-2 Test conditions for 4-step-1-bed PSA cycles to capture CO_2 from 44% CO_2 and N_2 mixture on Na-promoted alumina at 400 ºC and 4.54 bar (F: flow rate/sccm, T: time/sec)

Case#	Total cycles #	Pressurization (PR) P: 1->4.54bar		Adsorption (AD) P: 4.54bar		Blowdown (BD) P: 4.54->1bar		Purge (PG) P: 1bar	
		F	T	F	T	F	T	F	T
1	79	132	105	132	300	100	92	100	300
2	42	132	105	132	45	200	46	150	400
3	47	132	105	132	25	200	46	150	200
4	43	142	70	132	100	200	60	142	150

Table 3-3 Performance of 4-step-1-bed PSA cycles

	Purity	Recovery	Ar (Steam) / cm^3	Feed throughput cm^3/min	Total feed / cm^3
Case 1	0.67	0.16	517	52	608
Case 2	0.65	0.42	1046	29	285
Case 3	0.64	0.41	521	37	232
Case 4	0.71	0.35	645	36	228

The adsorption time for Case 1 was long enough to saturate the bed with the feed. Hence it provided the highest purity among the cases where the bed was pressurized by the feed. However much CO_2 was wasted in the adsorption step, resulting in the lowest recovery. Taking into account the amount of CO_2 left in the void space, which was around 20 cm^3, the actual amount of CO_2 desorbed during PG, i.e. the working capacity of Na-promoted alumina, was around 0.066 mol/kg in Case 1. Comparison with TGA and breakthrough tested equilibrium capacity was made in Figure 3-9.

In order to increase the working capacity of adsorbents and the CO_2 recovery, the amount of Ar used for PG was doubled and the adsorption time was shortened in Case

2 (Table 3). As a result, the working capacity is estimated to be 0.093 mol/kg and the recovery is increased to 0.42.

To further reduce the amount of CO_2 lost in AD, a shorter AD time was set for Case 3 with the same amount of Ar used during PG as that in Case 1. The purity and recovery are close to that of Case 2 but only half the amount of Ar was used during PG. The working capacity is close to that in Case 1. The purity and recovery of Case 2 and 3 are very close. Although the working capacity in Case 2 is higher, the effects of improved working capacity are diminished by the amount of CO_2 lost during AD and BD.

In all of the 3 cases above the CO_2 concentration front already reached the end of the bed when PR was finished. Therefore part of the adsorption of CO_2 was taken place when the desired partial pressure wasn't reached. To fully utilize the adsorbents' capacity and also create a sharp concentration front [65], Ar was used to pressurize the bed in Case 4. Two thirds of Ar as that in Case 3 was used. A smaller working capacity is observed with a higher purity even compared with Case 1. That can be explained: a larger fraction of Ar taking the place of N_2 in the void space after BD. With a less working capacity more CO_2 is lost during AD thus giving a smaller recovery.

The system void volume is measured by the helium expansion experiment to be 61.5 cm^3 including the bed void volume, the connecting tubing, fittings, etc and the bed volume is 15.5 cm^3. In all the four cases there are two significant drawbacks caused by this large void volume. One is that more than half of CO_2 is lost during BD, the other one is that the product purity during PG decreases with larger void volume due to more N_2 left in the void space after BD.

3.3.1.2 5-step-1-bed PSA cycles

To increase the product purity during PG a rinse step is introduced using Ar to push the interstitial N_2 out. This work is done based on the data obtained with the 4-step-1-bed PSA cycles by manually divide the purge step into a rinse step (RS) and a purge step (PG). RS is stopped when CO_2 concentration is higher than 80%. The corresponding test conditions and performance summary for the four cases are shown in Table 3-4 and Table 3-5.

Table 3-4 Test conditions for 4-step-1-bed PSA cycles to capture CO_2 from 44% CO_2 and N_2 mixture on Na-promoted alumina at 400 ºC and 4.54 bar (flow rate F: sccm, time T: sec)

Case#	Total cycles #	Pressurization (PR) P:1->4.54 bar		Adsorption (AD) P: 4.54 bar		Blowdown (BD) P: 4.54->1 bar		Rinse (RS) P: 1 bar		Purge (PG) P: 1 bar	
		F	T	F	T	F	T	F	T	F	T
1	79	132	105	132	300	100	92	100	33	100	267
2	42	132	105	132	45	200	46	150	31	150	369
3	47	132	105	132	25	200	46	150	29	150	171
4	43	142	70	132	100	200	60	142	25	142	125

Table 3-5 Performance of 5-step-1-bed PSA cycles

	Purity	Recovery	Ar (Steam) / cm^3	Feed throughput cm^3/min	Total feed / cm^3
Case 1	0.86	0.08	517	52	608
Case 2	0.79	0.20	1046	29	285
Case 3	0.82	0.18	521	37	232
Case 4	0.86	0.18	351	36	228

As is shown in Table 3-4 the time taken by the rinse step (RS) is consistent for Case 1 to 3, namely around 30 sec. But the flow rates are different. Case 1 and Case 4 show the highest purity of 86% CO_2 balanced with N_2, which is lower than expected. Because N_2 is considered to be inert and after the remaining interstitial N_2 has been removed from the column, only pure desorbed CO_2 is coming out during the purge step (PG). The product composition during the purge step is shown in Figure 3-8. It shows an asymptotic composition of 2% CO_2 and ~0.6% N_2 regardless of the total purge flow.
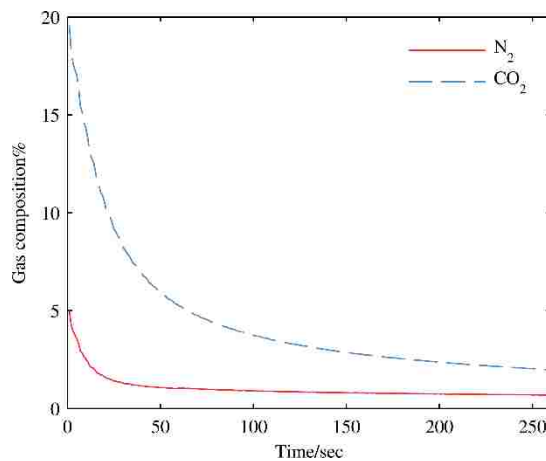
Figure 3-8 CO_2 and N_2 composition detected by Mass-Spec during purge in Case 1 of 5-step-1-bed PSA cycles

By using the 5-step-1-bed PSA cycles the product purity is improved from 67% to 86% (probably higher if Mass-Spec were accurate at low levels). The trade-off is a lower recovery. It is possible that the gases lost during AD, BD and RS can be recovered by the utilization of a multi-bed process. Also a higher capacity adsorbent may increase product purity and reduce the equipment size.

3.3.2 Comparison between breakthrough tests and TGA tests
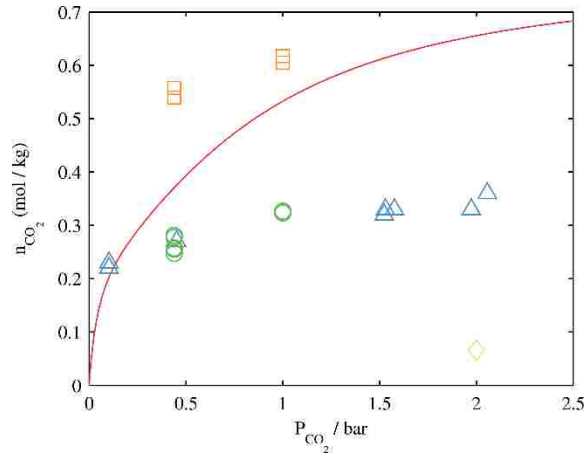
Figure 3-9 Comparison of the used (○) and fresh (□) sample capacity measured by TGA and breakthrough (Δ) tests with the simulated value (line) for Na-promoted alumina at 400 ºC (the estimated cyclic working capacity (◊) is also shown here)

The small working capacity observed in the PSA tests is unexpected. According to the isotherm model reported by Lee et al. [60] ideally (without considering the mass transfer resistance and column dynamics) the working capacity would be 0.65mol/kg. Additional breakthrough tests were done to check the adsorbents equilibrium capacity. The results are shown in Figure 3-9. A huge deviation was observed especially at the higher partial pressure region. According to the newly measured isotherm ideally the working capacity would be around 0.35mol/kg. Still this value is much higher than what was observed in the PSA tests, namely less than 0.1mol/kg, which proves the PSA performance is desorption limited. Desorption tests were carried out at 300, 400 and 500ºC as is shown in Figure 3-10. It was observed that the rate of desorption slows down after around 40 cm^3 CO_2 at all three temperatures. This is very close to what was observed in the PSA tests during the purge step. The fastest desorption rate is found at 500 ºC while the desorption rate at 300 ºC follows exactly as that at 400 ºC. It is not clear which mechanism is dominating during desorption.
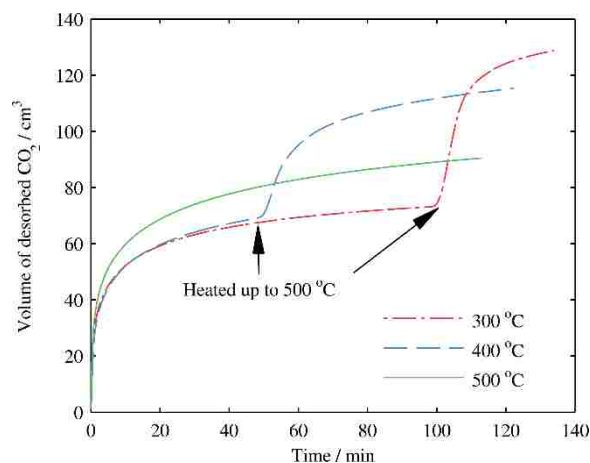
Figure 3-10 Desorption tests of Na-promoted alumina at different temperatures (after breakthrough test of 44% CO₂ and N₂ mixture at corresponding temperatures)

According to Lee et al. [56] completely reversible desorption of CO_2 on Na-promoted alumina was observed at 350 ^{o}C, namely more than 95% of CO_2 desorbed with 90 min of pure N_2 purge, and the desorption process can be described by the linear driving force model using the same mass transfer coefficient as is used in the adsorption process. This is not true with the Na-promoted alumina sample tested in this work. The adsorption and desorption test at 300 ^{o}C in Figure 3-10 shows that even after 2 hr N_2 purge there is still 46% CO_2 left on the adsorbents, which was only driven off when the temperature was raised up to 500 ^{o}C. At the end of the 2 hr purge, the CO_2 concentration has already fallen to 0.2%, which is close to the accuracy limit of our Mass-Spec. This type of phenomenon is also observed for the desorption test at 400 ^{o}C. It is shown in Figure 3-10 that after 2 hr purge at 400 ^{o}C the amount of adsorbed CO_2 remains around 0.1 mol/kg, which is 1/3 of the total capacity.

In order to find out the reason why the equilibrium capacity of Na-promoted alumina was much smaller than the value in the literature and to confirm the capacity data

obtained by the breakthrough method, thermogravimetric analysis (TGA) was applied to Na-promoted alumina. Both used samples from previous column tests and fresh samples were tested. The results are shown in Figure 3-9. The capacity of the fresh samples (square) appears to be slightly above the model predicted data while the capacity of the used samples (circle) falls right around the breakthrough tests results (triangle). Therefore it confirms the previous breakthrough results and reveals the long term degradation of Na-promoted alumina. The desorption of CO_2 on a used sample after being saturated by 44% CO_2/N_2 at 400 ^{o}C is also studied. As shown in Figure 3-11 the weight loss curve is approximately linear during the first 30min. After that the rate of desorption slows down. It indicates that two different mechanisms take place during desorption. The operation of PSA cycles falls into the linear section with a desorption rate of 0.0036 mol/kg/min. If this desorption rate could be applied to the estimated 0.066 mol/kg actual working capacity in Case 1 of 4-step-1-bed PSA cycles, it would have taken 21 min for the desorption to take place while the whole cycle was no more than 14 min. Hence this mechanism cannot be applied directly to the PSA cycles.

Compared with the column desorption test in which 0.146 mol/kg CO_2 desorbed in 50 min in Figure 3-10, the TGA test shows that 0.155 mol/kg CO_2 desorbed within the same time period in Figure 3-11. The closeness of those two numbers reveals that the column desorption rate is limited by the mass transfer or surface desorption in the solid adsorbents.
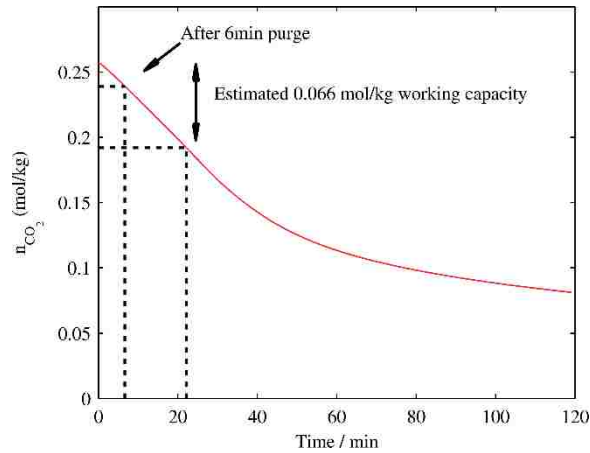
Figure 3-11 Desorption curve of used Na-promoted alumina at 400 ºC measured by TGA

3.3.3 Pilot scale steam tests

3.3.3.1 Comparison between breakthrough tests, TGA tests and model predicted results

The CO_2 capacity of fresh Na-promoted alumina at 440 ºC and $P_{CO2} = 1$ atm measured by TGA are shown in Figure 3-12. Compared with model [60] predicted results the capacity data after 3hr adsorption in TGA appear to be slightly higher. The adsorption kinetics details are shown in Figure 3-13. The equilibrium is not reached until 90 minutes. From the inset in Figure 3-13 it is shown that the rate of adsorption slows down after the first ~5 minutes, which is when the adsorption capacity becomes close to what is predicted by the model.

Previous study by our group shows that the CO_2 equilibrium capacity at 440 ºC follows the pattern in Figure 3-12. At 1 and 2 atm the equilibrium capacity is 0.45 and 0.6 respectively. Compared with the breakthrough tests results shown in Figure 3-14 the initial test at ambient pressure is very close the model results. During the breakthrough tests the bed was never fully regenerated, which is the reason the capacity is lower thereafter. The breakthrough capacity at $P_{CO2} = 2$ atm reached the maximum after the bed was regenerated by steam. However compared to the model result 0.6 mol/kg it is

72

still lower. Also as is reflected by the results in Figure 3-14 there are lots of uncertainties in the measure at this condition due to errors from the detector and flow meters.
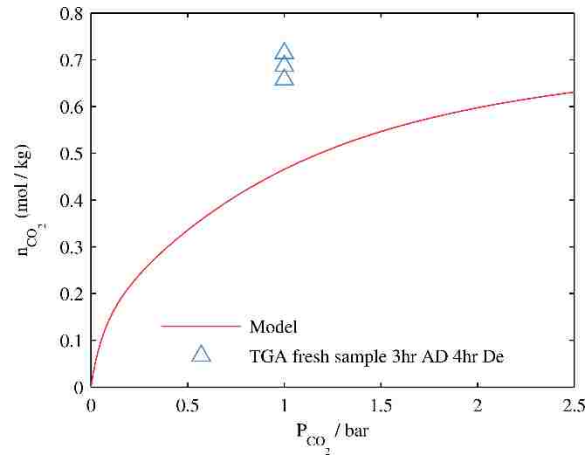
Figure 3-12 Comparison of the isotherm model by Lee et al. [60] and TGA test results on Na-promoted alumina at 440 ºC
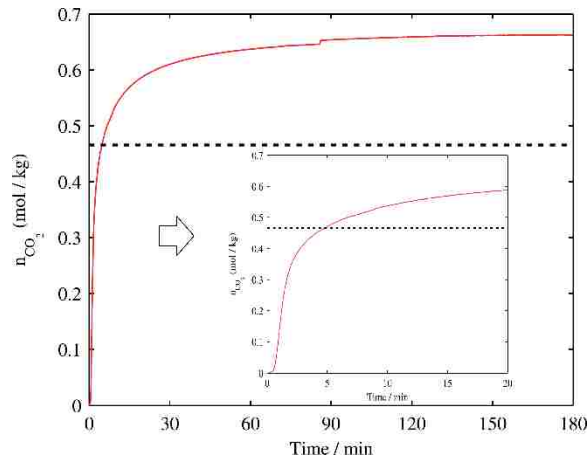
Figure 3-13 TGA capacity test on fresh Na-promoted alumina at 440 ºC when P_{CO2} = 1 atm (dashed line is the capacity predicted by the isotherm model, the inset is a zoom-in for the first 20 minutes)
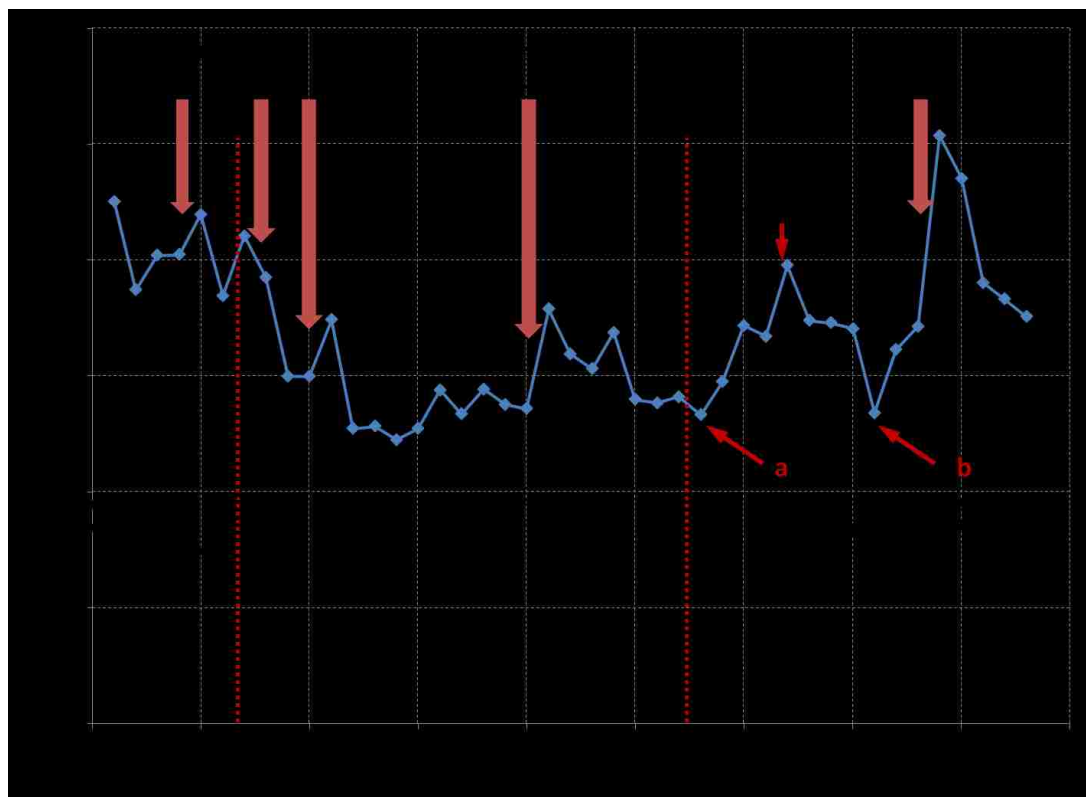
Figure 3-14 Breakthrough tests on Na-promoted alumina at 440 ºC and ambient and high pressure (P_{CO_2} = 2 atm)

For the first 6 tests the test conditions were explored to enable a full breakthrough and reasonable regeneration. From the 7th test on every test was done at the same conditions. The adsorber bed is only partially regenerated so that the capacity measurement is in fact the working capacity of alumina at these cyclic testing conditions. As shown in Figure 3-14 it reached cyclic steady state around test 12-20. After steam test 4 the capacity of the breakthrough test 21 is increased by more than 0.5 mol/kg. After that 6 dry tests were performed and the capacity slowly deceased to the same level before the steam test. Generally the CO_2 capacity of Na-promoted alumina is increased by around 0.5 mol/kg after steam purge for most cases. There is one exception. During steam test 2 it was observed that the increase of capacity happened before the steam test. It was

later found out the steam leak into the column from a bypass line was the reason. As shown in Figure 3-15 and Figure 3-16 the increased working capacity of the adsorbent can be clearly indicated by the delay of flow meter readings and mass spectrometer response curves.

The high pressure breakthrough test started from *test a*, before which the bed stood still for 4 days after previously being cleaned by the cyclic operation for ambient pressure breakthrough tests. After 4 cyclic high pressure breakthrough tests its capacity stabilized around 0.35 mol/kg. Then the bed was regenerated at 490 °C under dry condition. After 3 cyclic breakthrough tests the working capacity stabilized again at 0.35 mol/kg. After standing still for 4 days the bed was tested by cyclic breakthrough tests again (*test b*). Both *test a* and *b* showed lower capacity compared with the other tests at the same condition, the reason of which is not clear yet. The working capacity before steam test 5 was around 0.35 mol/kg. After steam test 5 the working capacity increased to 0.5 mol/kg and gradually dropped back to 0.35 mol/kg after 4 dry tests.
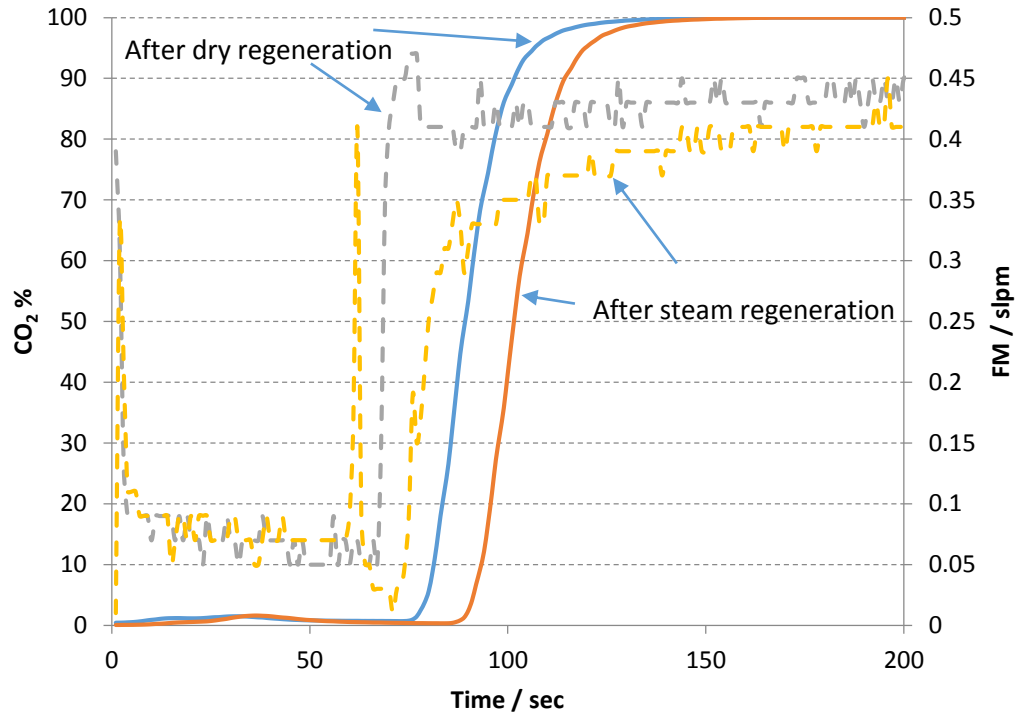
Figure 3-15 Comparison between the breakthrough curve before and after steam test 4 (solid line: Mass-Spec reading of CO_2 composition, dashed line: exit gas flow meter reading)
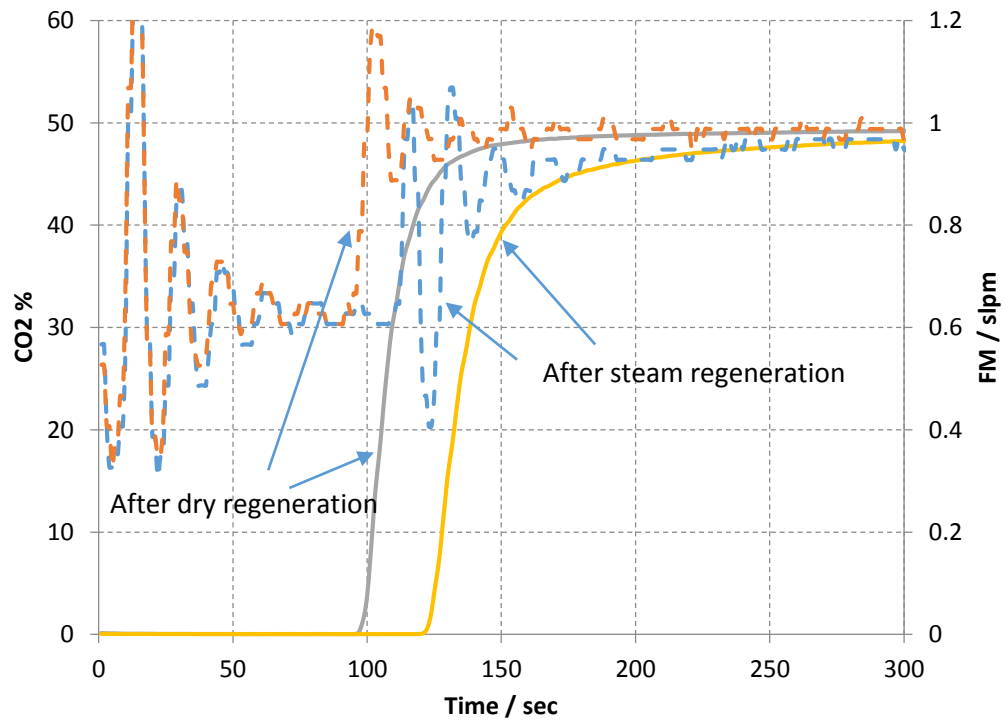
Figure 3-16 Comparison between the breakthrough curve before and after steam test 5 (solid line: Mass-Spec reading of CO_2 composition, dashed line: exit gas flow meter reading)

Table 3-6 Steam mass balance during five steam tests

Steam test #	Water pumped in/g	Water collected /g	Error%
1	85.9	94.1	-9.5
2	44.3	58.5	-32.0
3	37.5	N/A	
4	44.8	43.7	2.4
5	58.2	55.7	4.3

Steam mass balance was performed by measuring the weight loss from the water bottle (source) and the water collected at the moisture separator (destination). The steam test 1 and 2 in Table 3-6 show that more water was collected than what was pumped in. This is due to the water accumulated in the moisture separator when steam was sent through the bypass before the steam purge. This step was skipped since steam test 3. However some water was spilled during steam test 3 so it was not clear the amount of water collected for steam test 3. In the end the results of steam test 4 and 5 show that the steam balance can be closed by that modification of test procedures.

3.3.3.2 Possible role of steam during regeneration
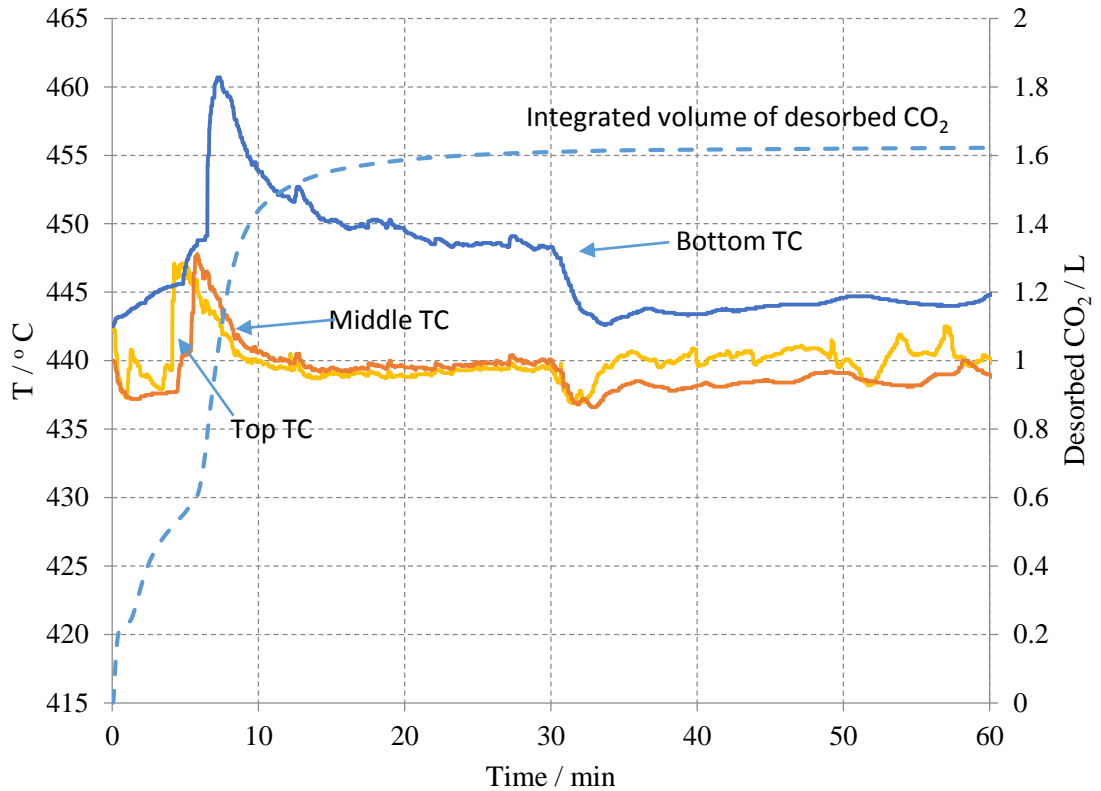
Figure 3-17 Temperatures along the axis of the bed and amount of desorbed CO₂ recorded during Steam Test 4 (Solid line: thermocouple (TC) readings, dashed line: integrated volume of CO₂ coming out of the column)

Figure 3-17 and Figure 3-18 show that the temperature inside the column increased when steam ran from the top to the bottom. The thermocouples along the column axis experienced this temperature pulse in a sequential way. The highest temperature peak was observed at the bottom thermocouple. Compared with the dry test shown in Figure 3-19 the bottom was also 7 °C higher than the other parts of the column. It could be explained by the following reason. The top of the column was cooled by large amount of gas flow while the preheating section was not providing enough power to heat the entering gas from room temperature to 440 °C. Since the sensor for the temperature controllers was located near the region where the flowing gas temperature was lower

than 440 ºC, the heating tape maximized its output to reach the set point. Although the resulting temperature at the sensor was well maintained at the set point, the gas flow was overheated by the heating tape below the sensor. By the time it reaching the column bottom, its temperature was higher than 440 ºC. Therefore, the bottom temperature could not be well-controlled and was overheated.
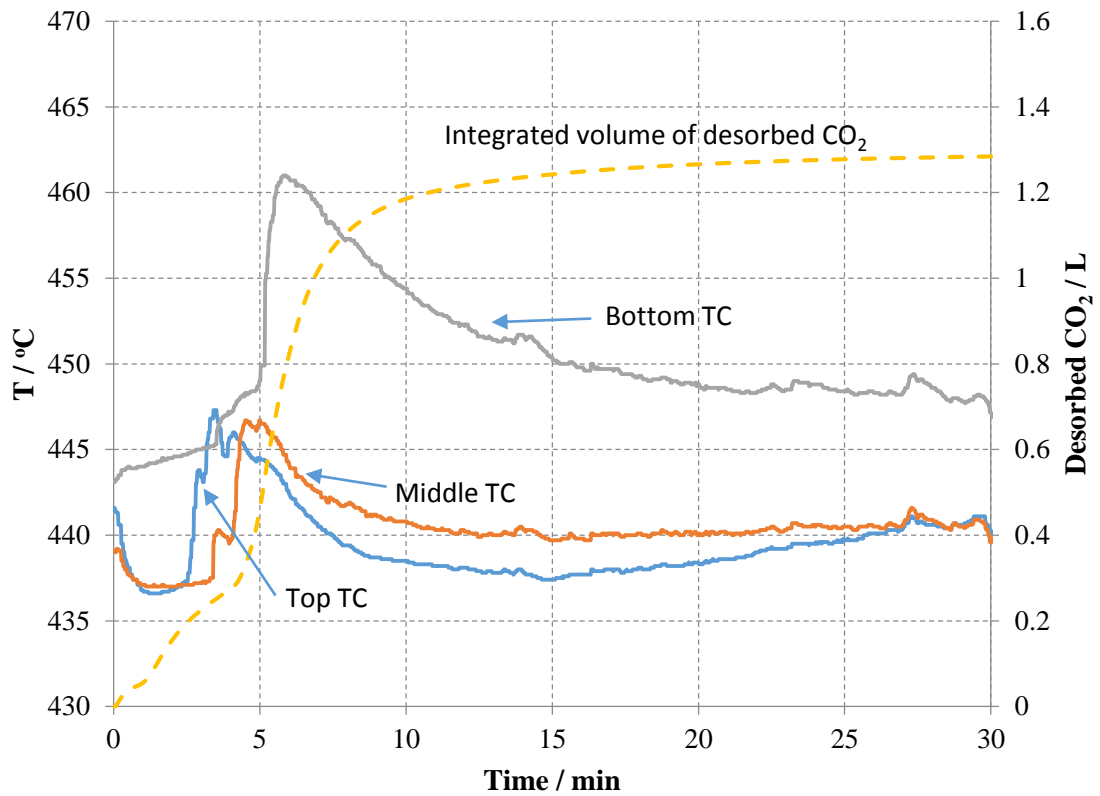
Figure 3-18 Temperatures along the axis of the bed and amount of desorbed CO₂ recorded during Steam Test 5 (Solid line: thermocouple (TC) readings, dashed line: integrated volume of CO₂ coming out of the column)

The temperature peak indicates that steam is not as inert as nitrogen or argon on Na-promoted alumina. Comparing the amount of desorbed CO_2 with respect to time in Figure 3-17 and Figure 3-18 it shows that most of the CO_2 desorbed when the temperature peak appeared around the bottom thermocouple in around 10 min. During

the dry test in Figure 3-19 CO_2 was being continuously removed during the first 30 min. Not only more CO_2 came out during the steam purge but also the rate of desorption was faster.

The direct reason for the benefits of using steam is not clear. To explain the increased working capacity one can look at it from two different angles. One way of viewing it is that the steam purge allows more CO_2 to be released. The other one is that after steam purge additional sites are created. To determine which one is the dominating factor for the higher capacity, the amount of CO_2 adsorbed and desorbed during steam purge tests and dry tests are compared as shown in Figure 3-20. Without steam purge the CO_2 capacity dropped over cycles because some of the adsorbed CO_2 accumulated on the adsorbent as the amount of CO_2 purged out during the desorption step was constantly lower than the amount of CO_2 adsorbed during the adsorption step. Moreover it is found out that the amount of CO_2 purged by steam matches reasonable well with the increased capacity after Steam Test 5. Regeneration by steam helped release of those irreversibly adsorbed CO_2 therefore creating more adsorption sites.

However the heat of adsorption released by steam causes a higher temperature inside the column. The higher temperature could also have facilitated the desorption kinetics and provided a cleaner adsorber. Based on our test with high pressure breakthrough test this could not be the only reason. As shown in Figure 3-14 the adsorber capacity is higher (0.5 mol/kg) after steam purge than that (0.4 mol/kg) after being generated at 490 °C. It could be that steam is competing with CO_2 on the surface of Na-promoted alumina so that CO_2 was pushed out by steam. Once the column is saturated with steam there would be no CO_2 leaving the column as shown in Figure 3-17 and Figure 3-18. Hence

the following conclusions can be reached: steam is competing with CO_2 for the same site on Na-promoted alumina.
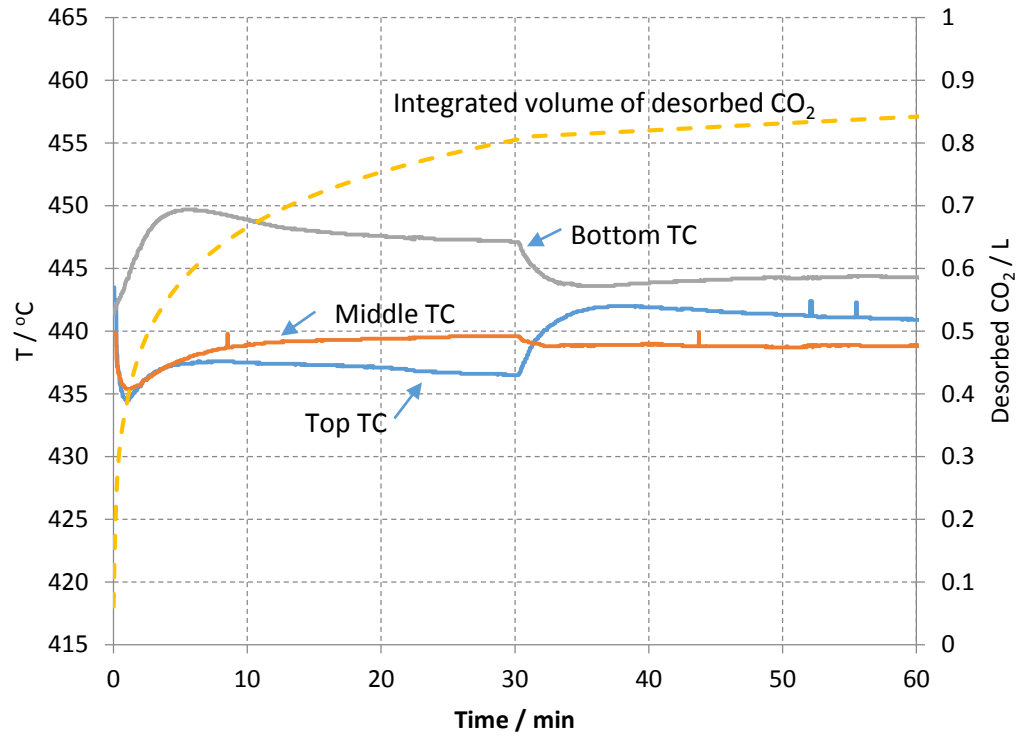
Figure 3-19 Temperatures along the axis of the bed and amount of desorbed CO_2 recorded during Dry Test 20 (Solid line: thermocouple (TC) readings, dashed line: integrated volume of CO_2 coming out of the column)
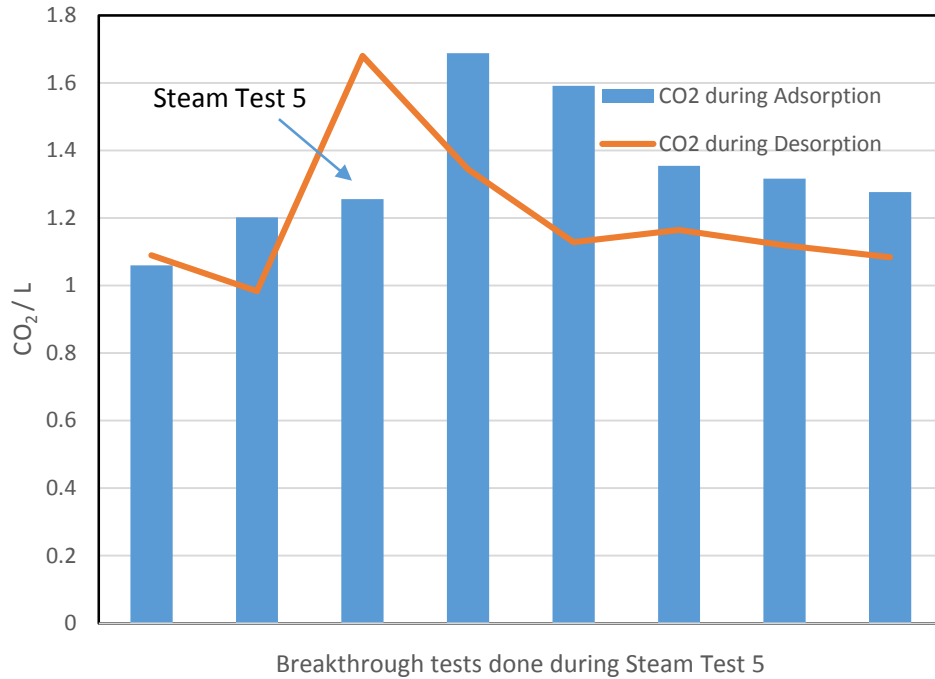
Figure 3-20 Comparison of the amount of CO_2 accumulated during the adsorption steps and purged out during the desorption steps of a series of breakthrough test for Steam Test 5

Although now it is clear that steam is adsorbed on Na-promoted alumina, it is difficult to quantify the amount of steam adsorbed at different conditions. The key issue is to find valves and instruments compatible with steam, which are less common for small scale test setups. So far the only quantitative study of high temperature steam adsorption isotherm was done by Boon et al. [53] on K-promoted hydrotalcite at 400 °C with columns 6 m tall and 3.8 cm ID. According to their results the steam adsorption capacity on K-promoted hydrotalcite is around 0.1 mol/kg at 400 °C and 1 atm. There is an easier way (Eq (3.5)) to estimate the adsorption capacity by monitoring the velocity of the travelling thermal front in the bed when adsorption happens. A few assumptions need to be made here: isothermal bed, sharp concentration front and the ideal gas law. In Eq (3.5) t is the time needed for the thermal front to travel from the top to the bottom thermocouple (TC) shown in Figure 3-21, L is the distance between the top and bottom

TC shown in Figure 3-22 and S is the cross section area of the bed. Capacity calculated based on this method tend to be smaller than the actual capacity. For example it is calculated that CO_2 capacity at 440 °C and $P_{CO2} = 2$ bar is 0.26 mol/kg while according to our mass balance calculation it is around 0.35 mol/kg.

$$F_{H_2O}t = \rho_b LSn_{H_2O} + \frac{P_{Total}\varepsilon LSy_{H_2O}}{RT_{bed}} \tag{3.5}$$

It is estimated that Na-promoted alumina has a capacity of 2.67 mol/kg for steam at 1 atm and 440 °C, which is much higher than that of K-promoted hydrotalcite reported by Boon et al. [53].
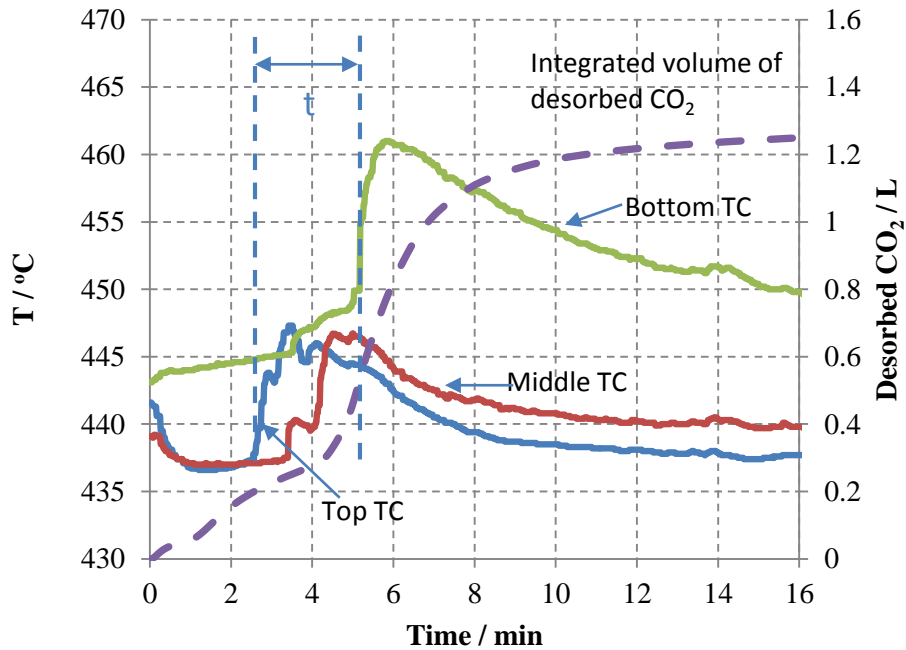
Figure 3-21 Temperatures along the axis of the bed and amount of desorbed CO₂ recorded during Steam Test 5 (Solid line: thermocouple (TC) readings, dashed line: integrated volume of CO₂ coming out of the column, t: travelling time for the thermal wave to move from the top TC to the bottom TC)
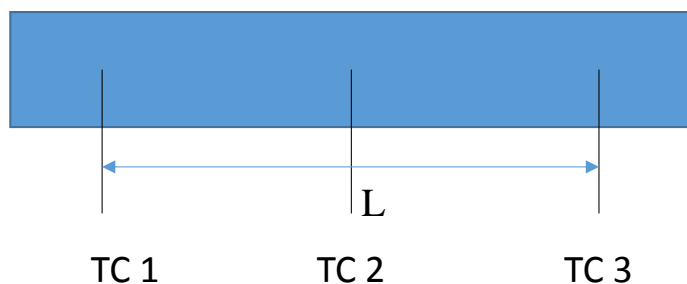
Figure 3-22 Illustration of the column structure

3.4 Conclusions

Our test results on Na-promoted alumina indicate that under dry testing conditions the CO_2 capacity decreases over cycles due to incomplete desorption or irreversible adsorption. However, it was discovered that steam competitively adsorbed on Na-promoted alumina, which makes it ideal for the regeneration of this adsorbent. Further study is needed to quantify the interaction between steam and CO_2 on the surface of Na-promoted alumina. Experimental work to measure the isotherm of pure steam and mixture of steam and CO_2 at various pressures is essential for the design of a novel high temperature pressure swing adsorption process.

3.5 Supplemental information

Table 3-7 Case 1: Mass balance data for each component during one cycle after cyclic steady state is reached for 4-step-1-bed PSA cycles (*volume at standard conditions: 25 ºC, 14.696 psia **CO$_2$% without considering Ar)

Unit: cm^3*	CO$_2$ in	CO$_2$ out	N$_2$ in	N$_2$ out	Ar in	Ar out	CO$_2$ % **
PR	75	1	93	0	181	177	0
AD	197	160	243	233	0	31	41
BD	0	65	0	77	0	12	46
PG	0	43	0	22	517	475	67
Total	272	268	336	332	698	695	45

Table 3-8 Case 2: Mass balance data for each component during one cycle after cyclic steady state is reached for 4-step-1-bed PSA cycles (*volume at standard conditions: 25 ºC, 14.696 psia **CO$_2$% without considering Ar)

Unit: cm^3*	CO$_2$ in	CO$_2$ out	N$_2$ in	N$_2$ out	Ar in	Ar out	CO$_2$ % **
PR	81	0	102	1	180	178	0
AD	45	15	57	53	0	29	22
BD	0	58	0	76	0	13	43
PG	0	52	0	29	1046	977	65
Total	126	126	159	158	1226	1197	44

Table 3-9 Case 3: Mass balance data for each component during one cycle after cyclic steady state is reached for 4-step-1-bed PSA cycles (*volume at standard conditions: 25 ºC, 14.696 psia **CO$_2$% without considering Ar)

Unit: cm^3*	CO$_2$ in	CO$_2$ out	N$_2$ in	N$_2$ out	Ar in	Ar out	CO$_2$ % **
PR	79	1	101	1	183	181	0
AD	23	4	29	23	0	21	14
BD	0	56	0	84	0	15	40
PG	0	42	0	23	521	483	64
Total	102	102	130	131	704	699	44

Table 3-10 Case 4: Mass balance data for each component during one cycle after cyclic steady state is reached for 4-step-1-bed PSA cycles (*volume at standard conditions: 25 ºC, 14.696 psia **CO_2% without considering Ar)

Unit: cm^3*	CO_2 in	CO_2 out	N_2 in	N_2 out	Ar in	Ar out	CO_2 % **
PR	0	1	0	1	288	119	0
AD	98	13	121	47	6	121	21
BD	3	52	4	60	0	75	46
PG	1	34	1	14	351	340	71
Total	102	99	126	122	645	655	45

Table 3-11 Test conditions for the steam tests when P_{CO2} = 1 atm for adsorption

Adsorption		
(Co-current)	CO_2 flow rate, slpm	0.5
	Total pressure, atm	1.0
	Step time, min	20
Regeneration		
Step 1 Dry purge I	N_2 flow rate, slpm	2.5
(Counter-current)	Total pressure, atm	1.0
	Step time, min	30
Step 1 Steam purge	Steam flow rate, slpm	2.0
(Counter-current)	N_2 flow rate, slpm	0.5
	Total pressure, atm	1.0
Step 2 Dry purge II	N_2 flow rate, slpm	0.5
	Total pressure, atm	1.0
	Step time, min	30

Table 3-12 Test conditions for the steam tests when P_{CO2} = 2 atm for adsorption

Adsorption		
(Co-current)	CO_2 flow rate, slpm	0.5
	N_2 flow rate, slpm	0.5
	Total pressure, atm	4.0
	Step time, min	20
Regeneration		
Step 1 Depressurization (Co-current)	Total pressure	4.0 -> 1.0 atm
Step 2 Dry purge I (Counter-current)	N_2 flow rate, slpm	2.5
	Total pressure, atm	1.0
	Step time, min	30
Step 2 Steam purge	Steam flow rate, slpm	2.0

(Counter-current)		
	N$_2$ flow rate, slpm	0.5
	Total pressure, atm	1.0
	Step time, min	30
Step 3 Dry purge II (Counter-current)	N$_2$ flow rate, slpm	0.5
	Total pressure, atm	1.0
	Step time, min	30
Step 4 Pressurization (Co-current)	N$_2$ flow rate, slpm	1.0

Analysis of Pumped Heat Electricity Storage

Process using Exponential Matrix Solutions

4.1 Introduction

The need to store excessive amount of electrical energy comes with the fact that the demand has peaks and valleys while the output of a power plant, especially nuclear power plants, is relatively stable. Additionally development of intermittent renewable energy like wind, solar and tides further provides an incentive for the development of such processes. It is also reported [66] that electricity storage has many benefits ranging from renewable energy integration to power quality and reliability. The most commonly used processes for large scale electrical energy storage (EES) are pumped hydroelectric storage (PHS), compressed air energy storage (CAES) and flow batteries [67].

PHS is comprised of two water reservoirs at different elevations and electrical energy is stored as gravity potential energy. CAES compresses air into large caverns up to 10 MPa and uses gas turbines to recover the energy. Flow batteries have two half-cell electrolyte reservoirs, from which electroactive species flow through a power cell to reversibly convert chemical energy into electricity or vice versa. All three of them have a high turn-around efficiency of 60-90% [68], which is defined as the ratio between the amount of electricity retrieved and the amount of electricity stored. Among the nonchemical techniques PHS and CAES require particular geological structures, which might not be available to regions that EES is needed.

Thermal energy storage could provide a nonchemical solution for regions without any geographical features like rivers and caverns. However as is said by Morandin et al. [69] there is little literature available on the transformation of electrical energy into thermal

energy for storage, because electrical energy is believed to degrade once it is converted to heat. It is mentioned by Chen et al. [68] that the turn-around efficiency for thermal energy storage is usually below 60%. A new thermal electrical energy storage process, referred as pumped heat electricity storage (PHES) in [70], thermo-electrical energy storage (TEES) in [69, 71, 72] or pumped thermal electricity storage (PTES) in [73-75], has recently been proposed and studied by several independent groups [70-74, 76-84]. In this study it will be referred as pumped heat electricity storage (PHES).

4.1.1 Recent development on PHES processes

PHES is able to achieve high turn-around efficiency by acting as a heat pump during loading and as a thermal engine during delivery. In an ideal case where a reversible Carnot heat pump with efficiency of $\eta_1=T_1/(T_1-T_0)$ and a reversible Carnot heat engine with efficiency of $\eta_2=(T_1-T_0)/T_1$ are applied, and pressure drop, thermal losses and properties dependence on temperature are neglected, it could have a turn-round efficiency of $\eta_1 \eta_2=100\%$. A simple finite-time thermodynamics study has been done recently by Thess [70] predicting that the turn-around efficiency of PHES would be comparable to that of advanced-adiabatic CAES under certain conditions.

However the concept is not new and dates back to the work published in 1924 by Marguerre [85], which has not been translated into English. The development of such a concept over the last century is well illustrated in the work by Mercangöz et al. [86]. Recently two types of PHES based on the same basic principle appeared in literature: one is based on using transcritical CO_2 as the working fluid with hot water and ice storage (patented by ABB Ltd. [83]), the other one is based on using inert gas as the working fluid with hot and cold solid material storage tanks (patented by Isentropic Ltd.

89

[87] and SAIPEM S.A. [88]). Although both of them are still under development and no demonstration plants have been built, an increasing number of journal papers and patents shows that this is an area gaining lots of interest.

Full scale process modeling and optimization studies exist for both types of PHES. Morandin et al. [69, 71] optimized the procedure for the synthesis of the heat exchanger network and the storage tanks for the transcritical CO_2 PHES, and achieved a maximum turn-around efficiency of 60% with the isentropic efficiency of compressors and expanders around 0.85. McTigue et al. [75] studied the second type of PHES and concluded that the success of PHES would hinge upon compressor and expander performance and with polytropic efficiency of 0.99 the turn-around efficiency could be close to 70%. The prototype machines development is reported by Howes [80] that 2 prototypes machines were developed at Isentropic Ltd with reciprocating compressors and expanders and based on that preliminary tests a hypothetical 2-MW storage machine is defined with a turn-around efficiency of 72%.

In this work we will focus on the study of the second type PHES with the same configurations as described by Desrues et al. [79]. Our model is based on the cyclic steady state solution obtained by Carnish and Caram [89] for heat regenerators. Traditional full scale simulation of the cyclic heat regenerator operation requires calculation from the initial state and progressively reaches the cyclic steady state. With the help of the exponential matrix solution we are able to express the cyclic steady state solution of the temperature distribution explicitly thus provide an efficient alternative method to evaluate the process. A disadvantage of such a solution is that it cannot be applied to cases where parameters are dependent on temperature, which prevents it from

being used for more detailed engineering simulation. To our best knowledge this method has not been applied to the PHES process, our aim is to provide a different approach to evaluate the second type PHES process and a guideline for further development.

4.2 Process description

The process includes a high pressure (HP) tank and a low pressure (LP) tank packed with solid refractory material, pairs of compressors and turbines to transfer electrical energy into thermal energy and vice versa, a heater and a cooler to regulate the process gas temperature, and a circulating inert gas flow connecting the components listed above. The operation schedule can be divided into two steps: the loading step and the delivery step. Electrical energy is stored as sensible heat in the solid material inside the tank during the loading step and released during the delivery step. The process flow diagrams are shown in Figure 4-1 and Figure 4-3 while the corresponding T-S diagrams are shown in Figure 4-2 and Figure 4-4.
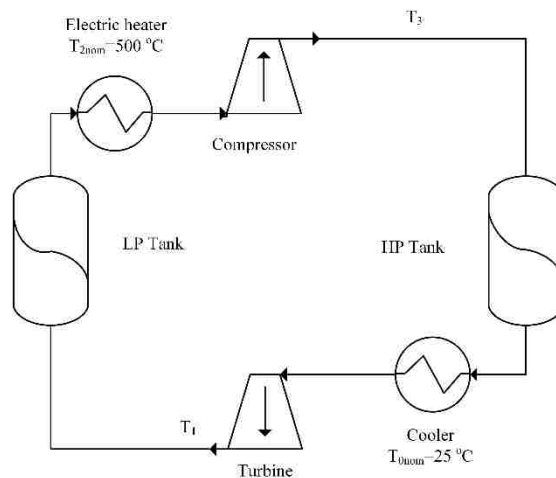
Figure 4-1 Process flow diagram during the loading step
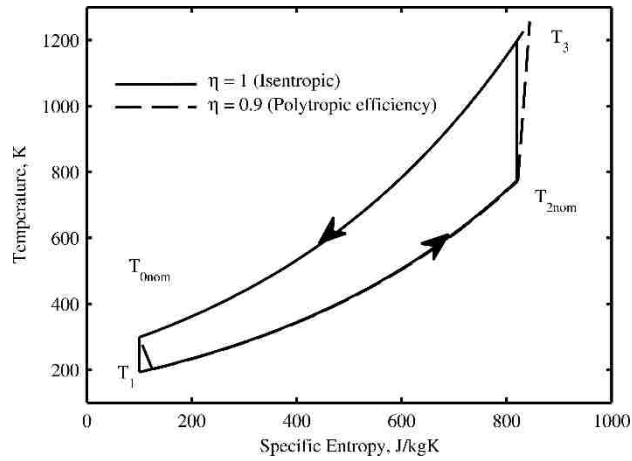
Figure 4-2 T-S diagram during the loading step, comparison with the isentropic turbomachines
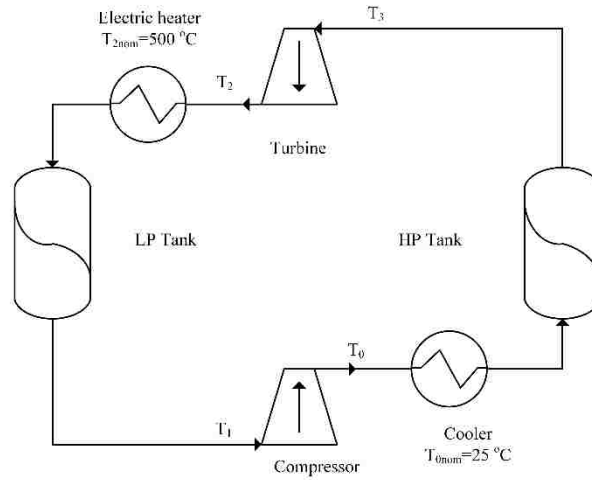
Figure 4-3 Process flow diagram during the delivery step
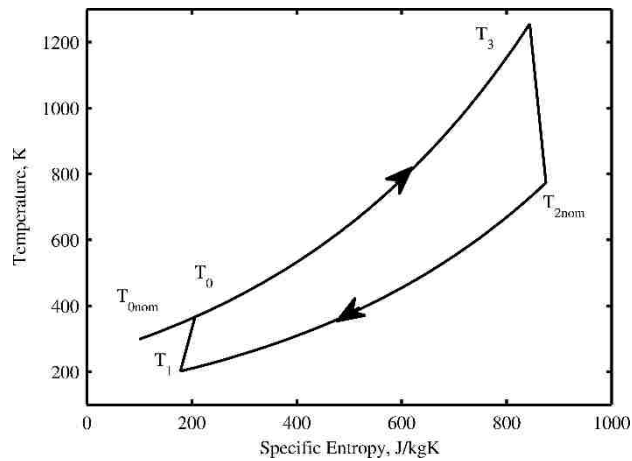
Figure 4-4 T-S diagram during the delivery step

Table 4-1 Illustrative example of the temperature calculation at the compressor and turbine

Loading	Delivery
$T_{2nom} = 773.15$ K, $T_{0nom} = 298.15$ K, PR = 3, $\gamma = 1.66$, $\zeta = 0.9$	$T_{2nom} = 773.15$ K, $T_{0nom} = 298.15$ K, PR' = 3.88, $\gamma = 1.66$, $\zeta = 0.9$
$T_3 = T_{2nom}\psi^{1/\zeta} = T_{2nom}PR^{(\gamma-1)/(\gamma\zeta)} = 1256.1$ K	$T_2 = T_3\psi^{-\zeta} = T_3PR'^{(\gamma-1)(-\zeta)/\gamma} = 773.2$ K
$T_1 = T_{0nom}\psi^{-\zeta} = T_{0nom}PR^{(\gamma-1)(-\zeta)/\gamma} = 201.2$ K	$T_0 = T_1\psi^{1/\zeta} = T_1PR'^{(\gamma-1)/(\gamma\zeta)} = 366.2$ K

During the loading step the gas flows clockwise. The compressor works as a heat pump and raise the gas temperature to a desired point to heat up the HP tank while the expander provides a cold stream to cool the LP tank down. Hence the hot thermal wave moves towards the bottom of the HP tank while the cold thermal wave moves towards the top of the LP tank. The step is stopped before either thermal wave breaks through, otherwise it will become a great burden for the heater and the cooler and decrease the overall energy efficiency.

During the delivery step the gas flows counterclockwise. The expander works as a heat engine to release the thermal energy previously stored in the system. The thermal waves move upward in the opposite direction compared to that of the loading step. The LP tank is heated up while the HP tank is cooled down. The low temperature of the gas stream coming out of the bottom of the LP tank actually reduces the work needed at the compressor.

A cooler is added to remove the extra heat generated by the irreversibilities of the turbomachines at room temperature T_{0nom}. A heater is added to maintain the temperature of the gas going into the compressor at T_{2nom} during the loading step thus increase the total energy stored in the HP tank. Depending on the electricity supply and demand the loading step time and the delivery step time may vary.

4.3 Model description

An exponential matrix solution for the temperature distribution in the storage vessels can be obtained using the method proposed by Carnish and Caram [89]. The tank is discretized into N identical compartments as shown in Figure 4-5. Here a linear relationship of heat transfer between gas and solid phase is applied in Eq. (4.2), in which the heat transfer coefficient (h) is a lumped factor, accounting for the gas phase dispersion effect, the film heat resistance and the heat conduction inside the solid spheres. When h is infinitely large the thermal wave becomes a flat front as is described in Levenspiel's work [90]. Neglecting accumulation of the gas phase, the energy balance equations of the nth compartment for gas and solid phases are given by:
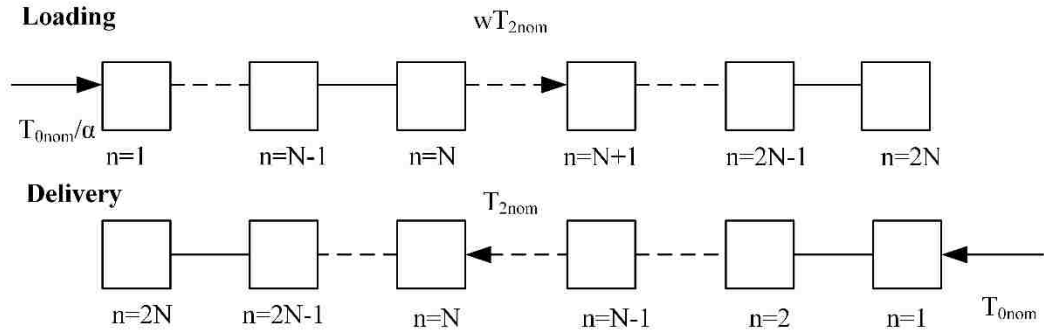
Figure 4-5 Discretized compartments-in-series model for PHES processes

$$\rho_g U_g C_{pg}(\theta_{n-1} - \theta_n) = hal(\theta_n - T_n) \tag{4.1}$$

$$\rho_s C_{ps}\frac{dT_n}{dt} = ha(\theta_n - T_n) \tag{4.2}$$

where U_g, ρ_g, $C_{p,g}$, ρ_s, $C_{p,s}$, h, a, l, T and θ are the superficial velocity, gas density, gas heat capacity, solid bulk density, solid heat capacity, heat transfer coefficient, solid surface area to volume ratio, length of each compartment, solid temperature and gas temperature. We assume $C_{p,g}$, $C_{p,s}$, ρ_s, $\rho_g U_g$ and h are independent of temperature. Process gas is assumed to obey the ideal gas law and irreversibilities of the

turbomachines are taken into account by using the polytropic efficiency ζ. Therefore the temperature ratio for a compressor can be calculated as:

$$w = T_{out} / T_{in} = \psi^{1/\zeta} \tag{4.3}$$

ψ is the thermal compression ratio and for an ideal gas $\psi = PR^{(\gamma-1)/\gamma}$ where $\gamma = C_p/C_v$.

The temperature ratio for a gas turbine can be calculated as:

$$\alpha = T_{in} / T_{out} = \psi^{\zeta} \tag{4.4}$$

As is mentioned in Desrues et al.'s work [79] the irreversibility of turbomachines tends to increase the outlet temperature. In the PHES process the irreversible heat is removed at the cooler. To avoid the extra heat generated by the turbine during delivery, a different pressure ratio is chosen for the delivery step so that the outlet gas temperature $T_2 = T_{2nom}$ as shown in Table 4-1:

$$PR' = PR^{1/\zeta^2} \tag{4.5}$$

The dimensionless length and time are defined as:

$$\Lambda = \frac{ha}{\rho_g U_g c_{pg}} L \tag{4.6}$$

$$\eta = \frac{ha}{\rho_s c_{ps}} t \tag{4.7}$$

where L is the total length of the tank. Those dimensionless numbers were also used in White's work [73] on the study of PHES processes and exist in several works related to heat regenerators [89, 91]. Eq. (4.1) and (4.2) are then transformed into

$$\theta_n = \beta T_n + \chi \theta_{n-1} \tag{4.8}$$

$$\frac{dT_n}{d\eta} = \theta_n - T_n \tag{4.9}$$

where β and χ are defined as

$$\beta = \frac{\Lambda / N}{1 + \Lambda / N} \tag{4.10}$$

$$\chi = 1 - \beta \tag{4.11}$$

Because the cooler and heater will keep the temperature of the gas going into the LP tank and the HP tank constant, the temperature profile in the two tanks can be solved separately. Here for the sake of simplicity we solve them together in a set of linear differential equations.

In the loading step the compartments are numbered clockwisely from the bottom of the LP tank to the bottom of the HP tank:

$$
\frac{d}{d\eta}\begin{bmatrix} T_1 \\ T_2 \\ \vdots \\ T_n \\ T_{n+1} \\ \vdots \\ T_{2n} \end{bmatrix} = \underbrace{\begin{bmatrix} \beta-1 & 0 & 0 & & & & \cdots & 0 \\ \chi\beta & \beta-1 & 0 & 0 & 0 & & \cdots & 0 \\ \vdots & & \ddots & 0 & 0 & & \cdots & 0 \\ \chi^{n-1}\beta & \cdots & \chi\beta & \beta-1 & 0 & 0 & \cdots & 0 \\ 0 & 0 & \cdots & 0 & \beta-1 & 0 & 0 & 0 \\ \vdots & \vdots & \vdots & & & & \ddots & 0 \\ 0 & 0 & \cdots & 0 & \chi^{n-1}\beta & \cdots & \chi\beta & \beta-1 \end{bmatrix}}_{A}\begin{bmatrix} T_1 \\ T_2 \\ \vdots \\ T_n \\ T_{n+1} \\ \vdots \\ T_{2n} \end{bmatrix} + \underbrace{\begin{bmatrix} \chi T_{0nom}/\alpha \\ \chi^2 T_{0nom}/\alpha \\ \vdots \\ \chi^n T_{0nom}/\alpha \\ \chi T_{2nom}w \\ \vdots \\ \chi^n T_{2nom}w \end{bmatrix}}_{F}
$$

(4.12)

In the delivery step the compartments are numbered counter-clockwisely from the bottom of the HP tank to the bottom of the LP tank:

$$
\frac{d}{d\eta}\begin{bmatrix} T_1 \\ T_2 \\ \vdots \\ T_n \\ T_{n+1} \\ \vdots \\ T_{2n} \end{bmatrix} = \underbrace{\begin{bmatrix} \beta-1 & 0 & 0 & & & & \cdots & 0 \\ \chi\beta & \beta-1 & 0 & 0 & 0 & & \cdots & 0 \\ \vdots & & \ddots & 0 & 0 & & \cdots & 0 \\ \chi^{n-1}\beta & \cdots & \chi\beta & \beta-1 & 0 & 0 & \cdots & 0 \\ 0 & 0 & \cdots & 0 & \beta-1 & 0 & 0 & 0 \\ \vdots & \vdots & \vdots & & & & \ddots & 0 \\ 0 & 0 & \cdots & 0 & \chi^{n-1}\beta & \cdots & \chi\beta & \beta-1 \end{bmatrix}}_{A}\begin{bmatrix} T_1 \\ T_2 \\ \vdots \\ T_n \\ T_{n+1} \\ \vdots \\ T_{2n} \end{bmatrix} + \underbrace{\begin{bmatrix} \chi T_{0nom} \\ \chi^2 T_{0nom} \\ \vdots \\ \chi^n T_{0nom} \\ \chi T_{2nom} \\ \vdots \\ \chi^n T_{2nom} \end{bmatrix}}_{F'}
$$

(4.13)

Eq. (4.12) and (4.13) can be written in the matrix notation as:

$$\frac{d\mathbf{T}(\eta)}{d\eta} = \mathbf{A}\mathbf{T}(\eta) + \mathbf{F} \tag{4.14}$$

$$\frac{d\mathbf{T}(\eta)}{d\eta} = \mathbf{A}\mathbf{T}(\eta) + \mathbf{F}' \tag{4.15}$$

Eq. (4.14) and (4.15) have the same form of exponential matrix solution as:

96

$$\mathbf{T}(\eta) = e^{\mathbf{A}\eta}(\mathbf{T}_0 + \mathbf{A}^{-1}\mathbf{F}) - \mathbf{A}^{-1}\mathbf{F} \qquad (4.16)$$

The corresponding gas temperature can be calculated as:

$$\boldsymbol{\theta}(\eta) = (\mathbf{A} + \mathbf{I})\mathbf{T}(\eta) + \mathbf{F} \qquad (4.17)$$

The cyclic steady state solutions of the solid temperature distribution after the delivery step and the loading step, namely $\mathbf{T}_{ssc}$ and $\mathbf{T}_{ssh}$, have the following relationship:

$$\mathbf{T}_{ssh} = e^{\mathbf{A}\pi}(\mathbf{T}_{ssc} + \mathbf{A}^{-1}\mathbf{F}) - \mathbf{A}^{-1}\mathbf{F} \qquad (4.18)$$

$$\mathbf{T}_{ssc} = \mathbf{M}\left[e^{\mathbf{A}\pi'}(\mathbf{M}\mathbf{T}_{ssh} + \mathbf{A}^{-1}\mathbf{F}') - \mathbf{A}^{-1}\mathbf{F}' \right] \qquad (4.19)$$

where $\mathbf{M} = \begin{bmatrix} 0 & & & 1 \\ & & 1 & \\ & \cdot^{\cdot^{\cdot}} & & \\ 1 & & & 0 \end{bmatrix}$, π and π' are the dimensionless time of the loading and

delivery step respectively. $\mathbf{M}$ is used as a factor to reverse the compartments order. Solving Eq. (4.18) and (4.19) we have:

$$\mathbf{T}_{ssc} = \left[\mathbf{I} - \mathbf{M}e^{\mathbf{A}\pi'}\mathbf{M}e^{\mathbf{A}\pi}\right]^{-1}\mathbf{M}\left[e^{\mathbf{A}\pi'}\left[\mathbf{M}(e^{\mathbf{A}\pi}\mathbf{A}^{-1}\mathbf{F} - \mathbf{A}^{-1}\mathbf{F}) + \mathbf{A}^{-1}\mathbf{F}'\right] - \mathbf{A}^{-1}\mathbf{F}'\right]$$
$$(4.20)$$

$$\mathbf{T}_{ssh} = \left(\mathbf{I} - e^{\mathbf{A}\pi}\mathbf{M}e^{\mathbf{A}\pi'}\mathbf{M}\right)^{-1}\left[e^{\mathbf{A}\pi}\left(\mathbf{M}\left(e^{\mathbf{A}\pi'}\mathbf{A}^{-1}\mathbf{F}' - \mathbf{A}^{-1}\mathbf{F}'\right) + \mathbf{A}^{-1}\mathbf{F}\right) - \mathbf{A}^{-1}\mathbf{F}\right]$$
$$(4.21)$$

Hence the exponential matrix solutions for cyclic steady state temperature distribution are obtained. Together with Eq. (4.16) we are able to calculate not only the cyclic steady state temperature profile but also the transient temperature profile during each step.

4.3.1   Definition of the turn-around efficiency and storage bed utilization ratio

The turn-around efficiency is widely described in existing studies [73, 79, 83] on PHES processes as the ratio of amount of work obtained during delivery to the amount of work stored during loading. We will follow the same definition to be consistent with them. However it is worth noting that the turn-around efficiency does not equal the overall process efficiency, which is defined as the ratio of the work obtained during

delivery to the total energy provided in both the loading and delivery step. The bed

utilization ratio is the ratio of actual stored energy and the maximum amount of energy

that can be stored with the existing PHES process. Because the solid properties, e.g.

tank dimensions and heat capacity, can be canceled out, the utilization ratio is

represented by the volume averaged temperature difference between the loading step

and delivery step. The detailed derivations are described in the following work.

The energy flow diagram is provided in Figure 4-6, where Q_{hot1}, Q_{cool1}, Q_{hot2} and

Q_{cool2}, are the heat transferred at the electric heater and cooler when loading and

delivering. W_{net1} and W_{net2} is the amount of work done at the compressor and work

received at the expander during the loading and delivering step.

Based on the first principle the energy stored in the process during the loading step is:

$$\Delta E_{tot} = Q_{hot1} + W_{net1} - Q_{cool1} = W_{net2} - Q_{hot2} + Q_{cool2} \tag{4.22}$$

Neglecting the energy accumulated in the gas phase we have:

$$\Delta E_{tot} \approx \Delta E_{HP} + \Delta E_{LP} = \rho_s c_{ps} LS(\overline{\Delta T_{HP}} + \overline{\Delta T_{LP}}) \tag{4.23}$$

$\overline{\Delta T_{HP}}$ and $\overline{\Delta T_{LP}}$ are the volume average temperature differences before and after the

loading step of the solid in the HP tank and the LP tank respectively. The total stored

energy has a linearly relationship with $\overline{\Delta T_{HP}} + \overline{\Delta T_{LP}}$, which is defined as the average

temperature difference $\Delta T_{average}$ and can be easily calculated based on our model.

Q_{hot1} W_{net1} Q_{hot2} W_{net2}

$\Delta E_{tot}= Q_{hot1} + W_{net1} - Q_{cool1}$ $\Delta E_{tot}= Q_{hot2} - W_{net2} - Q_{cool2}$

Loading   Delivery
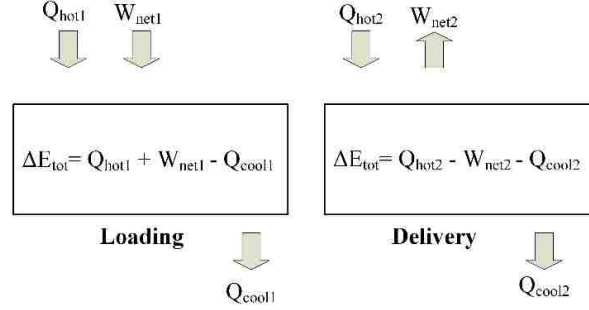
Q_{cool1} Q_{cool2}

Figure 4-6 Energy flow diagram during the loading and the delivery step

The turn-around efficiency is then defined as:

$$Eff = 1 - \frac{Q_{cool1}+Q_{cool2}}{\Delta E_{tot} + Q_{cool1}} = \frac{W_{net2}-Q_{hot2}}{W_{net1}+Q_{hot1}} \tag{4.24}$$

which becomes negative when Q_{hot2} is larger than W_{net2}. It can now be expressed as

dimensionless numbers as the following:

$$
\begin{aligned}
Eff &= 1 - \frac{Q_{cool1}+Q_{cool2}}{\Delta E_{tot} + Q_{cool1}} \\
&= 1 - \frac{U_g \rho_g c_{pg} \overline{\Delta T_{cool1}}t + U_g \rho_g c_{pg} \overline{\Delta T_{cool2}}t}{\rho_s c_{ps} L(\overline{\Delta T_{HP}} + \overline{\Delta T_{LP}}) + U_g \rho_g c_{pg} \overline{\Delta T_{cool1}}t} \\
&= 1 - \frac{(\overline{\Delta T_{cool1}} + \overline{\Delta T_{cool2}})\pi}{\Lambda(\overline{\Delta T_{HP}} + \overline{\Delta T_{LP}}) + \overline{\Delta T_{cool1}}\pi}
\end{aligned}
\tag{4.25}
$$

where $\overline{\Delta T_{cool1}}$, $\overline{\Delta T_{cool2}}$, $\overline{\Delta T_{hot1}}$ and $\overline{\Delta T_{hot2}}$ are time averaged temperature differences

at the cooler and heater during the loading and delivery step respectively.

For given storage vessels we prefer to design a PHES process with not only high turn-

around efficiency but also large storage capacity. To quantify the percentage of the used

storage capacity, a storage bed utilization ratio is defined as:

$$R_U = \frac{\overline{\Delta T_{HP}} - \overline{\Delta T_{LP}}}{(T_3 - T_{0nom}) - (T_{2nom} - T_1)} \tag{4.26}$$

Similar conception was discussed in White's work [113], where it was referred as a

capacity or utilization factor by the ratio of π/Λ and similar dimensionless analysis was

done for availability losses in PHES processes. We will show that R_U is very close to

the value of π/Λ in most cases but starts to diverge when π is close to Λ later. When the vessels are fully utilized, R_U equals 1 and thermal fronts travel through the whole storage vessel. When step time approaches zero R_U will reduce to zero. Therefore R_U is mainly a function of step time.

4.4 Simulation setup

In this work the matrix exponential is calculated using Matlab function EXPM. Discussions on the algorithms to compute the matrix exponential can be found in Moler and Loan's work [92]. The temperature profiles in the tanks are obtained by discretizing it into N_1=300 compartments while the net work of turbomachines and heat duties of heaters and coolers for each time step are calculated using N_2=300 time steps. Increasing N_1 and N_2 to 400 will change the turn-around efficiency and utilization ratio by less than 1%. The value of operating parameters are T_{0nom}=298.15K, T_{2nom}=773.15, PR=3, PR'=3.88, γ=1.66 and ζ=0.9 unless otherwise specified. The computation time for calculating a complete dynamic cycle of loading and delivery is around 60 seconds by running MATLAB R2013a on an Intel i5 3.10 GHz, 8 GB RAM and Windows 7 64-bit computer.

An analytical solution for a single charge operation for a heat regenerator is available in White's work [73] and is shown below:

$$\theta_g(\xi,\eta) - \theta_s(\xi,\eta) = \exp\left(-(\xi+\eta)\right) I_0\left(2\sqrt{\xi\eta}\right) \qquad (4.27)$$

where θ, ξ and η are the dimensionless temperature, length and time respectively and I_0 is the zero-th order modified Bessel function of the first kind. The number of compartments used in this work causes dispersion effects as discussed in Levenspiel's work [90]. For a given size of regenerator the larger the number of compartments, the closer it is to the analytical solution. In Figure 4-7 the results are shown for a single

charge operation heating the regenerator with Λ=400 from 25 ºC to 500 ºC. The numerical solution represents well the travelling of thermal front in the regenerator, however, dispersion effects make the front spread wider, resulting in a slightly smaller turn-around efficiency.
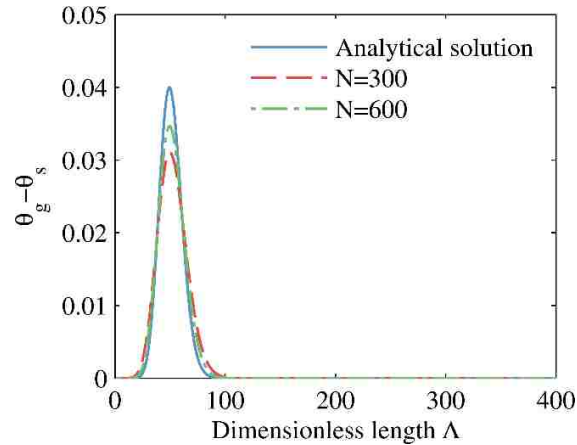
Figure 4-7 Comparison of dimensionless temperature difference during a single charge operation when Λ=400 π=50

4.5 Results and discussion

In order to evaluate the influence of turbomachine irreversibilities and film resistance to heat transfer on the PHES process capacity and efficiency, three levels of approximations including four models are proposed:

1. A flat front model with the polytropic efficiency ζ=1 for turbomachines,

2. A flat front model with the polytropic efficiency ζ=0.9 for turbomachines,

3. A film resistance model with the polytropic efficiency ζ=1 and 0.9 for turbomachines.

In a flat front model heat transfer reaches equilibrium immediately so that the initial step change of fluid temperature retains its shape when travelling through the tank. When the polytropic efficiency ζ equals to 1, compression and expansion in turbomachines are considered to be reversible, in which case PR=PR' and no additional

heat needs to be removed at the cooler. The following equation is used to calculate the corresponding isentropic efficiency for compressors and turbines:

$$\zeta_{is,c} = \frac{PR^{(\gamma-1)/\gamma} - 1}{PR^{(\gamma-1)/(\gamma\zeta)} - 1} \qquad (4.28)$$

$$\zeta_{is,t} = \frac{PR^{-\zeta(\gamma-1)/\gamma} - 1}{PR^{-(\gamma-1)/\gamma} - 1} \qquad (4.29)$$

Note that PR is the pressure ratio of the HP tank and LP tank. Therefore the corresponding isentropic efficiency for the compressor and turbine are calculated as 0.87 and 0.92 in the PHES process here.

4.5.1 Flat front model and $\zeta=1$

When $\pi < \Lambda$ the front is still contained in the tank thus the storage capacity has a linear relationship with the distance travelled by the front. The dimensionless length for such a distance can be represented as the following:

$$\Lambda_{front} = \frac{ha}{U_g \rho_g C_g} z = \frac{ha}{U_g \rho_g C_g} t_{step} \frac{U_g \rho_g C_g}{\rho_s C_s} = \pi \qquad (4.30)$$

To maximize process efficiency π need to be kept smaller than Λ to avoid the breakthrough of the front. When step time π is equal to Λ the storage vessels are fully used and R_U becomes 1, which is true for all flat front models. Also $\zeta=1$ means turbomachines are reversible so that the pressure ratios during loading and delivery are the same, which in this case equals 3 for both steps. Assume that the temperature at the heater and cooler stays the same, $T_3 = T_{2nom}PR^{(\gamma-1)/\gamma} = 1196.6$ K and $T_1 = T_{0nom}/PR^{(\gamma-1)/\gamma} = 192.6$ K. In this case $\Delta T_{average}$ equals to $(T_3-T_{0nom})-(T_{2nom}-T_1) = 318$ K and the turn-around efficiency equals 1.

4.5.2   Flat front model and $\zeta=0.9$

The average temperature difference can still be represented by $(T_3-T_{0nom})-(T_{2nom}-T_1)$ = 386 K, where outlet gas temperature T_1 and T_3 will be the same as that calculated in Table 4-1. Note that $\Delta T_{average}$ in this case is 386 K compared with 318 K in the previous case when $\zeta=1$. Therefore the storage capacity at a constant pressure ratio is increased when the irreversibilities of turbomachines are considered. However the turn-around efficiency is lower because of the additional heat caused by the losses in the turbomachines. According to Eq. (4.24)

$$Eff = 1 - \frac{Q_{cool1}+Q_{cool2}}{\Delta E_{tot}+Q_{cool1}} = 1 - \frac{T_0 - T_{0nom}}{(T_3 - T_{0nom})-(T_{2nom}-T_1)} \qquad (4.31)$$

which is equivalent to the equation derived in Desrues et al.'s work [120].Therefore the turn-around efficiency is around 82.4% based on the numbers in Table 4-1. Moreover Eq. (4.31) shows that when there is no heat transfer resistance, the turn-around efficiency is independent of tank size and operation duration.

4.5.3   Film resistance heat transfer model, $\zeta=1$ and $\zeta=0.9$

The turn-around efficiency and utilization ratio are functions of the gas and solid material properties, pressure ratios and the dimensionless numbers π and Λ. A base case is studied with parameters T_{0nom}=298.15K, T_{2nom}=773.15, PR=3, γ=1.66, π=100 and Λ=200. As shown in Table 4-2 the turn-around efficiency are affected by both the polytropic efficiency and the film heat transfer resistance. The utilization ratio is determined by the ratio of π and Λ. Changing the polytropic efficiency from 1 to 0.9 has little effect on the utilization ratio. The heat transfer resistance reduced the utilization ratio because that the thermal front is stretched inside the storage tank and after reaching

cyclic steady state the front partially breakthrough the storage tank as shown in Figure

4-8 and Figure 4-9.

Table 4-2 Results of four different models where $\pi=100$ and $\Lambda=200$

Model assumptions	$\Delta T_{average}$ / K	Eff %	R_U %
Flat front, $\zeta =1$	318	100	50
Flat front, $\zeta =0.9$	386	82.4	50
Film resistance, $\zeta =1$	156	88.4	48.9
Film resistance, $\zeta =0.9$	189	72.2	48.9

Details on how each of the operating variables and dimensionless numbers affect the

turn-around efficiency and the utilization ratio in the film resistance heat transfer model

will be discussed below.

4.5.3.1 *Cyclic steady state solid temperature distributions in the LP and HP tanks*

With Eq. (4.20) and (4.21) the cyclic steady state temperature distributions at the end

of each step are obtained, while the transients are solved based on Eq. (4.16). As shown

in Figure 4-8 and Figure 4-9 the thermal wave propagates with respect to time after the

cyclic steady state is reached. During the loading step the thermal wave moves from the

bottom to the top in the LP tank while in the HP tank it moves from the top to the bottom.

During the delivery step it moves in the opposite direction. The outlet temperature of

both tanks starts to change as the thermal front breaks through, which can be used as a

signal to switch from loading to delivery or vice versa. Due to the same step duration

and the heater and cooler acting as temperature regulators, the cyclic steady state

temperature profiles at the end of each step are centrally symmetric. However the

transient profiles do vary a little in the beginning of a new step but remain the same

while travelling through the tank.
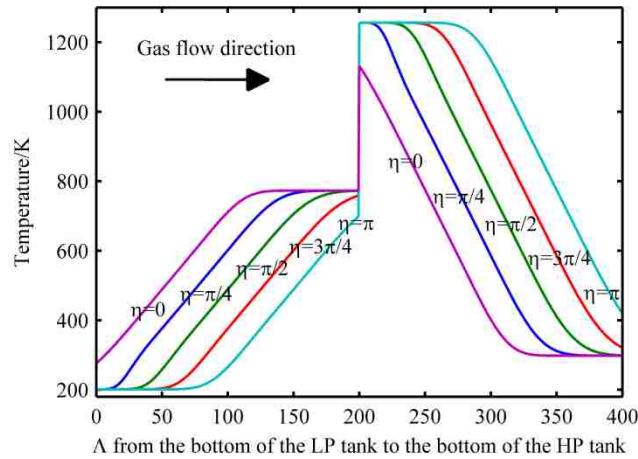
Figure 4-8 Solid temperature profile during the loading step after the cyclic steady state is reached when PR=3, PR'=3.88, T_{0nom} =298.15K, T_{2nom}= 773.15K, π=100 and Λ=200
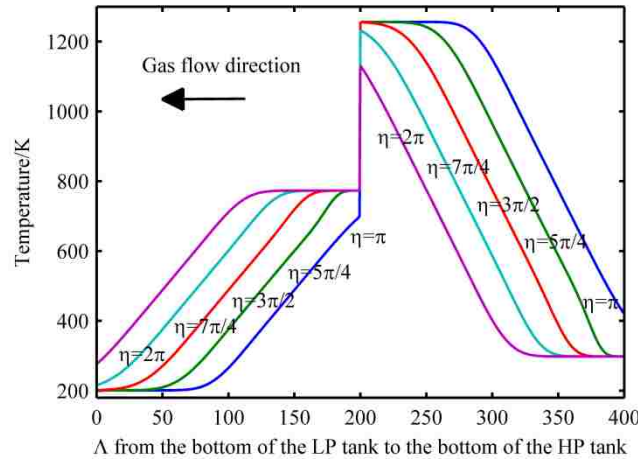
Figure 4-9 Solid temperature profile during the delivery step after the cyclic steady state is reached when PR=3, PR'=3.88, T_{0nom} =298.15K, T_{2nom}= 773.15K, π=100 and Λ=200

4.5.3.2 Comparison of air and argon as the process gas

Only the effects of different heat capacity ratios of the two gases are discussed here while the other parameters are the same as those in the base case of film resistance and ζ =0.9 model. The heat capacity ratio γ for air is 1.4 while for argon it is 1.66. Changing the working gas from argon to air in this case changes the temperature ratio at the turbomachines. It greatly reduces the average temperature difference by 38.2% and slightly changes the turn-around efficiency from 72.2% to 67.2%. Therefore a higher

heat capacity ratio is crucial for the total capacity of the process and it also helps to improve the turn-around efficiency. Furthermore for the same Λ since argon has a higher density compared to air at the same conditions, the superficial velocity U_g for argon will be smaller than that for air, which means less attrition for the solid material and stress for the turbomachines. Also inert argon will greatly reduce the oxidation effects at high temperatures.

4.5.3.3 Effects of changing the loading step pressure ratio: PR

It is showed in Figure 4-10 that by increasing the loading step pressure ratio PR from 2 to 5 the turn-around efficiency is raised from 0.67 to 0.76 while the utilization ratio stays the same around 0.49. Higher pressure ratio can increase the turn-around efficiency but hardly affect the utilization ratio. Meanwhile the highest temperature of the solid materials in the HP tank is also increased from 1050 to 1574 K, which on one hand increases the average temperature difference thus help improve the storage capacity, on the other hand together with the high pressure turns to a challenge for both the energy storage material and process equipment. Considering the working temperature of a regenerator packed with inexpensive ceramic materials for iron and steel combustion air preheating is from 500 to 1350 °C [93], the pressure ratio ranges between 2 to 5 in our study. To avoid the maximum temperature limit T_{2nom} is set to -15°C in Howes's [80] 2-MW PHES process so that the pressure ratio can be chosen as 12 with the highest temperature being 500 °C.
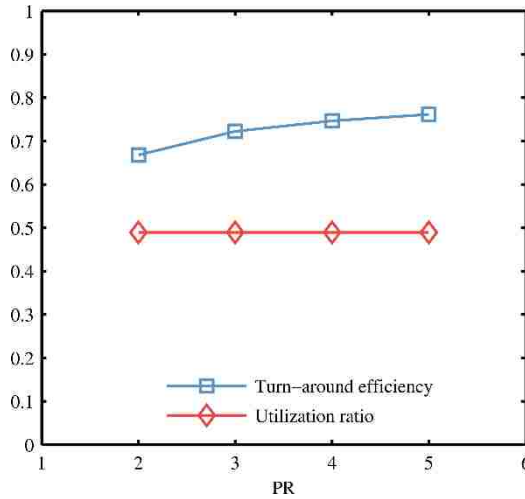
Figure 4-10 Relationship between PR and turn-around efficiency and utilization ratio

4.5.3.4 *Effects of changing the dimensionless numbers: π and Λ on the capacity and efficiency*

Since the dimensionless step duration π and the dimensionless tank length Λ are comprised by several parameters, some of which are distinct like ρ_g, C_{pg}, U_g and L to Λ and ρ_s, C_{ps} and t_{step} to π while the others are the same like h and a, we will discuss their effects separately.

The effects of changing dimensionless numbers Λ and π independently on turn-around efficiency and utilization ratio are shown in Figure 4-11. Once Λ is fixed changing the step time π will change the temperature distribution inside each tank when the cyclic steady state is reached, as shown in Figure 4-12. The utilization ratio increases almost linearly with the step time π until π is close to Λ. Then it starts to level off, which is associated with the breakthrough of the thermal wave resulting in uniform temperature distribution for the solid material thus reaching its maximum capacity. The linear relationship between the total temperature difference and π is in accordance with the flat front model, which is valid when π is relatively small compared with Λ.
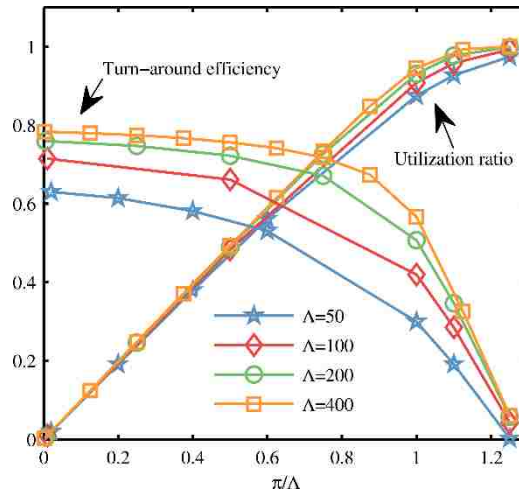
Figure 4-11 Effects of π and Λ on turn-around efficiency and utilization ratio when T_{0nom}=298.15K, T_{2nom}= 773.15K, PR$_1$=3 and PR$_2$=3.88
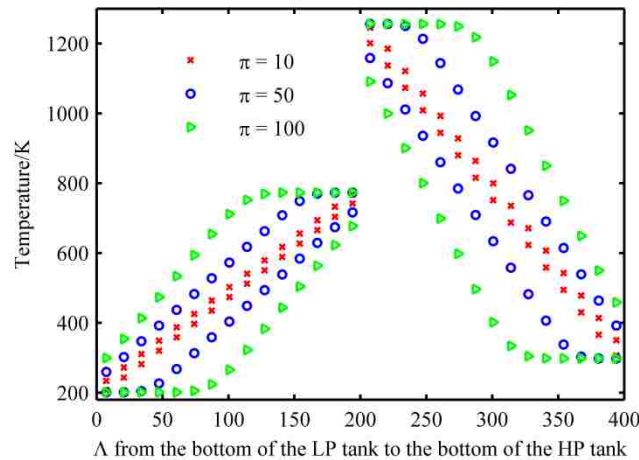
Figure 4-12 Temperature profile at the end of loading and delivery step with different values of π when T_{0nom}=298.15K, T_{2nom}= 773.15K, PR=3, PR'=3.88 and Λ=200

The turn-around efficiency decreases as π increases and the maximum efficiency is determined by Λ. The maximum efficiency is increased from 63% to 78% by changing Λ from 50 to 400. The maximum efficiency is limited by the irreversibilities of turbomachines and cannot be higher than 82.4% in the flat front model when ζ=0.9. Also it takes longer time for the efficiency to drop to a certain value with a larger Λ, which is an advantage for larger size vessels.

The results indicate that choosing a proper value for Λ not only determines the maximum capacity but also the maximum efficiency. Besides π needs to be set carefully since a larger value of π comes with larger capacity but lower efficiency.
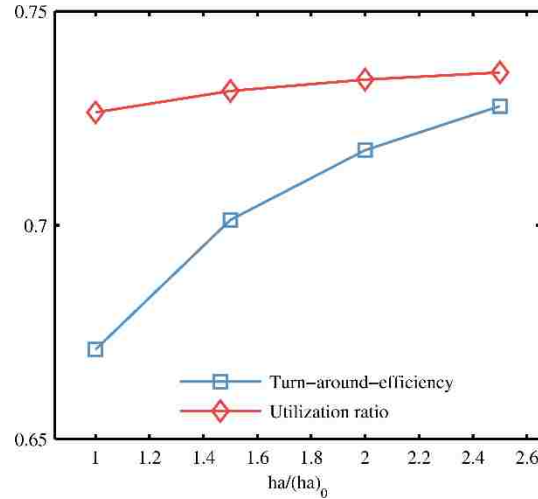
Figure 4-13 Effects of ha on the efficiency and the total temperature difference when T_{0nom}=298.15K, T_{2nom}= 773.15K, PR_1=3, PR_2=3.88, π_o=150 and Λ_o=200

So far we have discussed the effects of varying Λ and π separately using their distinct factors. By changing the value of ha, π and Λ can be changed together. To better illustrate the effects of changing π and Λ together a base case is chosen where π_o=150 and Λ_o=200. As shown in Figure 4-13 that a higher value of ha results in slightly higher utilization ratio and turn-around efficiency. Increasing the surface area and the heat transfer coefficient does have a larger impact on turn-around efficiency than on utilization ratio.

4.5.3.5 *Effects of turbomachinary polytropic efficiency*

According to McTigue et al. [75] after optimization the losses associated with pressure drop and irreversible heat transfer are only a few percent and the performance of PHES processes may be determined by the efficiency of turbomachinary. As we

mentioned before Desrues et al. [79] derived the following equation for the flat front model:

$$Eff = 1 + \frac{T_{0nom}(1 - \psi^{1/\zeta^3 - \zeta})}{T_{2nom}(\psi^{1/\zeta} - 1) + T_{0nom}(\psi^{-\zeta} - 1)} \qquad (4.32)$$

Therefore we can compare the effects of turbomachinary efficiency in both the film resistance heat transfer model and flat front model. As shown in Figure 4-14, it is clear that in both models the polytropic efficiency is an important factor for the turn-around efficiency. A small decrease in the polytropic efficiency will result in a large drop in the turn-around efficiency. The utilization ratio, however, is not affected. Another effect of decreasing the polytropic efficiency is that the temperature ratio at the turbomachines is changed. The average temperature difference is increased from 171 K to 232 K when the polytropic efficiency is reduced from 0.95 to 0.8. The storage capacity is therefore increased as a side effect.
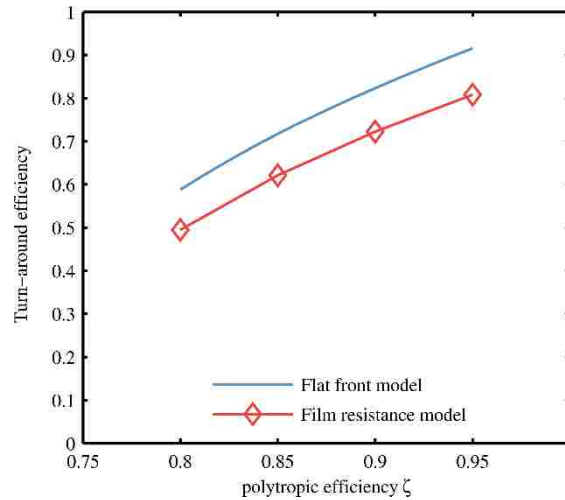
Figure 4-14 Effects of turbomachinary polytropic efficiency on the process turn-around efficiency when T$_{0nom}$=298.15K, T$_{2nom}$= 773.15K, PR$_1$=3, PR$_2$=3.88, π=100 and Λ=200

4.5.3.6 Asymmetrical operation

Previously we have focused on the symmetrical operation during which the loading period π equals the delivery period π'. For a PHES process with identical LP and HP

storage tanks, we can imagine that in a flat front model the cyclic steady state position of the thermal front will be determined by the shorter duration step in an asymmetrical operation. For example if π is larger than π' the energy input during $\pi-\pi'$ will be wasted at the heater and cooler because the front moves out of the tank during this time. In practice we may encounter situations where the loading period might be longer or shorter than the delivery period. Therefore we analyzed those two asymmetrical operation scenarios and compared them with the symmetrical operation and the results are shown in Figure 4-15. Both asymmetrical operations result in the breakthrough of thermal fronts, therefore greatly reducing the turn-around efficiency. The utilization ratio, as discussed for the flat front model, is determined by the shorter step time. For example when we keep π the same and increase the value of π', the utilization ratio stays the same when $\pi' > \pi$. It decreases with π' when $\pi' < \pi$.
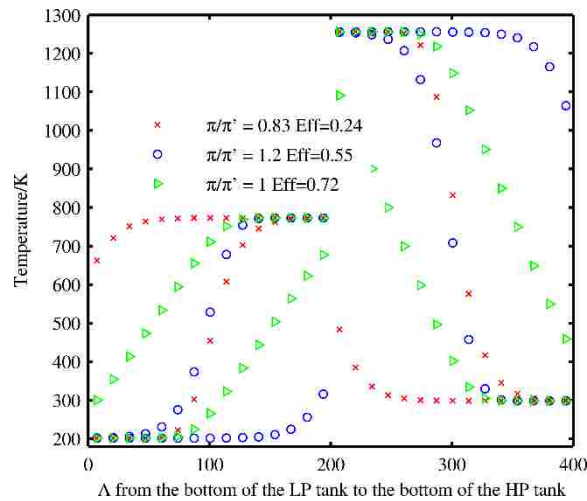
Figure 4-15 Solid cyclic steady state temperature distribution for different operation scenarios when T_{0nom}=298.15K, T_{2nom}= 773.15K, PR_1=3, PR_2=3.88, π=100 and Λ=200

4.6 Conclusions

We used a simplified discretized heat transfer model to simulate the pumped heat energy storage system. Exponential matrix solutions for transients and cyclic steady

111

state temperature distributions were easily obtained and used for process analysis. Turn-around efficiency and storage utilization ratio were defined to characterize the performance of the system. Effects of different process gases, pressure ratios, and dimensionless parameters on those two factors were discussed, which provides us guidelines for later design and detailed modeling. Effects of heat transfer resistance and turbomachinery efficiency on the process performance are compared. Turbomachinery efficiency is found to be the limiting factor to the turn-around efficiency. Symmetric operation for PHES processes is suggested to achieve high turn-around efficiency and utilization ratio. The dynamic process of the system pressure change when switching to a new step and dependence of heat capacity and heat transfer coefficient on temperature, pressure and Reynolds number is neglected in this work. The matrix exponential solution won't be available in those cases. In order to take those detailed engineering effects into account, a traditional numerical method need to be used. The matrix exponential solution provides us a convenient approach to analyze the cyclic steady state process performance for PHES processes and is well suited for a first principle analysis.

4.7 Illustrative example

Here we use an example given by Levenspiel [90] to demonstrate the design process for a typical PHES process based on our exponential matrix solutions. Given two storage vessels with 32 m high and 3 m in diameter filled with uniformly sized spherical basaltic beach stones, an appropriate step time is needed to make full use of the storage capacity while keeping the turn-around efficiency relatively high. By calculation of the two dimensionless numbers, an appropriate operation point can be easily found according to Figure 4-11. To compare PHES processes with available technologies like lead acid

batteries, storage specific energy ρ_{energy} is calculated with all three levels of approximations models studied before.

Data
For the solid:
d_p=0.08m ε=0.4 a=3(1- ε)/R=45 m^{-1} k_s=0.5 W m^{-1} K^{-1} ρ_s=912 kg m^{-3} C_{ps}=1000 J kg^{-1} K^{-1}
U_g=0.4 m s^{-1} at 20 °C
For Argon at 20 °C and 1 atm:
μ= 2.2×10^{-5} kg m^{-1} s^{-1} k_g=0.017 W m^{-1} K^{-1} ρ_g=1.7 kg m^{-3} C_{pg}=521 J kg^{-1} K^{-1}
For the process parameters:
PR=3, PR'=3.88, T_{0nom} =298.15K, T_{2nom}= 773.15K

$$\mathrm{Re} = \frac{d_p U_g \rho_g}{\mu} = 2473$$

$$\mathrm{Pr} = \frac{C_{pg}\mu}{k_g} = 0.67$$

Using the correlation from Levenspiel: $\dfrac{hd_p}{k_g} = 2 + 1.8\,\mathrm{Re}^{1/2}\,\mathrm{Pr}^{1/3}$

we have h = 17.1 W m^{-2} K^{-1}. Then the dimensionless length variable $\Lambda = \dfrac{haL}{\rho_g U_g C_{pg}} = 69.5$

1. Flat front model and $\zeta = 1$

   In a flat front model the maximum energy density can be achieved and R_U equals 1.

The storage specific energy is defined as:

$$\rho_{energy} = \frac{\Delta E_{tot}}{2\rho_s V} \approx \frac{\Delta E_{HP} + \Delta E_{LP}}{2\rho_s V} = c_{ps}(\overline{\Delta T_{HP}} + \overline{\Delta T_{LP}})/2 \qquad (4.33)$$

where $\overline{\Delta T_{HP}} - \overline{\Delta T_{LP}} = (T_3 - T_{0nom}) - (T_{2nom} - T_1) = 318$ K thus ρ_{energy} is calculated to be

44.2 Wh/kg and the turn-around efficiency equals one.

Table 4-3 Results of four different models for the illustrative case

Model assumptions	$\Delta T_{average}$ / K	Efficiency %	Bed utilization ratio %	Specific energy ρ_{energy} Wh/kg
Flat front, ζ =1	318	100	100	44.2
Flat front, ζ =0.9	386	82.4	100	53.6
Film resistance, ζ =1	132	79.3	41.1	18.2
Film resistance, ζ =0.9	160	64.0	41.0	22.1

2. Flat front model and $\zeta = 0.9$

The maximum energy density in this case is higher than that when $\zeta = 1$ due to the larger average temperature difference caused by the irreversiblities of turbomachines. According to Eq. (4.25) and (4.26) ρ_{energy} is calculated to be 53.6 Wh/kg and the turn-around efficiency is 82.4%.

3. Film heat transfer resistance model, $\zeta = 1$ and $\zeta = 0.9$

Based on the simulation results shown in Figure 4-11, the maximum turn-around efficiency and the total capacity will be limited with such a small value of Λ regardless of the value of π chosen. For $\pi = 30$, $t_{step} = \rho_s C_{ps} \pi / ha = 9.9$ h. As shown in Table 4-3 for $\zeta = 1$, $\Delta T_{average} = 132$ K, $R_U = 41.1\%$ and Eff = 79.3%. For $\zeta = 0.9$ $\Delta T_{average} = 160$ K, $R_U = 41.0\%$ and Eff is 64.0%. The storage specific energy can then be calculated as 18.2 and 22.1 Wh/kg respectively.

Compared with lead acid batteries with specific energy between 30 and 50 Wh/kg [68], this PHES process has the potential to reach 53.6 Wh/kg when in flat front model and $\zeta = 0.9$. When considering the heat transfer resistance the specific energy drops down to 22.1 Wh/kg while turn-around efficiency becomes 64.0%. Alternatives to improve the performance include increasing the pressure ratio to increase the specific energy, and raising the value of Λ to increase the maximum turn-around efficiency. Note that in an actual PHES process other losses like pressure loss, mechanical and electrical losses are inevitable, thus we would expect an even lower efficiency.

Nomenclature

a	solid material surface area to volume ratio, m^2/m^3
A	discretization matrix for the governing equations
C_{pg}	gas heat capacity, J/(kg K)
C_{ps}	solid heat capacity, J/(kg K)
d_p	particle diameter, m
ΔE_{tot}	Energy stored during the loading step and released during the delivery step
Eff	Turn-around efficiency
F	feed vector of the loading step
F'	feed vector of the delivery step
h	heat transfer coefficient, $J/(m^2 \text{ s K})$
I	identity matrix
l	length of each compartment, m
L	total length of each tank, m
M	matrix to reverse the compartments order
n	tank index
N_1	number of compartments
N_2	number of time steps
PR	pressure ratio of the HP tank and the LP tank during loading
PR'	pressure ratio of the HP tank and the LP tank during delivery
R_U	tank utilization ratio
t_{step}	step duration, s
T	solid temperature vector, K
T_{ssh}	solid temperature vector for cyclic steady state solution after loading, K
T_{ssc}	solid temperature vector for cyclic steady state solution after delivery, K
$\Delta T_{average}$	sum of volume average temperature difference in both HP tank and LP tanks, K
$\overline{\Delta T_{HP}}$	volume average temperature difference of the HP tank between the end of loading and delivery steps, K
$\overline{\Delta T_{LP}}$	volume average temperature difference of the LP tank between the end of loading and delivery steps, K
$\overline{\Delta T_{cool1}}$	time average temperature difference of the process gas at the cooler when loading, K
$\overline{\Delta T_{cool2}}$	time average temperature difference of the process gas at the cooler when delivering, K
$\overline{\Delta T_{hot1}}$	time average temperature difference of the process gas at the heater when loading, K
$\overline{\Delta T_{hot2}}$	time average temperature difference of the process gas at the heater when delivering, K
U_g	interstitial velocity of gas flow, m/s
w	T_{outlet}/T_{inlet} of a compressor
β	$=(\Lambda/N)/(1+\Lambda/N)$
γ	heat capacity ratio C_p/C_v
ε	void fraction of the tank
ζ	polytropic efficiency of the turbomachines
η	dimensionless time
θ	gas temperature vector
μ	gas viscosity, $kg \text{ } m^{-1} \text{ } s^{-1}$

π	dimensionless step duration
ρ_g	gas density, kg/m^3
ρ_s	bulk density of the solid material in the tank, kg/m^3
χ	=1/(1+ Λ/N)
Λ	dimensionless length of the tank
ψ	thermal compression ratio

████████ **Conclusions and Future Work**

Chapter 1

An expression for the minimum work of separation for adsorption processes based on the isotherm at ambient temperature was developed and applied to the linear isotherm and the Langmuir isotherm. It was found that the adsorbent with the linear isotherm requires less work than that with the Langmuir isotherm. In all cases considered the work was greater than the ideal work of separation from the gas mixture. Moreover we analyzed the equivalent work needed for temperature swing adsorption processes and chemical looping processes. By using zeolite 13X and CaO the equivalent work required by those two processes are compared and calcium looping process is favored for low CO_2 concentration flue gas (<5%) while temperature swing adsorption requires less energy for high CO_2 concentration flue gas (>5%). The point where the required work from both processes are equal depends on the extent of degradation of CaO. However due to the utilization of high temperature sensible heat and carbonation heat, the effects of degradation are hardly noticeable when it comes to the overall efficiency of power plants with carbon capture. Further study is needed to analyze an emerging type of new metal organic framework (MOF) which possesses characteristics of both adsorption and chemical looping. Their capacity is dependent on the partial pressure of the flue gas and the working capacity and heat of adsorption is high.

Chapter 2

In Chapter 2 we ignored the mass transfer resistance for both reaction and adsorption and focused on the effects of reaction kinetics, thermodynamic equilibrium and adsorption isotherm on the performance of the sorption enhanced reaction process.

Three model reactions with different stoichiometric parameters, the water gas shift reaction, the H_2S decomposition reaction to produce H_2 and S_2 and the propene metathesis reaction to produce ethylene and butene, were studied. It was found from the first two reactions that in order to produce high purity product the following parameters: K_r, K_{eq} and K_c need to be large enough. The equilibrium constant affects the effluent profile in two ways: 1. by changing the equilibrium concentration of the adsorbate it changes the shape of the adsorbate concentration front thus the effluent profile; 2. by changing the reaction rate it changes the shape of the reaction mass transfer zone. In the meantime the reaction rate constant and the adsorption constant affect the reaction and adsorption separately. Also the reaction stoichiometric parameters are equally important as we found out in the study of the H_2S decomposition, in which the product purity is determined by the initial concentration of S_2 in the reactor. In practice it is difficult to periodically regenerate the reactor to the required level to produce high purity hydrogen. A secondary purification process may be needed to obtain high purity hydrogen from the sorption enhanced H_2S decomposition reactor. These conclusions can be applied to the future design of a sorption enhanced reactor with various reaction schemes. The third reaction sheds light on the importance of mass transfer resistance on the product concentration for a sorption enhance reaction reactor. Further study is needed to quantify the impacts of the mass transfer process during adsorption and the diffusion terms in the mass balance equation.

Chapter 3

In Chapter 3 an experimental study of pressure swing adsorption to separate CO_2 was carried out on Na-promoted alumina at high temperature. Argon was used as a purge

gas. The highest purity product was 86% CO_2 (argon free) with a 5-step scheme where the recovery rate was only 18%. The mass balance for each step suggests more than 90% of the uncollected CO_2 was lost during the blowdown step, which was caused by the void space in the test setup. The tests also showed that the adsorption capacity of the sorbent declined rapidly after a few cycles, which matched the results from thermogravimetric analysis on used samples. Moreover, based on the pilot scale steam tests it was discovered that steam was competitively adsorbed on Na-promoted alumina with CO_2, which greatly facilitated the regeneration process. The steam capacity of Na-promoted alumina is estimated to be 2.67 mol/kg when the steam partial pressure is at 0.8 atm. To fully regenerate Na-promoted alumina saturated by 2 atm CO_2, 16.6-24.9 mol steam per mol of capture CO_2 is required. In the future an experimental setup with minimized void space should be built to test the cyclic performance of CO_2 adsorbents for pressure swing adsorption processes. A modification on our pilot scale setup is being planned to include steam in the feed CO_2 mixture to study the role of steam during adsorption on Na-promoted alumina. This will make possible the quantification of the interaction between steam and CO_2 on the surface of Na-promoted alumina and measurement of the isotherm of pure steam and mixture of steam and CO_2 at various pressures. Moreover, surface characterizations are under investigation to elucidate the mechanism behind the observed competitive behavior of CO_2 and steam on Na-promoted alumina.

Chapter 4

In Chapter 4 we used a simplified discretized heat transfer model to simulate a pumped heat energy storage system. Exponential matrix solutions for transients and

cyclic steady state temperature distributions were easily obtained and used for process analysis. Turn-around efficiency and storage utilization ratio were defined to characterize the performance of the system. Effects of different process gases, pressure ratios, and dimensionless parameters on those two factors were discussed, to provide us guidelines for detailed modeling and later design. Effects of heat transfer resistance and turbomachinery efficiency on the process performance were compared. Turbomachinery efficiency is found to be the limiting factor to the turn-around efficiency. Symmetric operation for PHES processes is suggested to achieve high turn-around efficiency and utilization ratio. The dynamic process of the system pressure change when switching to a new step and dependence of heat capacity and heat transfer coefficient on temperature, pressure and Reynolds number is neglected in this work. The matrix exponential solution will not be applicable in those cases. In order to take those detailed engineering effects into account, a traditional numerical method will need to be used. The matrix exponential solution provides us a convenient approach to analyze the cyclic steady state process performance for PHES processes and is well suited for a first principle analysis. Future work is needed to extend this analysis method to other periodic operation processes to simplify the calculation for the cyclic steady state solutions.

Appendix A. Minimum Work of Desorption

According to Myers and Monson [5] the grand potential of a clean adsorbent *in vacuo* to be immersed to equilibrium pressure of p at constant temperature T is:

$$\Delta\Omega = -RT\int_0^P \frac{n}{P}\,dP \tag{A.1}$$

which is the minimum energy required to clean the adsorbent per unit mass of adsorbent. When the adsorbent is partly cleaned from loading n_1 to n_2 the minimum energy can be calculated by taking the Gibbs free energy of gas into account.

Before desorption:

$$G_1 = \Omega_1 + n_1(\mu_g^0 + RT\ln P_1) = -RT\int_0^{P_1}\frac{n}{P}\,dP + n_1(\mu_g^0 + RT\ln P_1) \tag{A.2}$$

After desorption:

$$G_2 = \Omega_2 + n_1(\mu_g^0 + RT\ln P_2) = -RT\int_0^{P_2}\frac{n}{P}\,dP + n_1(\mu_g^0 + RT\ln P_2) \tag{A.3}$$

The Gibbs energy change during desorption:

$$\Delta G = G_2 - G_1 = -RT\int_{P_1}^{P_2}\frac{n}{P}\,dP + n_1 RT\ln\frac{P_2}{P_1} \tag{A.4}$$

According to Eq. (3) based on the reversible membrane desorption process:

$$\Delta G' = -RT\int_{n_1}^{n_2}\ln\frac{P_2}{P}\,dn \tag{A.5}$$

Integrate Eq. (21) by parts we can prove that:

$$\Delta G' = -RT\left[\ln\frac{P_2}{P}\,n\Big|_{n_1}^{n_2} - \int_{P_1}^{P_2}-\frac{n}{P}\,dP\right] = \Delta G \tag{A.6}$$

After isothermal compression of the desorbed gas from P_2 to one atmosphere:

$$W_{min} = \Delta G + (n_1 - n_2)RT\ln\frac{P_{atm}}{P_2} = -RT\int_{n_1}^{n_2}\ln\frac{P_{atm}}{P}\,dn \tag{A.7}$$

Appendix B. Gas Mixture Viscosity

The Alicat flow meter needs to be calibrated by gas viscosity in order to show the actual gas flow rate. In our previous study the Wilke equation [94] was used to calculate the gas mixture viscosity:

$$\mu_{mix} = \sum_{i=1}^{n} x_i \mu_i / (\sum_{j=1}^{n} x_j \Phi_{ij}) \tag{B.1}$$

where

$$\Phi_{ij} = \frac{1}{\sqrt{8}} \left(1 + \frac{M_i}{M_j} \right)^{-0.5} \left[1 + \left(\frac{\mu_i}{\mu_j} \right)^{0.5} \left(\frac{M_j}{M_i} \right)^{0.25} \right]^2 \tag{B.2}$$

In Eq (B.1) and (B.2) x_i, μ_i and M_i represent the molar fraction, pure component viscosity and molecular weight respectively.

However an improvement was made by Kestin and Ro [64] using the extended law of corresponding states with an accuracy of ±0.1% at 25 °C. A complete set of equations to calculate the multi-component gas mixture viscosity is listed as the following:

$$\eta_{mix} = \frac{- \begin{vmatrix} H_{11} & H_{12} & \cdots & H_{1v} & x_1 \\ H_{21} & H_{22} & \cdots & H_{2v} & x_2 \\ \vdots & & & & \vdots \\ H_{v1} & H_{v2} & \cdots & H_{vv} & x_v \\ x_1 & x_2 & \cdots & x_v & 0 \end{vmatrix}}{\begin{vmatrix} H_{11} & H_{12} & \cdots & H_{1v} \\ H_{21} & H_{22} & \cdots & H_{1v} \\ \vdots & & & \vdots \\ H_{v1} & H_{v2} & \cdots & H_{vv} \end{vmatrix}} \tag{B.3}$$

where v is the number of gas species in the mixture and

$$H_{ii} = \frac{x_i^2}{\eta_i} + \sum_{k=1, k \neq i}^{v} \frac{2 x_i x_k}{\eta_{ik}} \frac{M_k}{(M_i + M_k)^2} \left(\frac{5 M_i}{3 A_{ik}^*} + M_k \right) \tag{B.4}$$

$$H_{ij} = -\frac{2x_i x_j}{\eta_{ij}} \frac{M_i M_j}{(M_i + M_j)^2} (\frac{5}{3A_{ij}^*} - 1) \quad \text{(B.5)}$$

$$\eta_{ij} = \frac{5}{16} [\frac{2m_i m_j kT}{\pi(m_i + m_j)}]^{0.5} \frac{f_\mu}{\sigma^2 \Omega_{i,j}^{(2,2)*}} = 26.7 [\frac{2M_i M_j T}{(M_i + M_j)}]^{0.5} \frac{f_\mu}{\sigma^2 \Omega_{i,j}^{(2,2)*}} \quad \text{(B.6)}$$

$$A_{ij}^* = \exp(0.1281 - 0.1108\ln(kT/\varepsilon_{ij}) + 0.0962(\ln(kT/\varepsilon_{ij}))^2 -$$
$$0.027*(\log(T/\varepsilon_{ij}))^3 + 0.0024*(\ln(kT/\varepsilon_{ij}))^4) \quad \text{(B.7)}$$

$$\Omega_{i,j}^{(2,2)*}/f_\mu = \exp(0.46649 - 0.57015\ln(kT/\varepsilon_{ij}) + 0.19164(\ln(kT/\varepsilon_{ij}))^2 -$$
$$0.03708*(\ln(kT/\varepsilon_{ij}))^3 + 0.00241*(\ln(kT/\varepsilon_{ij}))^4)$$
$$\text{(B.8)}$$

where the units of η, M, T, σ and ε/k is μP, g/mol, K, Å and K. The value of σ_{ij} and

ε_{ij}/k for CO_2, N_2 and Ar were listed in Table B-1 and Table B-2.

Table B-1 The scaling factor σ_{ij} (Å) for CO_2, N_2 and Ar

σ_{ij} (Å)	N_2	Ar
CO_2	3.705	3.604
	N_2	3.48

Table B-2 The scaling factor ε_{ij}/k (K) for CO_2, N_2 and Ar

ε_{ij}/k (K)	N_2	Ar
CO_2	151.1	156.5
	N_2	120

The results of those two different gas mixture viscosity model are compared in Figure

B-1.
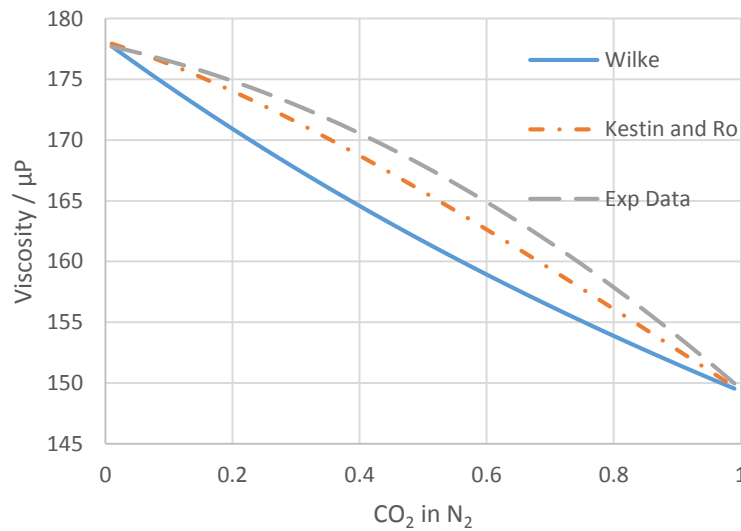
Figure B-1 Comparison of two gas mixture models from Wilke and Kestin and Ro with experimental data

Bibliography

[1] A.H. Berger, A.S. Bhown, Optimizing Solid Sorbents for CO_2 Capture, Energy Procedia, 37 (2013) 25-32.

[2] A.H. Berger, A.S. Bhown, Comparing physisorption and chemisorption solid sorbents for use separating CO_2 from flue gas using temperature swing adsorption, Energy Procedia, 4 (2011) 562-567.

[3] Y. Li, C. Zhao, H. Chen, Q. Ren, L. Duan, CO_2 capture efficiency and energy requirement analysis of power plant using modified calcium-based sorbent looping cycle, Energy, 36 (2011) 1590-1598.

[4] J. Wilcox, Carbon capture, Springer, 2012.

[5] A. Myers, P. Monson, Adsorption in porous materials at high pressure: theory and experiment, Langmuir, 18 (2002) 10261-10273.

[6] K. Chue, J. Kim, Y. Yoo, S. Cho, R. Yang, Comparison of activated carbon and zeolite 13X for CO_2 recovery from flue gas by pressure swing adsorption, Industrial & Engineering Chemistry Research, 34 (1995) 591-598.

[7] L.-S. Fan, L. Zeng, S. Luo, Chemical-looping technology platform, AIChE Journal, 61 (2015) 2-22.

[8] P. Peltola, J. Ritvanen, T. Tynjälä, T. Hyppänen, Model-based evaluation of a chemical looping combustion plant for energy generation at a pre-commercial scale of $100MW_{th}$, Energy Conversion and Management, 76 (2013) 323-331.

[9] J. Katzer, S. Ansolabehere, J. Beer, J. Deutch, A. Ellerman, S. Friedmann, H. Herzog, H. Jacoby, P. Joskow, G. McRae, The future of coal, Massachusetts Institute of Technology, (2007) 17-42.

[10] J. Blamey, E.J. Anthony, J. Wang, P.S. Fennell, The calcium looping cycle for large-scale CO_2 capture, Progress in Energy and Combustion Science, 36 (2010) 260-279.

[11] K. Kim, D. Kim, Y.-K. Park, K.S. Lee, A solid sorbent-based multi-stage fluidized bed process with inter-stage heat integration as an energy efficient carbon capture process, International Journal of Greenhouse Gas Control, 26 (2014) 135-146.

[12] I. Martínez, R. Murillo, G. Grasa, N. Rodríguez, J. Abanades, Conceptual design of a three fluidised beds combustion system capturing CO_2 with CaO, International Journal of Greenhouse Gas Control, 5 (2011) 498-504.

[13] K. Konrad, S. Robert, K. Walter, G. Wilhelm, Production of hydrogen, US Patent No. US1816523, (1931).

[14] B. Carvill, J. Hufton, M. Anand, S. Sircar, Sorption‐enhanced reaction process, AIChE Journal, 42 (1996) 2765-2772.

[15] D.P. Harrison, Sorption-Enhanced Hydrogen Production: A Review, Industrial & Engineering Chemistry Research, 47 (2008) 6486-6501.

[16] K.B. Lee, M.G. Beaver, H.S. Caram, S. Sircar, Effect of reaction temperature on the performance of thermal swing sorption-enhanced reaction process for simultaneous production of fuel-cell-grade H_2 and compressed CO_2 from synthesis gas, Industrial & Engineering Chemistry Research, 47 (2008) 6759-6764.

[17] M.G. Beaver, H.S. Caram, S. Sircar, Sorption enhanced reaction process for direct production of fuel-cell grade hydrogen by low temperature catalytic steam-methane reforming, Journal of Power Sources, 195 (2010) 1998-2002.

[18] H.M. Jang, K.B. Lee, H.S. Caram, S. Sircar, High-purity hydrogen production through sorption enhanced water gas shift reaction using K_2CO_3-promoted hydrotalcite, Chemical Engineering Science, 73 (2012) 431-438.

[19] M. Li, K. Duraiswamy, M. Knobbe, Adsorption enhanced steam reforming of methanol for hydrogen generation in conjunction with fuel cell: Process design and reactor dynamics, Chemical Engineering Science, 67 (2012) 26-33.

[20] K. Johnsen, H. Ryu, J. Grace, C. Lim, Sorption-enhanced steam reforming of methane in a fluidized bed reactor with dolomite as CO_2-acceptor, Chemical Engineering Science, 61 (2006) 1195-1202.

[21] Y. Ding, E. Alpay, Adsorption-enhanced steam–methane reforming, Chemical Engineering Science, 55 (2000) 3929-3940.

[22] J. Hufton, S. Mayorga, S. Sircar, Sorption‐enhanced reaction process for hydrogen production, AIChE Journal, 45 (1999) 248-256.

[23] C.H. Lee, S. Mun, K.B. Lee, Application of multisection packing concept to sorption-enhanced steam methane reforming reaction for high-purity hydrogen production, Journal of Power Sources, 281 (2015) 158-163.

[24] X. Wu, S. Wu, Production of high-purity hydrogen by sorption-enhanced steam reforming process of methanol, Journal of Energy Chemistry, 24 (2015) 315-321.

[25] K.D. Dewoolkar, P.D. Vaidya, Improved hydrogen production by sorption-enhanced steam methane reforming over hydrotalcite-and calcium-based hybrid materials, Energy & Fuels, (2015).

[26] M.P. Elsner, C. Dittrich, D.W. Agar, Adsorptive reactors for enhancing equilibrium gas-phase reactions—two case studies, Chemical Engineering Science, 57 (2002) 1607-1619.

[27] W.E. Waldron, J. Hufton, S. Sircar, Production of hydrogen by cyclic sorption enhanced reaction process, AIChE Journal, 47 (2001) 1477-1479.

[28] M. Grünewald, D.W. Agar, Enhanced catalyst performance using integrated structured functionalities, Chemical Engineering Science, 59 (2004) 5519-5526.

[29] B. Arstad, J. Prostak, R. Blom, Continuous hydrogen production by sorption enhanced steam methane reforming (SE-SMR) in a circulating fluidized bed reactor: Sorbent to catalyst ratio dependencies, Chemical Engineering Journal, 189 (2012) 413-421.

[30] K.B. Lee, M.G. Beaver, H.S. Caram, S. Sircar, Production of fuel-cell grade hydrogen by thermal swing sorption enhanced reaction concept, International Journal of Hydrogen Energy, 33 (2008) 781-790.

[31] V.E. Kaloidas, N.G. Papayannakos, Kinetic studies on the catalytic decomposition of hydrogen sulfide in a tubular reactor, Industrial & Engineering Chemistry Research, 30 (1991) 345-351.

[32] W. Serrand, Process for removing sulfur moieties from claus tail-gas, European Patent No. EP0332373A2, (1989).

[33] B. Karl, H. Wilhelm, H. Reinhard, S. Klaus, Process of purifying sulfur-containing exhaust gases and of recovering sulfur, Us Patent No. US3637352, (1972).

[34] S. Rawadieh, V.G. Gomes, I. Altarawneh, Optimizing packing heterogeneity for sorption enhanced metathesis reaction, Adsorption, 20 (2014) 701-711.

[35] V.G. Gomes, K.W.K. Yee, A periodic separating reactor for propene metathesis, Chemical Engineering Science, 57 (2002) 3839-3850.

[36] V.G. Gomes, O.M. Fuller, Dynamics of propene metathesis: Physisorption and diffusion in heterogeneous catalysis, AIChE Journal, 42 (1996) 204-213.

[37] Y. Choi, H.G. Stenger, Water gas shift reaction kinetics and reactor modeling for fuel cell grade hydrogen, Journal of Power Sources, 124 (2003) 432-439.

[38] G.C. Chinchen, P.J. Denny, J.R. Jennings, M.S. Spencer, K.C. Waugh, Synthesis of Methanol: Part 1. Catalysts and Kinetics, Applied Catalysis, 36 (1988) 1-65.

[39] K.B. Lee, A. Verdooren, H.S. Caram, S. Sircar, Chemisorption of carbon dioxide on potassium-carbonate-promoted hydrotalcite, Journal of Colloid and Interface Science, 308 (2007) 30-39.

[40] H.M. Jang, W.R. Kang, K.B. Lee, Sorption-enhanced water gas shift reaction using multi-section column for high-purity hydrogen production, International Journal of Hydrogen Energy, 38 (2013) 6065-6071.

[41] R.T. Yang, Gas separation by adsorption processes, Butterworth-Heinemann, 2013.

[42] M.E.D. Raymont, Make hydrogen from hydrogen-sulfide, Hydrocarbon Processing, 54 (1975) 139-142.

[43] S.C. Moffat, A.A. Adesina, The dissociation kinetics of H_2S over an alumina supported Co-Mo sulphide catalyst, Catalysis Letters, 37 (1996) 167-172.

[44] K. Fukuda, M. Dokiya, T. Kameyama, Y. Kotera, Catalytic Decomposition of Hydrogen Sulfide, Industrial & Engineering Chemistry Fundamentals, 17 (1978) 243-248.

[45] E. Furimsky, Activity of spent hydroprocessing catalysts and carbon supported catalysts for conversion of hydrogen sulphide, Applied Catalysis a-General, 156 (1997) 207-218.

[46] M. Gwaunza, A.A. Adesina, The performance of a Ru-Mo sulfide catalyst for H_2S decomposition, Reaction Kinetics and Catalysis Letters, 62 (1997) 55-62.

[47] D. Cao, A.A. Adesina, Fluidised bed reactor studies of H_2S decomposition over supported bimetallic Ru catalysts, Catalysis Today, 49 (1999) 23-31.

[48] V.E. Kaloidas, N.G. Papayannakos, Hydrogen production from the decomposition of hydrogen sulphide. Equilibrium studies on the system H_2S/ H_2/Si, (i = 1,...,8) in the gas phase, International Journal of Hydrogen Energy, 12 (1987) 403-409.

[49] M. Schuster, S. Blechert, Olefin metathesis in organic chemistry, Angewandte Chemie International Edition in English, 36 (1997) 2036-2056.

[50] M. Maroño, Y. Torreiro, D. Cillero, J.M. Sánchez, Experimental studies of CO_2 capture by a hybrid catalyst/adsorbent system applicable to IGCC processes, Applied Thermal Engineering, 74 (2015) 28-35.

[51] S.P. Wang, S.L. Yan, X.B. Ma, J.L. Gong, Recent advances in capture of carbon dioxide using alkali-metal-based oxides, Energy & Environmental Science, 4 (2011) 3805-3819.

[52] Y. Ding, E. Alpay, Equilibria and kinetics of CO_2 adsorption on hydrotalcite adsorbent, Chemical Engineering Science, 55 (2000) 3461-3474.

[53] J. Boon, P.D. Cobden, H.A.J. van Dijk, C. Hoogland, E.R. van Selow, M. van Sint Annaland, Isotherm model for high-temperature, high-pressure adsorption of and on K-promoted hydrotalcite, Chemical Engineering Journal, 248 (2014) 406-414.

[54] A. Hanif, S. Dasgupta, S. Divekar, A. Arya, M.O. Garg, A. Nanoti, A study on high temperature CO_2 capture by improved hydrotalcite sorbents, Chemical Engineering Journal, 236 (2014) 91-99.

[55] S. Sircar, C.M.A. Golden, PSA process for removal of bulk carbon dioxide from a wet high-temperature gas, European Patent No. EP 1142623 A2, (2000).

[56] K.B. Lee, M.G. Beaver, H.S. Caram, S. Sircar, Chemisorption of carbon dioxide on sodium oxide promoted alumina, AIChE Journal, 53 (2007) 2824-2831.

[57] K.B. Lee, M.G. Beaver, H.S. Caram, S. Sircar, Reversible chemisorption of carbon dioxide: simultaneous production of fuel-cell grade H_2 and compressed CO_2 from synthesis gas, Adsorption-Journal of the International Adsorption Society, 13 (2007) 385-397.

[58] K.B. Lee, M.G. Beaver, H.S. Caram, S. Sircar, Novel thermal-swing sorption-enhanced reaction process concept for hydrogen production by low-temperature steam-methane reforming, Industrial & Engineering Chemistry Research, 46 (2007) 5003-5014.

[59] K.B. Lee, M.G. Beaver, H.S. Caram, S. Sircar, Reversible Chemisorbents for Carbon Dioxide and Their Potential Applications, Industrial & Engineering Chemistry Research, 47 (2008) 8048-8062.

[60] K.B. Lee, M.G. Beaver, H.S. Caram, S. Sircar, Performance of Na_2O promoted alumina as CO_2 chemisorbent in sorption-enhanced reaction process for simultaneous production of fuel-cell grade H_2 and compressed CO_2 from synthesis gas, Journal of Power Sources, 176 (2008) 312-319.

[61] M.G. Beaver, H.S. Caram, S. Sircar, Selection of CO_2 chemisorbent for fuel-cell grade H_2 production by sorption-enhanced water gas shift reaction, International Journal of Hydrogen Energy, 34 (2009) 2972-2978.

[62] K. Jeong, S. Sircar, H.S. Caram, Modeling of Heat Recovery from a Steam-Gas Mixture in a High-Temperature Sorption Process, AIChE Journal, 58 (2012) 312-321.

[63] S. Walspurger, P.D. Cobden, W.G. Haije, R. Westerwaal, G.D. Elzinga, O.V. Safonova, In Situ XRD Detection of Reversible Dawsonite Formation on Alkali Promoted Alumina: A Cheap Sorbent for CO2 Capture, European Journal of Inorganic Chemistry, 2010 (2010) 2461-2464.

[64] J. Kestin, S.T. Ro, The viscosity of nine binary and two ternary mixtures of gases at low density, Berichte der Bunsengesellschaft für physikalische Chemie, 78 (1974) 20-24.

[65] D.M. Ruthven, S. Farooq, K.S. Knaebel, Pressure swing adsorption, VCH publishers New York, 1994.

[66] D. Rastler, Electricity energy storage technology options: a white paper primer on applications, costs and benefits, Electric Power Research Institute, 2010.

[67] G.L. Soloveichik, Battery technologies for large-scale stationary energy storage, Annual review of chemical and biomolecular engineering, 2 (2011) 503-527.

[68] H. Chen, T.N. Cong, W. Yang, C. Tan, Y. Li, Y. Ding, Progress in electrical energy storage system: A critical review, Progress in Natural Science, 19 (2009) 291-312.

[69] M. Morandin, F. Maréchal, M. Mercangöz, F. Buchter, Conceptual design of a thermo-electrical energy storage system based on heat integration of thermodynamic cycles–Part B: Alternative system configurations, Energy, 45 (2012) 386-396.

[70] A. Thess, Thermodynamic Efficiency of Pumped Heat Electricity Storage, Physical review letters, 111 (2013) 110602.

[71] M. Morandin, F. Maréchal, M. Mercangöz, F. Buchter, Conceptual design of a thermo-electrical energy storage system based on heat integration of thermodynamic cycles–Part A: Methodology and base case, Energy, 45 (2012) 375-385.

[72] Y.-M. Kim, D.-G. Shin, S.-Y. Lee, D. Favrat, Isothermal transcritical CO_2 cycles with TES (thermal energy storage) for electricity storage, Energy, 49 (2013) 484-501.

[73] A.J. White, Loss analysis of thermal reservoirs for electrical energy storage schemes, Applied Energy, 88 (2011) 4150-4159.

[74] A. White, G. Parks, C.N. Markides, Thermodynamic analysis of pumped thermal electricity storage, Applied Thermal Engineering, 53 (2013) 291-298.

[75] J.D. McTigue, A.J. White, C.N. Markides, Parametric studies and optimisation of pumped thermal electricity storage, Applied Energy, 137 (2015) 800-811.

[76] B.M. Wolf, Procédé d'accumulation et de récupération d'énergie, International Patent No. WO2007093277 A1, (2009).

[77] J. Ruer, Installation et procedes de stockage et restitution d'energie electrique, International Patent No. WO2008148962 A3, (2008).

[78] J. Macnaghten, J.S. Howes, Energy storage, Internatinal Patent No. WO 2009/044139 A2, (2009).

[79] T. Desrues, J. Ruer, P. Marty, J. Fourmigué, A thermal energy storage process for large scale electric applications, Applied Thermal Engineering, 30 (2010) 425-432.

[80] J. Howes, Concept and development of a pumped heat electricity storage device, Proceedings of the IEEE, 100 (2012) 493-503.

[81] J. Hemrle, L. Kaufmann, M. Mercangoez, Thermoelektrisches Energiespeichersystem mit einem Zwischenspeichertank und Verfahren zum Speichern der thermoelektrischen Energie, European Patent No. EP 2275649 A1, (2011).

[82] J. Hemrle, L. Kaufmann, M. Mercangoez, A. Z'Graggen, Electro-thermal energy storage system and method for storing electro-thermal energy, European Patent No. EP 2698506 A1, (2012).

[83] M. Mercangoez, J. Hemrle, L. Kaufmann, Thermoelectric energy storage system having an internal heat exchanger and method for storing thermoelectric energy, Internatinal Patent No. WO2011045282 A2, (2011).

[84] A. White, J. McTigue, C. Markides, Wave propagation and thermodynamic losses in packed-bed thermal reservoirs for energy storage, Applied Energy, 130 (2014) 648-657.

[85] F. Marguerre, ueber ein neues Verfahren zur Aufspeicherung elektrischer Energie, Mitteilungen der Vereinigung der Elektrizitätswerke, 354 (1924) 27-35.

[86] M. Mercangöz, J. Hemrle, L. Kaufmann, A. Z'Graggen, C. Ohler, Electrothermal energy storage with transcritical CO_2 cycles, Energy, 45 (2012) 407-415.

[87] J.S. Howes, J. MacNaghten, Energy Storage, Internatinal Patent No. WO 2009/044139 A2, (2009).

[88] J. Ruer, Installation and method for storing and returning electrical energy, US Patent No. US20100301614 A1, (2010).

[89] B.J. Carnish, H.S. Caram, Explicit Matrix Solution of the Discretized Thermal Regenerator Model, Numerical Heat Transfer, Part B: Fundamentals, 54 (2008) 390-407.

[90] O. Levenspiel, Design of long heat regenerators by use of the dispersion model, Chemical Engineering Science, 38 (1983) 2035-2045.

[91] M. Jakob, Heat Transfer, Wiley, 1957.

[92] C. Moler, C. Van Loan, Nineteen dubious ways to compute the exponential of a matrix, twenty-five years later, SIAM review, 45 (2003) 3-49.

[93] G. Beckmann, P.V. Gilli, Thermal energy storage: Basics, Design, Applications to power generation and heat supply, (1984).

[94] R.B. Bird, W.E. Stewart, E.N. Lightfoot, Transport phenomena, John Wiley & Sons, 2007.

Vita

Fan Ni was born in Jingzhou, Hubei Province, China in 1988. His father, Gaoyang Ni, is a middle school chemistry teacher and his mother, Cuilan Xu, is a primary school mathematics teacher. He is the only child of the family and stayed at his hometown until finishing high school.

He entered Zhejiang University in 2005 to study under the Department of Chemical and Biological Engineering. After obtaining his B.S. in Pharmaceutical Engineering in 2009 he came to Lehigh University to study in the Ph.D. program of chemical engineering.

The work in his thesis results in several conference presentations and journal publications. The first 2 chapters were presented at the AIChE annual meeting at Salt lake city 2015. The last chapter was presented at the AIChE annual meeting at Pittsburgh 2012 and later published on *Applied Thermal Engineering*. Three more papers corresponding to the first three chapters respectively are under preparation for submission.

After graduation he will join Wanhua Chemical Group Co. Ltd at Yantai, Shandong Province, China as a research engineer.